Department of Precision and Microsystems Engineering

Towards bottom-up fabrication of a boron-doped diamond chip electrode

R.J.A. Brocken

Report no : 2020.047
Coach : Dr. J.G. Buijnsters
Professor : Dr. J.G. Buijnsters
Specialisation : Micro and Nano Engineering (MNE)
Type of report : Master Thesis
Date : 9 November 2020

TU Delft Delft University of Technology

Challenge the future

Towards bottom-up fabrication of a boron-doped diamond chip electrode

R.J.A. Brocken

Delft University of Technology

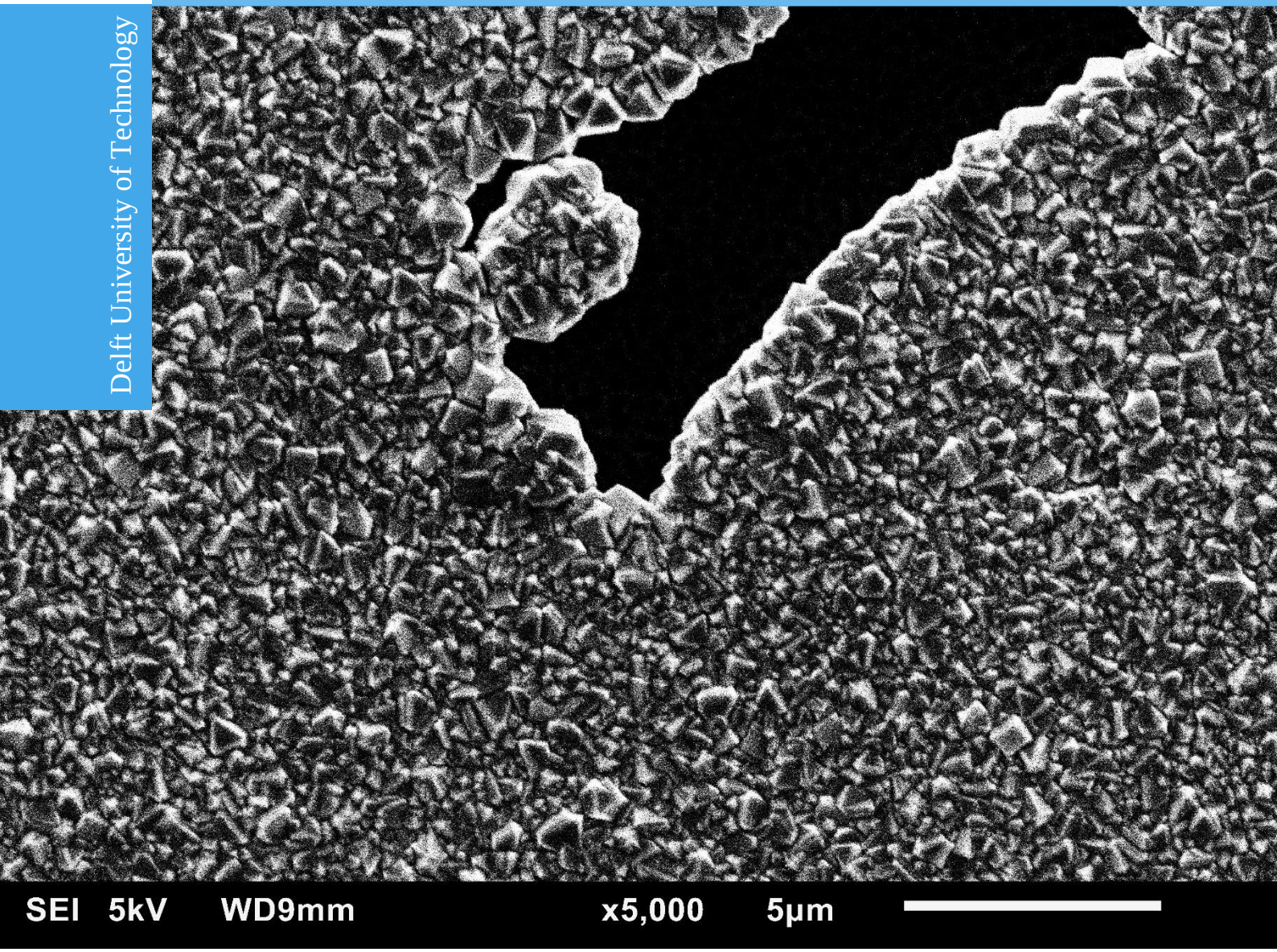

TU Delft Delft University of Technology

Challenge the future

Towards bottom-up fabrication of a boron-doped diamond chip electrode

by

R.J.A. Brocken

to obtain the degree of Master of Science
at the Delft University of Technology,
to be defended publicly on Monday November 9, 2020 at 10:00 AM.

Student number:	4312465	
Supervisor:	dr. J.G. Buijnsters	
Thesis committee:	Prof. dr. U. Staufer,	TU Delft
	Dr. J.G. Buijnsters,	TU Delft
	Dr.ir. J.F.L. Goosen,	TU Delft

This thesis is confidential and cannot be made public until November 9, 2022.

An electronic version of this thesis is available at http://repository.tudelft.nl/.

TU Delft Delft University of Technology

Preface

I would like to thank my partner Vera, for her support and patience troughout this endeavor. My parents for their encouragement, love and support throughout my life. My supervisor Ivan Buijnsters for his guidance during the project and his enthusiasm and knowledge on diamond and thin films. This motivated me in researching this topic. I would like to thank André Sartori for his support during and even after working at the TU Delft. Antoine Gerritse for allowing this opportunity and being a mentor during the start of my career. Murali Ghatkesar, Romme Koldenhof, Daniel Fan, Zhichoa Liu and Saleh Aghajani for their help, training and support in the labs. Agnieska Kooijman Banaszak, Sander van Asperen and Anne Doerr for training and allowing me to use equipment from their departments (MSE-3mE and Bionanoscience-AS) even during corona. And the MNE staff and PME technicians.

Bob Brocken
Delft, October 2020

Abstract

Boron-doped diamond (BDD) is an attractive electrode material. When sufficiently boron-doped, diamond has metal-like conductivity and in comparison with other electrode materials has several advantages, such as low and stable background current, reduced biofouling, broad potential window, corrosion resistance and chemical stability. However, current fabrication processes rely on top-down techniques, that often require cleanrooms and expensive micro fabrication techniques. This research focuses on a low-cost bottom-up fabrication technique by using an inkjet printing process to locally increase the substrate seeding density. Thin-film BDD can then be selectively grown into electrode geometries. The BDD electrodes can be used as more robust and better performing electrodes for detecting micropollutants in environmental monitoring or for detecting bio markers in saliva, sweat or blood, in health monitoring.

Inkjet manufacturing is an emerging production process in micro fabrication. Due to its accuracy, material efficiency, and given that it is a digital process, inkjet printing is a strong candidate for bottom-up fabrication of low-cost and customizable BDD (micro)-electronics. Two inkjet printers were used to investigate the micro fabrication technique for a BDD chip electrode. A hacked desktop Epson printer was used to demonstrate the capabilities of selective seeding using 'diamond' ink on silicon substrates and to grow patterned thin-film intrinsic diamond. However, the printer lacks the required control to produce continuous structures with high accuracy. A second method for selective seeding was employed by using a PIXDRO LP-50 commercial research printer, which has a high resolution, motion controlled print bed. With the application of surface treatments, such as oxygen plasma, on the silicon substrate and the development of different inks, continuous films of nanocrystaline diamond with line resolution of approximately 60 μm are produced in a final chemical vapor deposition (CVD) growth step. In addition, by loading the printer with a silver ink part of the diamond film has been coated with silver, which demonstrates that a reference electrodes or electrode leads can be manufactured with the same production technique.

This research demonstrates the potential for the bottom-up fabrication of chip electrodes using the inkjet printing process. Furthermore, as this process is not limited to the production of BDD electrodes, it opens the path towards bottom-up fabrication of other (boron-doped) diamond sensor devices, such as gas sensors or 2D heaters.

Contents

Abbreviations

MNE	Micro and Nano Engineering
PME	Precision and Microsystems Engineering
MSE	Materials Science and Engineering
BDD	Boron-doped diamond
SPEs	Screen-printed electrodes
NPs	Nanoparticles
CVD	Chemical vapour deposition
HPHT	High pressure high temperature
DND	Detonation nanodiamond
TMB	Trimethyl-boron
HFCVD	Hot filament CVD
MVCVD	Microwave plasma CVD
MCD	Microcrystaline diamond
NCD	Nanocrystaline diamond
UNCD	Ultra nanocrystaline diamond
DoD	Drop on demand
CE	Counter electrode
WE	Working electrode
RE	Reference electrode
HMI	Human Machine Interface
CV	Cyclic voltammetry
DPV	Differential pulse voltammetry
FRA	Frequency response analyzer
SEM	Scanning electron microscope
SFE	Surface free energy
DLS	Dynamic light scattering
DPI	Drops per inch
GUI	Graphical user interface

1 Introduction

Over the past decades, research has been conducted into boron-doped diamond (BDD) as an electrode material. When sufficiently boron-doped, BDD is a metal-like conductor and has several advantages over other commonly used electrode materials, such as gold, platinum or glassy carbon. It has a wide potential window, is highly corrosion resistant, is chemically stable and has a small and stable background current.

1.1 Background

The NWO research project 'DIAMOND MAKES SENSE' is a four-year project aimed at a simplified fabrication and functionalization approach of diamond micro-electrodes for use in electrochemical sensors [1]. This MSc thesis project intends to contribute to the fabrication of BDD micro-electrodes and diamond surface engineering. Current BDD chip electrodes [2, 3] are manufactured using top-down techniques that usually require cleanrooms and expensive (micro-)fabrication equipment. A simplified fabrication process is the bottom-up manufacturing of BDD electrodes based on selective seeding of diamond nanoparticles (NPs). Inkjet printing has the potential to selectively seed these diamond NPs by incorporating them into the ink solution. A commercially available BDD chip electrode is based on screen-printed electrodes (SPEs) which are reviewed in section 2.6.3, given that SPEs are now widely used for electrochemical sensing and are based on bottom-up growth, but with the disadvantage that they are usually only developed for single use. The envisaged BDD chip electrode offers the advantages of chemical stability as well as sustained, repeated use.

1.2 Diamond

The exceptional properties of diamond derive from the strong carbon-carbon covalent bonds, the highest atomic density of any material, and the fact that within the crystalline orientation of the sp^3 hybridization, all carbon atoms are symmetrically bonded to four neighbouring carbon atoms. Natural diamond, however, cannot be used as an electrode material as it is a very wide band gap semiconductor. Yet, during the growth process of synthetic diamond the concentration of charge carriers can be increased by the incorporation of dopant atoms. This increased concentration of charge carriers has the effect of increasing material conductivity. The most common dopant for diamond is boron, which turns diamond into a p-type semiconductor or metal-like conductor, depending on the doping level. Nitrogen [4] and phosphor have also been used as dopants to make an n-type semiconductor, although the high conductivity level achieved with boron can not be reached.

1.3 Water monitoring

Monitoring of the quality of (drinking) water is of growing importance as water sources are contaminated by an increasing amount of micropollutants [5–7].Due to the importance of water in daily life, this monitoring must be performed frequently and with ever greater precision. Current water analysing techniques are either costly, require significant maintenance or are inefficient. A BDD chip electrode for electrochemical analysis can replace difficult and costly chromatographic techniques [8] and detect micropollutants in waste and ground or surface water, with a quicker, cheaper electrochemical alternative. Electrochemical detection requires minimal sample preparation and

electrochemical sensors are compact, portable and provide real time data, thus making them suitable for in-situ analysis. According to Schmidt [9], cost effective in-situ analysis is one way to move forward in water analysis. As such, BDD is a particularly interesting material given that it is chemically very stable and, with the generation of hydroxyl radicals, can prevent electrode fouling by applying high oxidation potentials [10]. Due to these properties, BDD electrodes are suitable for electrochemical analysis.

1.4 Proposed research

The research goal of this project is to design, produce and validate a small BDD three-electrode system for the electrochemical analysis of water micropollutants.

The main research question for the project is as follows: 'How can a boron-doped diamond chip electrode be produced using bottom-up fabrication techniques?'

2 Literature

To develop a thin-film BBD device, the growth mechanism and manufacturing techniques for diamond must be understood. Thus, this chapter discusses the growth of synthetic diamond, particularly focussing on diamond NPs used for the selective seeding of diamond on non-diamond substrates. Furthermore, it considers the additional steps required for the manufacturing of BBD chip electrodes.

2.1 Diamond growth

Synthetic diamond growth is most commonly done using two production techniques: high pressure high temperature (HPHT) synthesis and chemical vapour deposition (CVD). A third production technique, detonation synthesis, is mainly used for the development of nanodiamond particles or detonation nanodiamond (DND). These particles are used for seeding on non-diamond substrates prior to CVD diamond growth. This report focuses on the CVD growth of diamond. The growth of CVD diamond occurs in a gaseous high temperature, low pressure environment of a small amount, typically 0.5-2 vol % of carbon gas, usually methane in excess hydrogen. Trimethyl-boron (TMB) is frequently used as boron source. Hydrogen is important for the growth of the sp^3 carbon, as atomic hydrogen etches sp^2 carbon at a much higher rate than sp^3 carbon, resulting in a lower amount of sp^2 carbon grown during the CVD process. Moreover, the atomic hydrogen also acts as a growth precursor to form H-terminated surface sites and produce active radical sites for carbon radical addition [11]. Due to the high substrate temperatures of 500-1200 °C, only a limited number of substrate materials, such as Si, Nb, Mo, Ti, Ta and W [12], can withstand the growth conditions.

Common CVD growth process are hot filament CVD (HFCVD), as depicted in the schematic shown in Figure 2.1, and microwave CVD (MWCVD). HFCVD uses a tungsten (W) or tantalum (Ta) filament which is heated to 2000-2400 $°C$. At this temperature, molecular hydrogen converts into atomic hydrogen. The advantages of HFCVD are that its setup is simple and that it allows growth on larger surface areas, whereas the advantage of MWCVD is that it reaches higher plasma temperatures, which result in higher concentrations of atomic hydrogen and, consequently, faster growth rates.

The growth of synthetic diamond by CVD is divided into two types, homoepitaxial and heteroepitaxial growth. While homoepitaxial growth results in the growth of single crystalline diamond, heteroepitaxial growth leads to primarily polycrystalline diamond. Polycrystalline diamond consist of diamonds with different growth facets or grains, whereas single crystalline diamond contains no grain boundaries. Depending on the grain size of the grown diamond, further distinctions are made between polycrystalline diamond thin films. These are discussed in section 2.3.1. Due to the relatively high surface energy of diamond versus silicon, the nucleation of diamond on silicon and most other substrates requires a pre-treatment of the substrate to grow a diamond thin film [13]. The nucleation density of untreated silicon substrate is usually in the order of $10^4 - 10^5 cm^{-2}$, whereas nucleation densities of $> 10^{11} cm^{-2}$ are required for high quality nano crystalline growth. Additional nucleation sites are created with a pre-treatment, or so-called seeding prior to CVD growth. the next section discusses this seeding process in more detail.

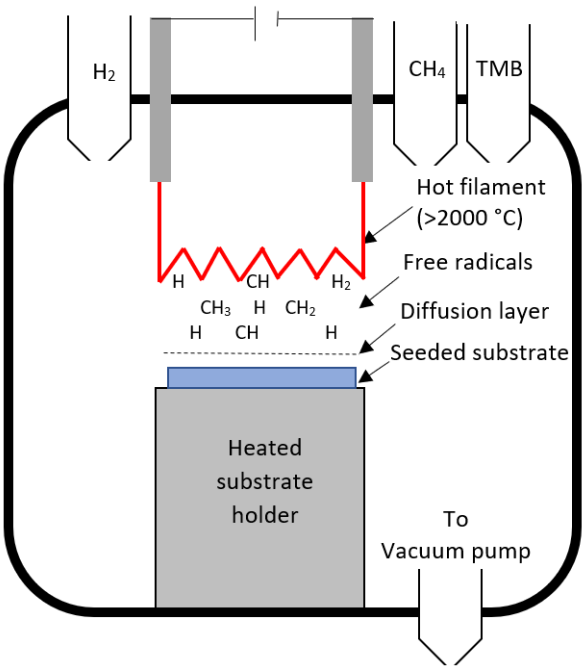

Figure 2.1: Schematic representation of an HFCVD reactor for diamond growth.

2.2 Seeding

As discussed in the previous section, an additional nucleation step is required to grow diamond on non-diamond substrates, which is frequently referred to as substrate seeding. Various methods are used, such as ultrasonic seeding, abrasion or electrical biasing. Ultrasonic seeding is a widely-used seeding technique wherein the substrate is emerged into a solution containing diamond NPs [14]. Ultrasonic seeding results in the formation of a homogeneous film over the entire surface. However, for the fabrication of the chip electrode, selective area growth must occur. In fact, selective growth of thin-film diamond or BDD has been discussed in several reports over the past decade. Selective growth can be achieved through different densities of nucleation sites on the substrate of several orders of magnitude [15]. The difference in nucleation site densities is achieved by removing or applying diamond NPs or DND in specific regions. With the use of an inkjet-printer, the research team of Ivan Buijnsters at TU Delft has recently demonstrated selective seeding in the growth of diamond microdisks on a silicon substrate [16]. Micropipetting has been used by Taylor et al. [17] and examples of template assisted growth have been reported by Sartori et al. [18].

2.2.1 Boron-doped diamond nanoparticles

Given that undoped diamond NPs used during seeding remain non-conductive after the growth of BDD films, they represent localized regions of low conductivity and form a resistive barrier at the diamond–substrate interface. The low conductivity can be detrimental for applications that require a good electrical contact with the substrate, including small electrical probes and electrodes. Therefore, the use of boron-doped seeds is recommended as it can result in a well-conductive interfacial layer [19]. Afandi et al. [20] described the use of purchased boron-included DNDs from SkySpring Nanomaterials Inc. However, these NPs are not available at the time of writing. Gines et al. [21] described the process of producing diamond NPs by bead mill grinding and Heyer et al. [22] described a similar technique for the production of heavily BDD NPs, which could be an alternative to purchasing BDD NPs.

2.3 Properties of boron-doped diamond

This paragraph examines some of the most important properties of diamond, considers how CVD growth and boron doping have an effect on the electrochemical behaviour and explains how these properties can be measured and controlled.Table 2.1 lists some of the many outstanding material properties of diamond and, more specifically, BDD.

Table 2.1: Properties of boron-doped diamond.

Mechanical Properties	**Chemical properties**	**Electrical properties**
Extremely hard material (500-800 GPa)	Chemically stable	Wide potential window
High thermal conductivity (>2000 $Wm^{-1}K^{-1}$)	Corrosion resistant	Low background current
Low thermal expansion (10^{-6} K^{-1} at 300K)	Reduced biofouling	

2.3.1 Microstructure, surface morphology and grain size

Depending on growth time and conditions, the microstructure of polycrystalline CVD diamond varies. Longer growth times result in thicker films, with higher surface roughness due to selective growth in specific crystal orientations. Figure 2.2 illustrates the increase of grain size, in relation to the increase of film thickness. Polishing this rough growth surface is expensive and time consuming. Therefore, time is spent into growing diamond thin films with smaller grain sizes. Different surface microstructures are distinguished based on their grain size namely: microcrystalline diamond (MCD, grain size $> \mu m$), nanocrystalline diamond (NCD, $10nm - 1\mu m$) and ultra nanocrystaline diamond (UNCD, $< 10nm$). In general, the smaller the grain size, the higher the sp^2 carbon content of the films as non-diamond impurities become trapped in the grain boundaries [23].

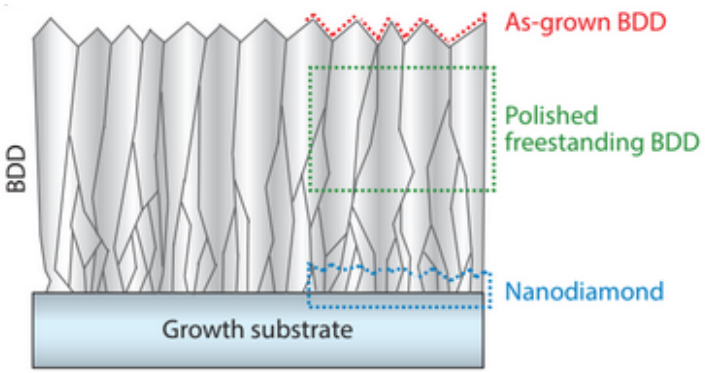

Figure 2.2: Microstructure of as grown BDD relative to thickness [24].

2.3.2 sp^2 content

The sp^2 content, which is also referred to as the non-diamond content (NDC), of a diamond thin film is an important parameter. Sp^2 carbon is less chemically inert than sp^3 carbon, making the electrode more susceptible to fouling. However, BDD electrodes with higher levels of NDC have been shown to be more favourable for electrochemical pollutant degradation [25]. Sp^2 carbon is expected to decrease the potential window of the electrode and increase the amount of background current, thus reducing the detection limits for target compounds in electroanalysis [11]. In turn, the process parameters for CVD diamond growth are usually altered in order to decrease the amount of sp^2 carbon. Yet, given that the added impurities from the addition of boron during BDD growth make it

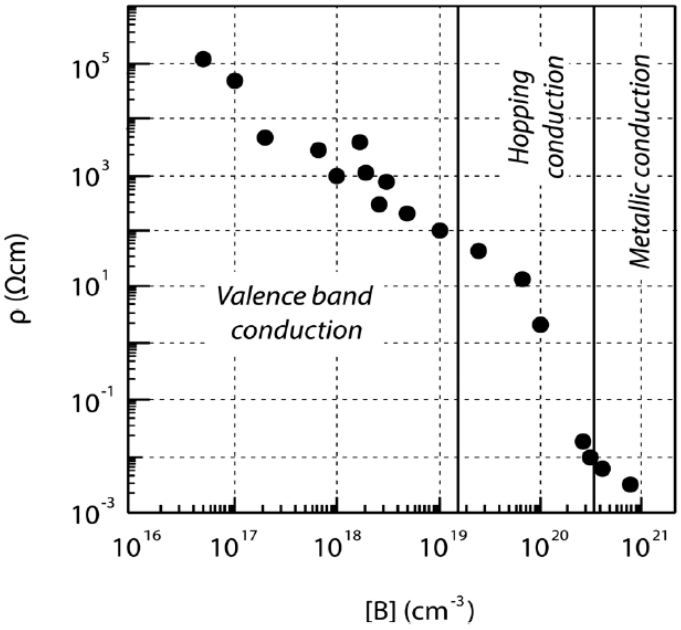

Figure 2.3: Room-temperature resistivity versus boron doping concentration [12].

more difficult to create low sp^2 carbon content, it is therefore important to monitor the amount of NDC content in a BDD electrode. The easiest way to qualitatively check for the sp^2 carbon content is through Raman spectroscopy [12].

2.3.3 Boron-doping level

Boron concentration plays an important role in diamond conductivity. Higher boron concentration means higher electrical conductivity, although it also increases the amount of impurities in the BDD. A boron density of at least 10^{20} B atoms per cm^{-3} is required for the diamond to behave as a semi-metallic. Figure 2.3 demonstrates how the amount of boron relates to BDD conductivity. The BDD colour can indicate the amount of dopant in the diamond. Typical high doping levels ($>10^{20}$ B atoms per cm^{-3}) turn BDD black, although this colour change results from NDC or sp^2 impurities. A lower doping level of 10^{19} B atoms per cm^{-3} produces a semi-conducting diamond and turns it towards a blue colour. To minimize impurities and other risks associated with high boron density, boron doping levels just above the conductive threshold are favourable [26].

2.3.4 Surface termination

After growth, BDD is usually H-terminated due to the growth process involving hydrogen in the feed gas. Over time, the BDD surface slowly oxidizes. It is therefore important to monitor the surface termination and ensure that the surface is sufficiently hydrogen terminated again, if required. The surface termination is important for wetting the BDD electrode, and it plays an important role in the inner sphere redox process, as described in section 2.5.1. The polarity of the surface results in electrostatic interactions, which can raise or lower the valence and conduction band of the BDD. By applying a water droplet, a qualitative test can be performed to check if the surface is H- or O-terminated. An oxygen-terminated BDD surface is hydrophilic, and the contact angle of the water droplet will be relatively low $< 65°$, whereas a hydrogen-terminated surface is hydrophobic and results in larger contact angles of $> 90°$. There are several methods to change the BDD surface termination. For instance, the BDD surface can be H-terminated via cathodic reaction to create hydrogen or by hydrogen plasma treatment. The BDD surface becomes more O-terminated over time due to ex-

posure to oxygen in the air. Active methods to create an O-terminated surface are anodic oxidation, boiling in acid or oxygen plasma treatment.

2.4 Inkjet printing

Inkjet printing is a well-known technique due to its use in homes and offices. As a result of its popularity, high quality printers can be purchased for a relatively low price. It is now an emerging technique for the production of electrodes on a range of substrates [27]. Inkjet printing is a digital, mask-less material deposition technique. It allows for quick design changes and prototyping with the added benefit of less material waste. Inkjet printing is distinguished by two common types, continuous inkjet printing and drop on demand (DoD). The DoD technique is divided into thermal actuated DoD and piezo DoD. In continuous inkjet printing, a continuous stream of droplets is broken into individual droplets by Rayleigh instability, and these droplets are given a negative charge. The charged droplets are then passed through a set of deflecting electrodes that "steer" the droplets either to the substrate or towards the gutter, where the droplets can be reused. The DoD techniques only create a droplet when an active signal is applied. In case of piezo DoD depicted in Figure 2.4a, the piezo active membrane is attached to the nozzle chamber where ink collects. By applying a short electronic pulse to the piezo element, the volume inside the nozzle chamber is reduced, and if a large enough pressure is applied, a droplet is ejected. The thermal DoD printhead depicted in Figure 2.4b is also based on the reduction of the volume inside the nozzle chamber, but in case of thermal activated printed by vaporizing a thin film of ink, which creates a pressure bubble and ejects a droplet. The advantage of the DoD techniques is that the working mechanics are relatively simple compared to continuous jetting and smaller picolitre droplets can be produced.

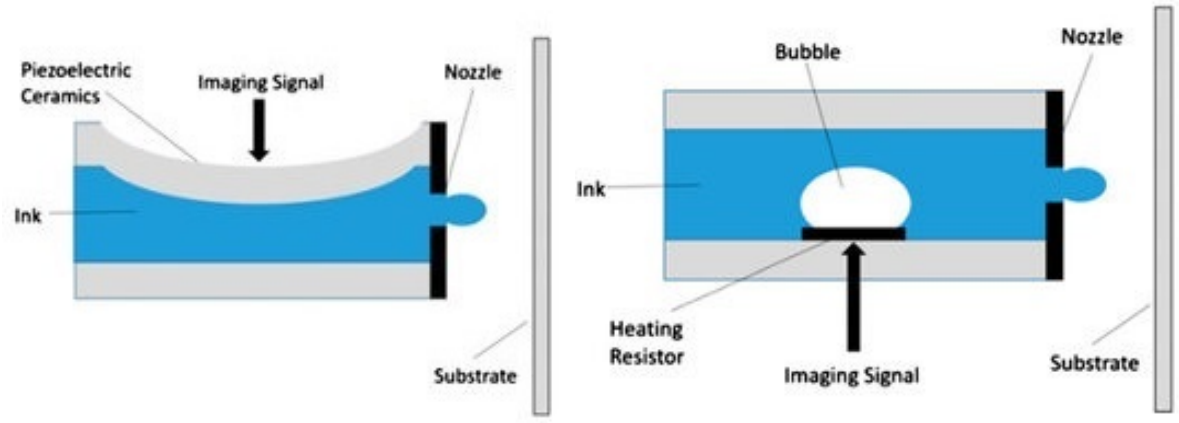

Figure 2.4: DoD printhead technologies with **(a)** piezoelectric and **(b)** thermal activation mechanism [28].

2.4.1 Printing resolution

The printing resolution of the inkjet printing process is partly defined by the minimum droplet size. Smaller droplets allow smaller features in printing. However, apart from the volume, size relates to the contact angle of the droplet. Therefore, wettability of the substrate is a major factor in inkjet printing, and different techniques are applied to change the wettability.

$$D_{con} = d_0 \sqrt[3]{\frac{8}{tan\frac{\theta}{2}(3 + tan^2\frac{\theta}{2})}} \tag{2.1}$$

The relation between the ejected drop volume, drop diameter on the substrate and the contact

angle can be described by Equation (2.1). Wherein D_{con} is drop diameter after contact with the substrate, θ the equilibrium contact angle and d_0 the diameter based on the drop volume. Three phenomena occur when the droplet comes near the surface: 1) adhesion of the droplet and the diamond NPs to the substrate surface, 2) evaporation of water and 3) cohesion among droplets. These phenomena are important because they dictate how the droplets spread over the surface [29]. Many studies have investigated the adhesion of different droplets to the surface. In inkjet printing with silver, much effort is put into preventing line bulging [30]. More specifically line bulging changes the uniformity of the printed line and thus the minimal feature size. To prevent line bulging parameters such as drop spacing, print speed and ink composition are being researched [31]. Additionally to print narrow lines, the physical properties of the substrate are altered. By changing the print surface, the wetting of the ink can be influenced. Groove can trap the liquid in smaller features, or similarly by creating local regions of higher hydrophilicity and lower hydrophobicity the ink can be confined between boundaries. Alternatively, by controlling dewetting of inkjet ink, the print line can be shrunk in perpendicular direction, allowing to print narrower lines [32].

2.4.2 Coffee-stain effect

Another important aspect when printing with inks containing NPs is controlling the evaporation rate as it contributes to the deposition of the particles on the substrate. A common phenomenon in inkjet printing is the coffee-stain effect, which is illustrated in Figure 2.5. This effect is caused by evaporation at the edge of the droplet. Capillary flow inside the droplet transfers the particles from the centre to the droplet edge boundaries, and due to this effect at the end of the drying process there is a large concentration of particles at the outer edges. One way of counteracting this effect is by causing a Marangoni flow to occur inside the droplet. This effect is based on the surface tension gradient within the droplet in combination with the vapor pressure of the liquids in the solution. In recent years, several reports have engaged the Marangoni effect to prevent the formation of the coffee stain effect [33, 34]. By using a solution with two liquids that have large differences in vapor pressure a surface tension gradient is introduced and thus Marangoni flow helps prevent the coffee-stain formation [35].

2.4.3 Ink printability

The print ability of inkjet ink can be evaluated by its viscosity, surface tension and internal forces. The dimensionless Ohnesorge (Oh) number or Z number, $Z = \frac{1}{Oh}$, can be used to predict drop formation of the inkjet ink. Z can be calculated by using the formula given in Equation Equation (2.2), which is a combination of the Reynolds (Re) and Weber (We) numbers. The Reynolds number in Equation (2.3) is a relation between the internal forces and the viscous forces of the liquid, such that ρ represents liquid density, d the nozzle diameter, v the velocity and η the dynamic viscosity. In contrast, the Weber number in Equation (2.4) is a relation between the fluid inertia and surface tension, wherein σ represents the surface tension of the liquid. The Z value can be calculated independ of velocity. Many papers examined the relation between drop formation and the Z number and, generally, a value for inkjet ink between 1<Z<10 is recommended [31, 37, 38].

$$Z = \frac{1}{Oh} = \frac{Re}{\sqrt{We}} = \frac{\sqrt{d\rho\sigma}}{\eta} \tag{2.2}$$

$$Re = \frac{\rho d v}{\mu} \tag{2.3}$$

$$We = \frac{\rho v^2 d}{\sigma} \tag{2.4}$$

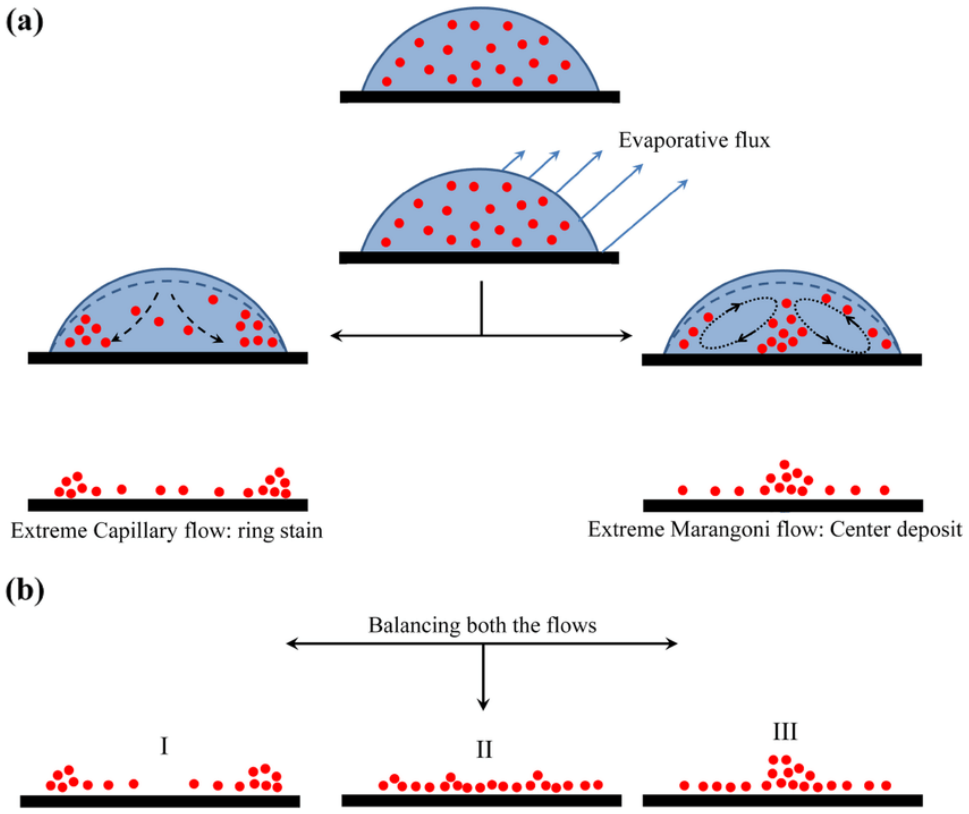

Figure 2.5: Influence of liquid evaporation on particle distribution after drying [36].

2.5 Electrochemistry

As mentioned in Section 2.3, BDD has exceptional properties that make it useful for electrochemistry. The most important properties are chemical stability, low background current, wide potential window and reduced bio fouling [39]. Since the proposed BDD electrode will be used for electrochemical analysis it is important to develop an understanding of electrochemistry and its associated parameters.

2.5.1 Electrochemical principles

Electrochemistry uses electrical stimulation to study the chemical reactivity of a system. It analyses the loss or gain of electrons and, the oxidation or reduction mechanism in the reaction [40]. Oxidation and reduction reactions are called redox reactions.

The electron transfer generally falls in two categories, inner or outer sphere electron transfer. Inner sphere reactions occur at the surface of the electrode and the electron transfer takes place during direct interaction with the electrode surface and the reactant. The electrode material plays an important role in the reaction kinetics. Outer sphere electron transfer occurs near the electrode surface, however there is no direct interaction between the reactant and the surface. Electron transfer happens through quantum tunnelling.

Possible electrochemical detection methods are voltammetric, amperometric, potentiometric, conductometric, and coulometric measurements. The most common method for electrochemical reduction and oxidation processes is cyclic voltammetry. In voltammetry a constant or varying potential is applied, and the current is measured [41].

During cyclic voltammetry, reduction and oxidation peaks can be observed. The peaks give information on the thermodynamics of the redox processes and on the kinetics of electron transfer.

2.5.2 Electrodes

It is common to work with a three-electrode system in electrochemical experiments whereby each electrode has a different function in the system. Figure 2.6 shows a schematic representation of such a system. The three electrodes are the working electrode (WE), counter electrode (CE) and reference electrode (RE). The electrodes should be chemically inert to prevent interference with the electrochemical process.

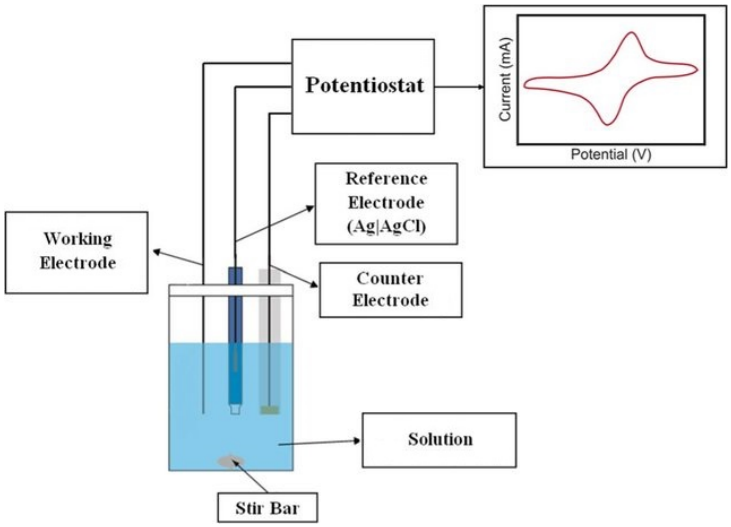

Figure 2.6: Schematic representation of an electrochemical cell with a three-electrode system [42].

The potential of the voltammetry experiment is controlled between the WE and RE. The current flows between the WE and CE when a potential is applied, while the chemical reaction of interest occurs at the WE surface.

A few important conditions need to be fulfilled for the proper performance of the electrochemical experiment. To reduce ohmic losses between the RE and WE, and to be able to accurately determine the applied potential at the WE, the RE should be placed as close as possible to the WE.

The RE should have a well-defined, stable equilibrium potential. There are some common materials used as reference electrodes of which the standard potential in a typical solution is known. These include the saturated calomel electrode (SCE), standard hydrogen electrode (SHE) and the Ag/AgCl electrode [41]. RE of these materials are used as a reference point to determine the applied potential by the WE. The applied potential during an electrochemical experiment is therefore always described in comparison to the specific RE used during the experiment.

The CE's total surface area must also be larger than the surface area of the WE to allow unrestricted current transfer into the system and prevent this from becoming a limiting factor in the kinetics of the electrochemical process [43].

2.5.3 Solvent window

The solvent window defines the potential window over which the electrode can operate before the solvent is electrolysed. Its wide potential window, as depicted in Figure 2.7, distinguishes BDD electrodes from other types of electrodes. A BDD electrode above metallic conduction threshold and with a low sp^2 content has a potential window of 3.7V in aqueous media.

To characterize the BDD electrode, cyclic voltammetry (CV) is performed in a three-electrode system with only a solution of H_2SO_4 electrolyte. This should show the characteristic behaviour of a BDD electrode as shown in Figure 2.7. Other typical electrolytes for the characterisation of BDD are

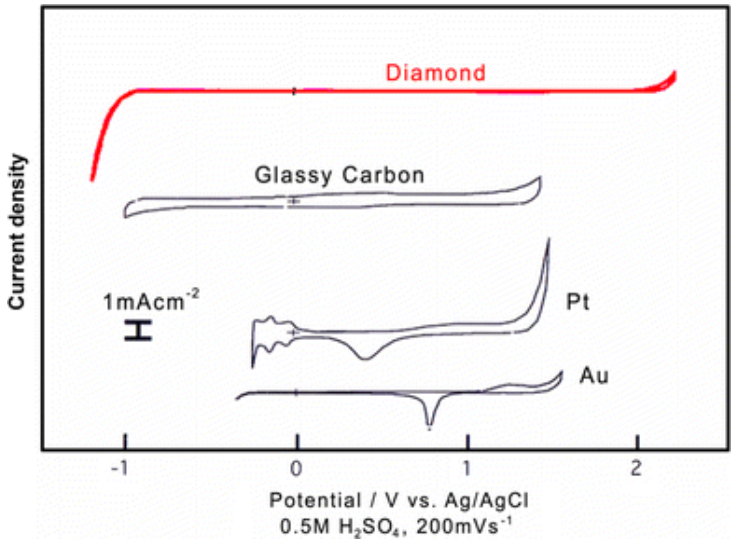

Figure 2.7: Potential window of BDD versus other common electrode materials [44].

$Fe(CN)_6^{-3/-4}$ and $Ru(NH_6)^{3+/2+}$ which are inner and out sphere redox couples respectively and their presence in the electrolyte leads to a reversible electron transfer process indicating behaviour similar to the illustration of Figure 2.8a.

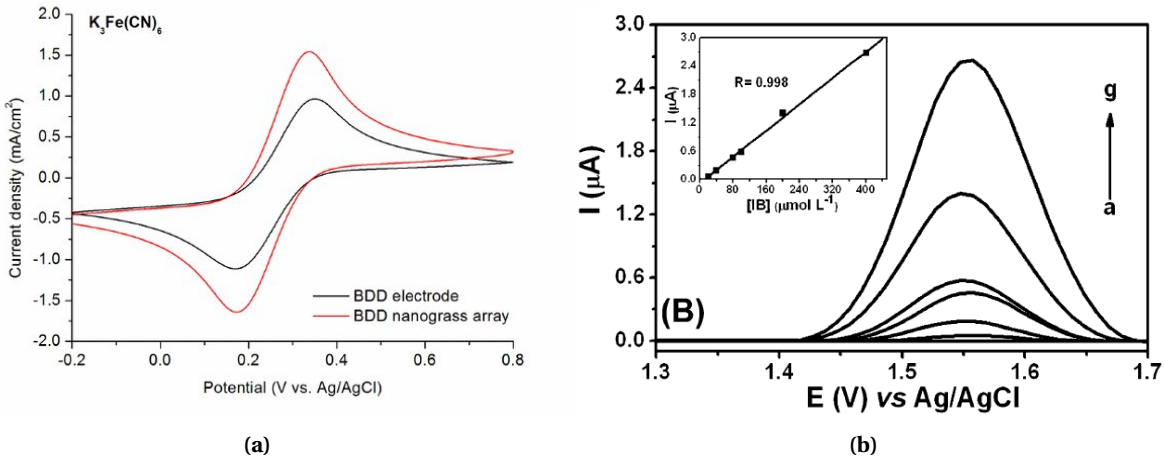

Figure 2.8: Voltammetric curves of two analytes, **(a)** CV curve of 5 mM $Fe(CN)_6^{-3/-4}$ [45] and **(b)** DPV at BDD in 0.1 mol L^{-1} H_2SO_4 in 10% ethanol (a) containing ibuprofen at the following concentrations (mmol L^{-1}): 20 (b); 40 (c); 80 (d); 100 (e); 200 (f); and 400(g) [46].

2.5.4 Electrochemical analysis

The goal of electroanalysis is to find the presence or a specific quantity of an analyte in a solution. By means of analysing a well-defined oxidation peak, these quantities and the limit of detection of the electrode can be determined. Figure 2.8b illustrates a differential pulse voltammetry (DPV) graph with different concentrations of ibuprofen, wherein an increasing concentration of ibuprofen results in an increase of the oxidation peak current. From this graph, a behaviour correlation between current of the oxidation peak and analyte concentration can be indentified. Ibuprofen is one of many possible micropollutants in wastewater which can be detected using BDD electrodes. Moreover, the analyte dopamine has been demonstrated with the use of nitrogen incorporated diamond [4, 47] and

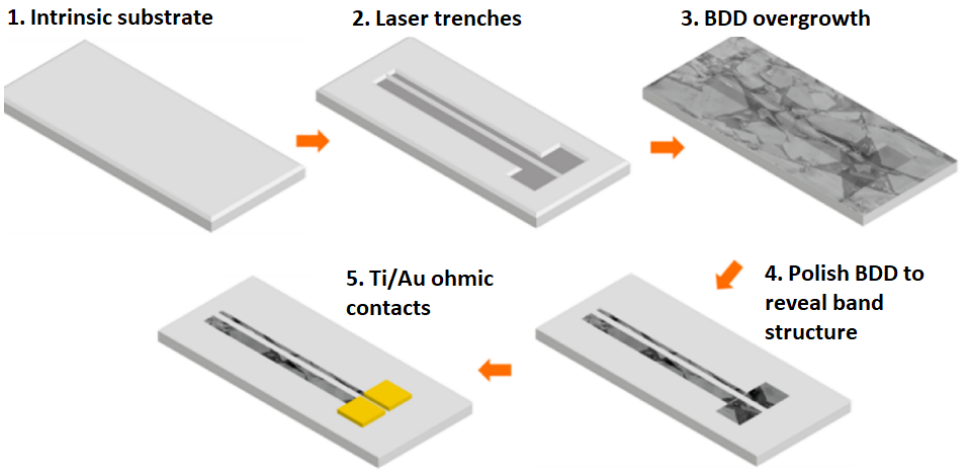

Figure 2.9: The production process for all diamond band electrode [56].

BDD electrodes [48, 49]. Baluchová et al. [50] reviewed over 340 references in the field of electroanalysis of various organic compounds and biomacromolecules.

In addition to these organic compounds, BDD electrodes have also become an important tool for heavy metals detection [51–53] as toxic heavy metals can cause serious health issues through contaminated water, even at trace levels.

2.6 Electrochemical sensor design

Based on the requirements for electrodes and electrochemistry, a sensing chip electrode with a three-electrode configuration can be designed. This section reviews different electrochemical sensor designs, such as BDD electrodes and electrodes made from materials with production processes similar to those aimed for during this project.

2.6.1 Boron-doped diamond electrodes

Traditionally, BDD electrodes are produced from thin-film BDD where the electrode geometry is created by top-down processes. Diamond is selectively removed by reactive ion etching (RIE) [3, 54], focussed ion beam (FIB) or by laser ablation [55, 56]. Sbartia et al. [55] used a laser-machined BDD microcell to detect heavy metal ions, in wastewater, runoff water and rainwater. The electrodes (WE,CE, pseudo-reference) were created by machining a resistive barrier using a laser. Bitziou et al. [56] demonstrated the fabrication of an all-diamond electrode by using laser micro machining, as depicted in Figure 2.9. Figure 2.10 indicates the steps to fabricate a microfluidic device with BDD electrodes, as demonstrated by Watanabe et al. [57].

There are other examples of diamond electrodes grown using selective seeding. For example, the group of Bonnauron et al. [58] used a photoresist mask that was seeded with DND. After removing the mask, their patterned nanodiamond remained, as demonstrated in Figure 2.11a. The first example of diamond seeding using an inkjet printer was reported in 2008 by Chen et al. [59, 60], who suggested the possibility of growing diamond patterns, by selective seeding with a Dimatrix materials printer. The result of their procedure is shown in Figure 2.11b. No actual functional devices were created using this technique until 2019, when Sartori et al. [16] demonstrated the growth of diamond disk micro-resonators, which can be used as highly sensitive mass sensors.

2.6.2 Inkjet printed electrodes

Inkjet printing is a newly emerging technique for the production of electronic devices and electrochemical sensors. Metal NPs of gold, copper or silver are mixed with the inkjet ink to create highly

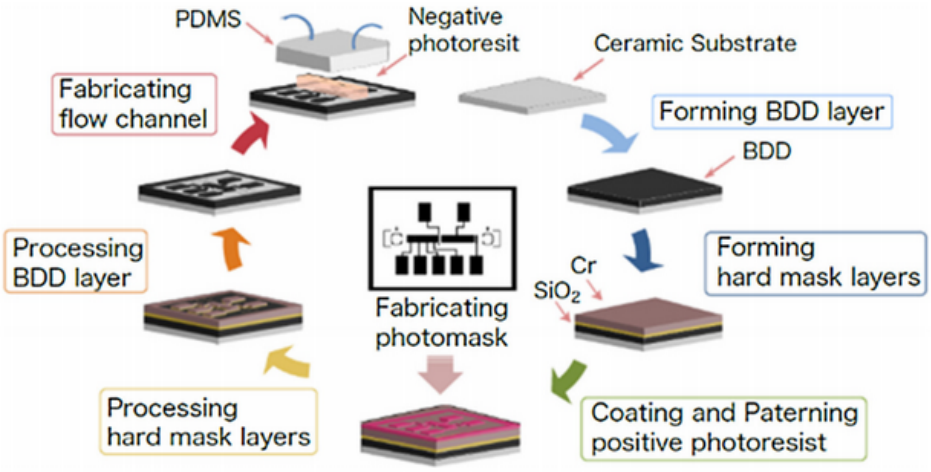

Figure 2.10: The manufacturing steps for a microfluidic device with BDD electrodes [57].

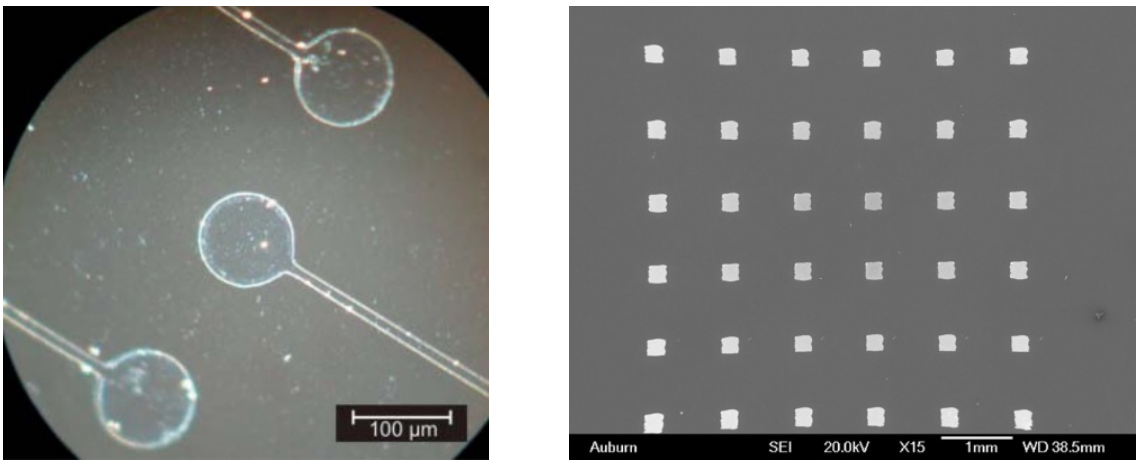

(a) **(b)**

Figure 2.11: Examples of patterned diamond: **(a)** dark field observation of nanoseeded diamond before growth [58] and **(b)** patterned diamond using a Dimatrix printer [59].

conductive tracks. Due its higher conductivity and lower cost compared to gold, silver is one of the most common metallic print materials. Although copper is less expensive it suffers from high oxidation. There are examples of inkjet printed electrochemical sensors, however most are based on printing on polymer, paper or glass substrates [27, 61, 62], which are not applicable substrates for the growth conditions of CVD diamond. Figure 2.12 demonstrates the process steps for inkjet printing a glucose sensor on a Polyethyleentereftalaat (PET) substrate. Figure 2.13a is the resulting sensor on the flexible substrate. The paper based electrochemical sensor illustrated in Figure 2.13b is used for the detection of glucose, lactate and uric acid [63]. The interaction of the droplets on a larger surface are less of a concern for inkjet printing of electronic tracks. These methods rely on depositing large quantities of droplets which merge together in an annealing step to form a conductive surface. A difficulty in seeding for diamond growth is that agglomeration of diamond NPs can have a negative effect on the growth of the thin film diamond, e.g. in terms of thickness and uniformity. Typically, conductive inks contain a weight percentage of 20-70%, and multiple passes over the same print area are frequently used to increase the film thickness. After printing, silver ink is sintered on a hotplate

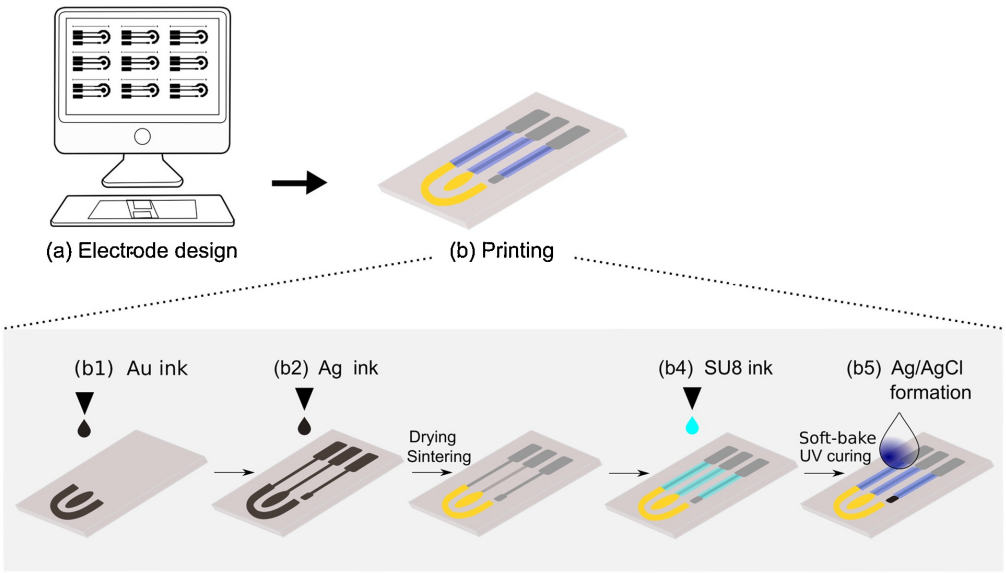

Figure 2.12: the inkjet processing steps of glucose sensor on flexible PET [65]

(a) **(b)**

Figure 2.13: Examples of inkjet printed electrodes with **(a)** the resulting electrode of Figure 2.12 [65] and **(b)** shows a paper based electrochemical sensor for 3 different analytes [63].

or oven at temperatures ranging from 100-160 $^{\circ}C$ for 5 to 90 min. More recently studies have shown sintering of print silver tracks by employing UV light [64].

2.6.3 Screen printed electrodes

Screen printing, while similar to inkjet printing, is a process with a long history for production in a different field. Screen printing is mainly used in the textile industry to produce logos or labels. More recently, it has become a common technique for electrode production as it allows for low cost, high volume production of electrodes with small feature sizes. The best example of commercialized screen-printed electrodes is the glucose sensor for diabetic patients, which has generated a billion dollar industry [66]. This technique, however, requires different masks for each production step and wastes significantly more ink than inkjet printing, making it costly for low volume production and prototyping. A typical design of a (silver-carbon) screen printed electrode (SPE) is shown in Figure 2.14b, and the production steps are depicted in Figure 2.14a. There is one commercially BDD SPE available from Metrohm DropSens (Spain) [67], of which the RE and CE are manufactured using screen printing technology. The electrode is illustrated in Figure 2.14c.

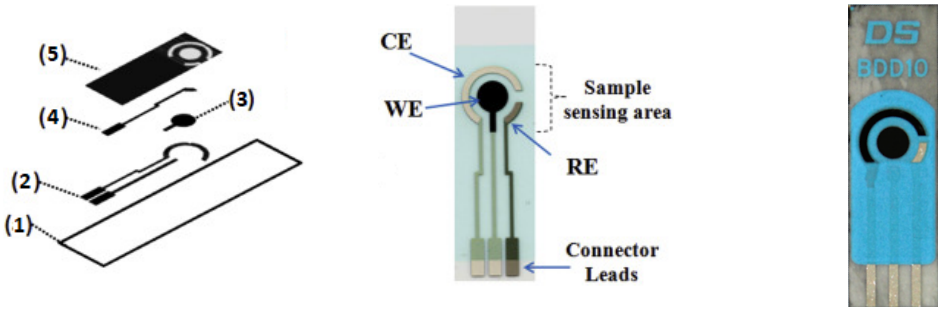

(a) (b) (c)

Figure 2.14: Different SPEs and the required manufacturing steps: **(a)** the production steps each of which needs a different mask, (1) substrate, (2) silver track, (3) carbon layer, (4) silver/silver chloride track and (5) insulating layer [68]; **(b)** example of typical (silver-carbon) screen-printed electrode configuration and **(c)** Metrohm DropSens BDD electrode [67].

2.6.4 Reference electrodes

The reference electrode of the three-electrode system must be coated with silver and silver chloride to create a well-defined and stable potential equilibrium. This process is commonly done through screen-printing, manually applying silver paste or with laser pulse deposition. The inkjet printing process allows for the direct printing of the RE electrode by using ink containing Ag NPs or directly printing Ag/AgCl ink. Another method described by Hyde et al. [69] uses electrochemical nucleation to deposit silver on BDD using a silver nitrate solution. After an anodization process in HCl, Ag can be electrochemically coated to form AgCl. The stability of the AgCl is a concern for solid-state reference electrodes as it is in direct contact with the solution. The reference electrode is therefore sometimes coated with a protective polymer layer of polyurethane [70] or Nafion. The chemical stability and corrosion resistance being important advantages of BDD over other electrode material, additional layers and materials which are in contact with the solution will likely decrease the durability of the electrode sensor. Sbartia et al. [55] used in the development of an all BDD electrode sensor chip for the detection of heavy metal ions a pseudo-reference electrode of BDD, similar to Ensch et al. [71], who measured the quasi-reference electrode potential against a commercial Ag/AgCl RE.

2.6.5 Ohmic contacts

Low contact resistance is important for high performance of the device and higher accuracy of device parameters. An non-ohmic contact displays a non-linear relation between voltage and current between two conductors. Non-ohmic contact between a semiconductor and a metallic material generally originates from a Schottky barrier and can be prevented by the application of specific thin film layers. For low contact resistance between the BDD surface and metallic contacts, several methods are proposed in literature, although the most common method for creating contact pads on BDD is by RF sputtering a carbide-forming layer, usually titanium, followed by the application of a gold layer [2, 72, 73]. It is important that the titanium layer is not exposed to air before deposition of the gold layer to prevent the oxidation of titanium. For semiconducting diamond above a certain boron threshold, silver is commonly used as an electronic contact.

3 Methodology

In this chapter, the methods and techniques employed for the experiments and characterizations are discussed.

3.1 Inkjet Printing

Both printers used during this master thesis project, the Epson XP-235 and the PIXDRO LP-50 printer, are DoD printers, with piezoelectric nozzles. The inkjet printing process was chosen as a bottom-up fabrication technique, because it is a relatively inexpensive, fast and digital process. A distinction in design methodology must be made depending on the printers used. The LP-50 has a motion stage that allows printing in X- and Y directions and has software for the automatic creation of pixel spacing based on droplet size. In case of the Epson printer, however, the default printing on non-flexible substrates or any substrate with a thickness $> 50\,\mu m$ can only accurately be controlled in the motion direction of the printhead. For the Epson printer the individual nozzles and location of the droplets must be addressed manually using a self-composed python script. However, the Epson does possess a high quality printhead with a large number of nozzles (254) and allows simultaneous printing of multiple inks.

As discussed in section 2.2, for CVD diamond growth the substrates need to have a high enough nucleation density to be able to grow a closed thin-film diamond surface on the substrate. The print seeding was done with in house developed inkjet ink containing nanodiamond particles to selectively increase the seeding density. The inkjet ink was a mixture of different ratios of water and glycerol, to which the mother solution 5% (wt/vol) NanoAmando aqueous colloid (NanoCarbon research institute Ltd., Japan) was added.

3.1.1 Epson XP-235

The Epson XP-235 is a low-cost consumer inkjet printer developed by Epson. It employs the piezo DoD technique and is equipped with a printhead containing 256 nozzles. Different inks can be loaded by replacing the standard ink cartridge with a refillable cartridge. The nozzles can individually be addressed using the software developed in an earlier project by Waasdorp et al. [74]. This printer has been chosen as part of the project because it is a continuation of the department's earlier research done on selective seeding and inkjet printing. The software was further optimized during this master thesis project to be able to directly send print files to the printer on Windows systems. By selecting specific nozzles, a bitmap image representing the design can be generated and deposited on the substrate, as shown in Figure 3.1b. By loading multiple cartridges with different inks, the EPSON XP-235 can print multiple materials in the same print. The printhead of the Epson XP-235 is divided into two columns of 127 nozzles. One column consists of all black nozzles, and the other is connected to the cyan, magenta and yellow ink cartridges, as illustrated in Figure 3.1a.

Since the printer is developed for printing on paper, its mechanics are not suited to print on hard substrates such as glass or silicon. For this reason part of the bottom was removed using a milling process to accommodate a glass slice and print with the correct print gap, as depicted in Figure A.6. Also, given the incapability of printing in the paper feed direction, the resolution of the printer in this direction is limited by the printhead geometry. This results in a minimum drop spacing of approxi-

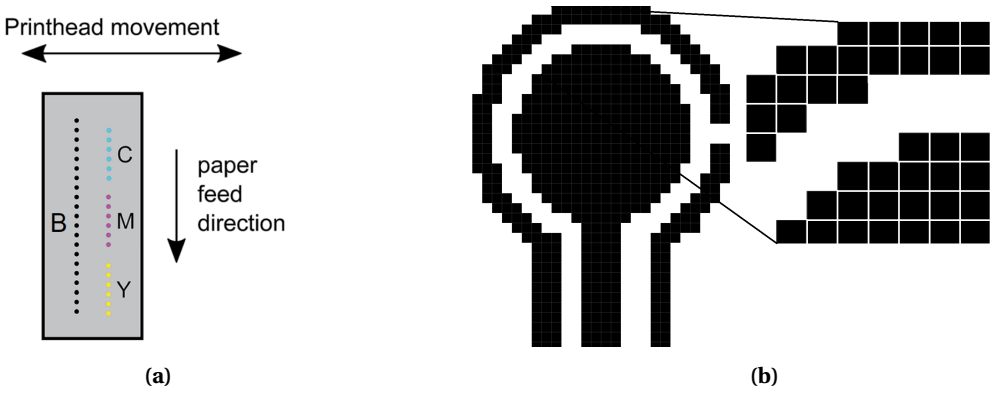

Figure 3.1: (a) The nozzles arrangements and printing directions of the Epson printer [74] and **(b)** formation of an image represented by squares based on pixels/droplets.

mately $\frac{1}{120} inch$ or $\approx 210\,\mu m$. Methods to bridge this drop spacing and to print continuous shapes, which are required for conductive tracks, were changing the surface energy of the substrate to affect the wetting of the droplets on the surface, as will be discussed in Section 3.1.5, and the implementation of a small motion stage. Additional information on printing with the Epson printer is provided in the appendices. Appendix A provides a step by step guide for using the Epson printer. Given, to print with the EPSON printer, all print nozzles must work. Appendix B therefor includes different techniques for unclogging the nozzles. Although the EPSON printhead is resilient in printing with many liquid types, one or more nozzles frequently clog, which creates a defect in the printed pattern.

To develop an understanding of the limitations of the Epson printer, it is important for the reader to have some understanding of the printing process with the hacked configuration. Figure 3.2 illustrates a brief example script for printing the letter *P*. The start of the script defines the spacing of the droplets. As previously mentioned, the separation between the individual nozzles is 1/120 inch; so there is no control over the *dy* direction. However, the distance between vertical lines can be controlled by changing the *dx* value. In this example, there is equal spacing in x and y directions given that $dx = \frac{1}{120}\, inch$. With the list definition, lines 7-9, different nozzles can be selected for the vertical print lines. The letter *P* in this example is printed using three vertical lines. The first list addresses nozzles 1-5 of the available 42 nozzles in each colour. The second list addresses only two nozzles, and the third addresses three nozzles. The image is created by determining the horizontal position of the nozzle lists, lines 20-22. Furthermore, for every nozzle list a specific colour can be selected from the graphical user interface (GUI), representing the different inks. To print with different inks or colours at the same time, the colours must be hard coded. In addition, droplet sizes can be selected based on the three available options from the Epson firmware. All printed patterns with the Epson printer were printed with the large droplet, approximately 12 pL, making it easier to cover the *y* gap between droplets.

```
1
2   def createPs(x, r=b'\x00', size=1, **kwargs):
3       dy = 0
4       dx = (dy + 1) * (1 / 120)
5       hor = 5760
6
7       list1 = createnozzlelistsp(42, [1, 2, 3, 4, 5])
8       list2 = createnozzlelistsp(42, [1, 3])
9       list3 = createnozzlelistsp(42, [1, 2, 3])
10      m = len(list1)
11      prefix = b'\x1b' + str_hex('i')  # ESC i
12      c = b'\x01'  # COMPRESSED
13      b = b'\x02'
14      n = 1
15      nL = dec_hex(n % 256)
16      nH = dec_hex(n / 256)
17      mL = dec_hex(m % 256)
18      mH = dec_hex(m / 256)
19
20      image = ESC_dollar(hor, x) + ESC_i_nrs(list1, r, size) + \
21              ESC_dollar(hor, x + dx) + ESC_i_nrs(list2, magenta,size) + \
22              ESC_dollar(hor,x + 2 * dx) + ESC_i_nrs(list3, black2, size)
23
24      # suffix1 = b'\x0d' #b'\x0d\x0c'
25      total = image
26
27      return total
```

Figure 3.2: Example script for printing the letter P.

3.1.2 PIXDRO LP-50

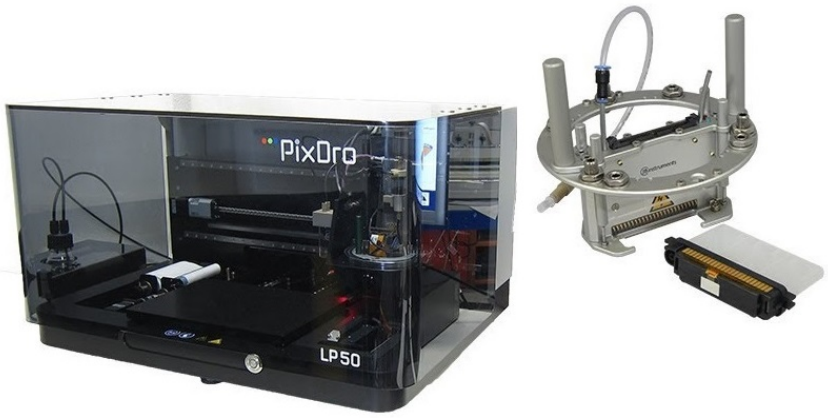

Figure 3.3: The PIXDRO LP-50 commercial research printer and DMC printhead module, which allows printing of DMC-116 cartridges

The PIXDRO LP-50 depicted in Figure 3.3 is a research grade desktop printer newly acquired by the PME department. The PIXDRO printer allows control over the printing process with high resolution, and it employs DoD with piëzo active nozzles. The PIXDRO LP-50 can be equipped with control units and supports printing with printheads of different manufacturers such as Dimatix, Konica Minolta, OCE and Xaar. The printer is aimed at developing inkjet inks, -processes and -applications. It prints on a heated vacuum bed of 227 x 327 mm^2, can be controlled on 4-DOF, and has an accuracy of about $\pm 15\,\mu m$ and a precision of $\pm 5\,\mu m$ in the X and Y axis. The printing in this thesis project was done with DMC printheads. The DMC-11610 and DMC-11601 cartridges, are disposable and print in two volumes. The last two digits of the cartridge dictate the general dropvolume in picolitres. The DMC-11601 prints with a higher resolution due to the smaller drop volume but has, an increased

printing time. Both printheads are equipped with 16 nozzles that can be individually controlled. All prints in this thesis project are performed with a single nozzle active, due to the inconsistency among the different nozzles. The nozzle diameters of the DMC cartridges are squares of $\approx 9\,\mu m$ and $\approx 21\,\mu m$ for the 1 and 10 pL printheads, respectively. The DMC printheads are specifically designed for development of printing inks, costing a fraction of the price of the other available high quality printheads. The printing was done with a 1mm gap between the printhead and the substrates, while maintaining a printhead temperature of 29°C. The larger printhead DMC-11610 was chosen for most prints due to shorter print times. The minimum feature size that the 10 pL printhead could produce was in the range of $50-70\,\mu m$. Since currently only one printhead can be equipped at a time, the PIXDRO was not able to print multiple materials at the same time, unlike the EPSON printer. The default print settings for the PIXDRO LP-50 is unidirectional printing in the Y normal direction; see Figure 3.4. The printhead moves into position and while ejecting droplets the motion stage underneath moves up, creating vertical lines on the substrate. With bi-directional printing the printhead prints in both the up and down movement of the motion stage, resulting in shorter print times. Unidirectional printing is however chosen over bi-directional printing, due to it producing better quality prints. The trajectories of the droplet in flight, during bi-directional printing will result in an offset between the up and downward lines.The exact steps for printing with PIXDRO LP-50 are described in Appendix C.

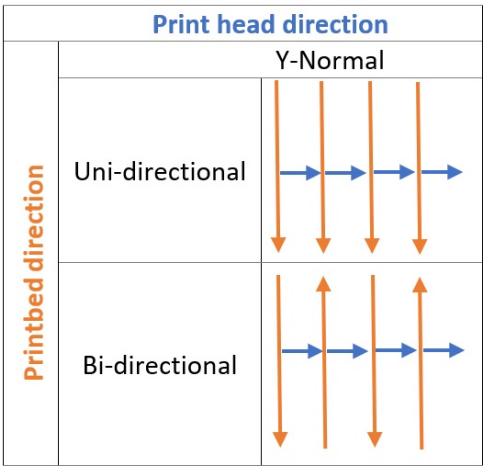

Figure 3.4: Two possible print direction combinations, with Y-normal uni-directional and Bi-directional

3.1.3 Waveform tuning

A separate part in printing with the PIXDRO printer is the tuning of the waveforms for different inks and printheads. Figure 3.5 illustrates the drop view window of the PIXDRO printer. Eleven different parameters control the jetting of the droplets. A stroboscopic high speed camera records the ejected droplets and helps with tuning the parameters. The waveform parameters are related to three characteristics, namely the level, duration and rate of change of the waveform. The waveform itself can be separated in five stages. The first section is the standby phase. From the standby phase, the voltage is slowly increased to reduce the volume in the chamber. By then reducing the voltage, inked is sucked into the nozzle chamber, and with a short high pulse, droplets are ejected from the nozzle. The last phase before returning to the standby phase is the damping phase, which creates pressure inside the nozzle chamber and prevents oscillations in the ink chamber. Increasing the voltage level or rate of change of the waveform beyond a certain threshold leads to the formation of satellite droplets. Making it too low or too slow, results in no ejected droplets.

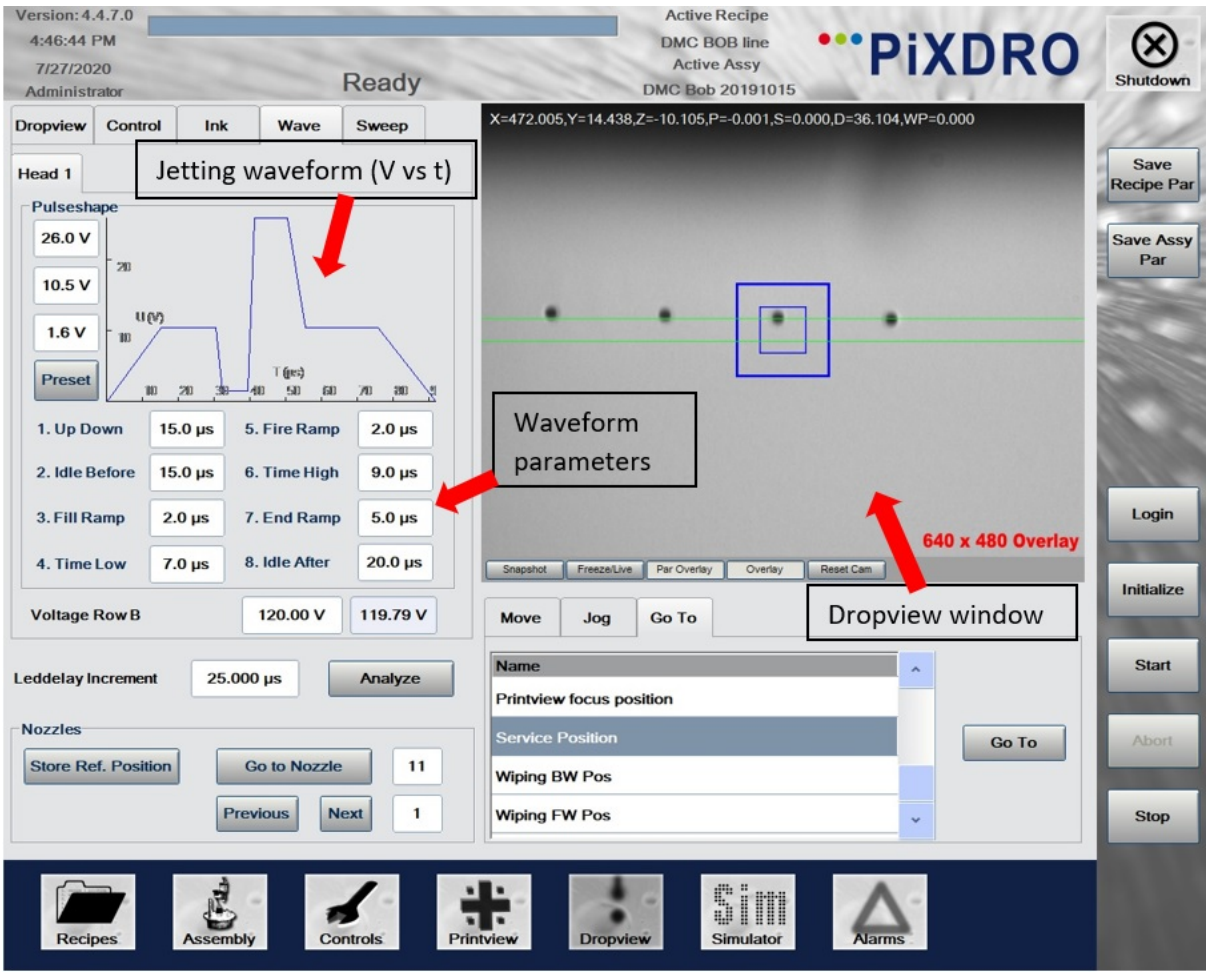

Figure 3.5: Drop view window of the PIXDRO printer.

3.1.4 Printed patterns

The inkjet printed pattern was based on the design of common SPE's. More specifically, it consisted of a circular working electrode in the centre and a circular outer ring of which $\frac{3}{4}$ was dedicated to the CE and $\frac{1}{4}$ to the RE (see Figure 3.1b). Designs used with the PIXDRO printer were made in FUSION 360, and the technical drawings of the design for the proposed BDD sensor are included in Appendix I. The CAD designs from FUSION were converted to black, cropped and saved as bitmap images. These bitmap images could then be loaded into the PIXDRO printing software, called PIXDRO HMI. The electrochemical sensor design was developed such that the lay-out of the leads was the same as the DropSens dimensions. The same spacing of the leads should allow the electrode to connect using the standard DropSens connector cable. To demonstrate the prototyping capabilities of the inkjet printing, some additional geometries were designed, including a 2D heater, an interdigitated electrodes, a geometry commonly used for gas sensing, and a circular electrode. The designs are shown in Appendix I.

3.1.5 Surface treatment

Given that the printing resolution is partly defined by the contact angle the droplets make with the substrate surface, different surface treatments were applied to influence the wetting behaviour. By employing certain techniques, the hydrophilicity of the surface could increase. The techniques in this thesis project were acid cleaning, oxygen plasma treatment and air-exposure after oxygen plasma treatment.

Figure 3.6: Optical photograph of the front control panel of the Diener Femto plasma setup used for surface treatmentr

Using acid treatment in a solution of $H_2SO_4 : HCl : HNO_3$ 2:2:3, diced silicon samples were heated until the colour of the solutions changes. This method removes any organic contaminants on the surface and increases the wettability of the substrate.

Samples were also treated with a Diener plasma tool fig. 3.6 at two powers, respectively for treatment times of 3 min at 80W and 2 min at 20W. The 80W for 3 min is the most common cycle employed in the department, while the shorter cycle was used to make the surface less hydrophilic. During plasma treatment, the air is ionized, and reactive species of the feeding gas break down larger carbon species on the surface of the substrate. Oxygen plasma is also known for the formation of different

oxygen-rich functional groups and dangling bonds on the substrate surface, making the surface more hydrophilic. After surface treatment, the dangling bonds react with water, surface impurities or other dangling bonds, which reverses the process over time.

3.1.6 Inkjet inks

Since the ink in the inkjet printing process must satisfy specific rheological conditions, it is advised to evaluate the liquid based on parameters that predict the printability. Some examples of these requirements are surface tension of the liquid, viscosity and particle size (Z-avg). The requirement for particle size in relation to the diameter of the printing nozzle dictates that the particle size should be at least 100 times smaller. For the DMC-11610 with a nozzle of 21 μm, particles should be less than 210 nm, and for the 1 pL printhead less than 90 nm. Most printing was done with a mixture of glycerol (Sigma Aldrich ≥ 99.0%) and DI water (18.2 $M\Omega.cm$). Glycerol was chosen for this solution for its miscibility, high boiling point(290 $^{\circ}C$), high viscosity (900 mPas at 25$^{\circ}C$) and non-toxicity. For silver printing, a commercial silver ink Metalon® JS-B25P (Novacentrix) of 25% wt silver NPs and, Z-avg particle size of 75 nm was used. The tests were performed using tri(ethylene glycol) monoetyhlether which is a single liquid that meets all printer requirements and ethylene glycol, a common inkjet printing liquid due to its low surface tension. The following Table 3.1 shows calculated ink properties based on Equation (2.2), Equation (2.3) and Equation (2.4) for print liquids used during this thesis project.

Table 3.1: Theoretical and calculated ink values at 25$^{\circ}C$ *(*Droplet velocity and nozzle diameter are assumed 6 m/s and* 21 μm*)*

Mixture	Viscosity (mPas)	Surface tension (mN/m)	Re	Weber	Z number
Water	1	71.2	147.6	12.3	41.8
Wat:Gly (3:2)	4	69 [75]	47.5	16.5	10.1
Wat:Gly (1:1)	6.8	68 [75]	21.7	13.4	6
Metalon JS-B25P	5	31	33	31.9	5.8

3.1.7 Contact angle measurement

As discussed earlier, the resolution of the inkjet printing process is partially defined by the contact angle that the droplets make with the substrate surface. This contact angle depends on the surface tension of the liquid, the surface free energy of the substrate and the interfacial tension component, which is described by Young's equation in Equation (3.1), wherein γ_{sg} is the surface energy, γ_{sl} the interfacial free energy, γ_{lg} the surface tension and θ the contact angle. A high contact angle indicates that the surface has poor wetting properties. The contact angle of the liquid-solid interface is closely related to the surface tension of the liquid itself and the surface free energy; this relation is illustrated in Figure 3.7.

$$\gamma_{sg} = \gamma_{sl} + \gamma_{lg} \cdot cos\theta \tag{3.1}$$

The contact angle measurements are performed on a Theta lite optical tension meter (Biolin Scientific). Drops with a volume of 3 μl were dispensed for all tests. The effect of the drop volume on measuring contact angles is described by Krüss [77]. Any volume between 1 – 10 μl should yield the same results for the test as long as the drop volume of all individual tests is the same. Upon contact with the surface, a camera records the stabilization of the droplet measuring the contact angle during the first 10 s with 17 Hz.

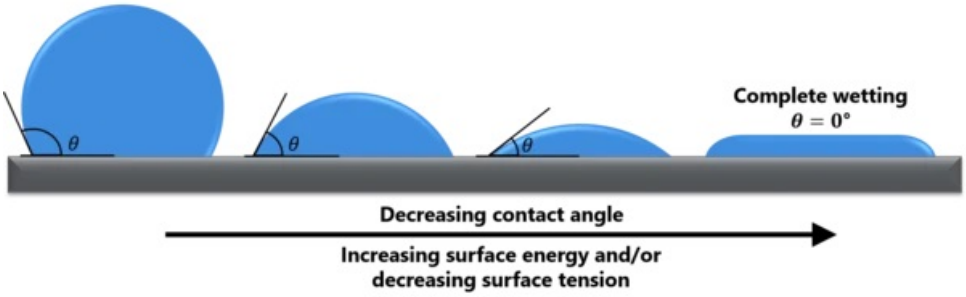

Figure 3.7: Contact angle of a liquid with increasing surface energy or decreasing surface tension [76].

3.1.8 Surface free energy

Apart from determining the contact angles the inks make with varying substrate treatments, the contact angle measurement also allows to determine the surface free energy of the substrate. To determine the surface energy of the substrate, the contact angles of three different components were analysed. The test liquids consisted of two polar liquids, MillQ DI water ($18-20\,M\Omega.cm$), ethylene glycol and the non-polar liquid diodomethane 99% (Sigma-Aldrich). The properties of the test liquids are noted in Table 3.2. The surface free energy was determined by various interactions of inter molecular forces [78].

Table 3.2: Surface tension components of the three test liquids used for the surface free energy assessment.

Test liquid	**Surface tension,** $\gamma_{tot}(mN/m)$	**polar,** $\gamma_p(mN/m)$	**dispersive,** $\gamma_d(mN/m)$
MillQ DI water	72.8	51	21.8
Ethylene glycol	48	19	29
Diiodemethane	50.8	50.8	0

3.2 Diamond synthesis

3.2.1 Nucleation density

Print techniques with various concentrations of diamond NPs resulted in varying seeding densities on the substrate surface. By investigating the substrate using high resolution SEM images, the substrates were checked in terms of seeding density and number of surface agglomerations counted by means of ImageJ. The results of inkjet printing were compared to a standard spin-seeding procedure similar to [79].

3.2.2 CVD reactor

Diamond was grown in the in-house built HFCVD reactor, depicted in Figure 3.8. The nucleation takes place near a tantalum hot filament powered to around 425W, the sample stage was set to $725°C$ and flow of feed gas were 300 sccm H_2 and 6 sccm CH_4, resulting in the growth of NCD.

3.3 Characterization

3.3.1 DropSens electrode

A partially SPE electrode from DropSens DRP-CBDD10 (batchnummer:M191002) was acquired to gather information on the chip electrode production and design. The electrode was characterized based on its electrochemical properties and physical properties. To be able to determine the thick-

Figure 3.8: The in-house built HFCVD reactor.

ness of the functional layers of this electrode, the electrode was diced through the centre of the WE electrode and cast in a conducting polymer allowing to be imaged under the SEM. It was then sanded with different grit sizes on disc sanders. The sample was sanded in small steps, from grit 80 up to grit 3000. By rotating between each sanding step and ensuring that all scratch marks run in the same direction, the process could be visually inspected to determine if the entire surface had been sanded to the current grit. After the sanding process, two more polishing steps were applied to develop a smooth surface.

Electrochemical characterization of the DropSens was done using cyclic voltammetry with an Autolab M101 potentiostat by dipping the electrode in a solution of 0.1 M KCl (Sigma-Aldrich, ≥ 99%) containing either 1 mM $Ru(NH_3)_6{}^{3+/2+}$ or 1 mM $Fe(CN)_6{}^{3-/4-}$. The DropSens is a chip electrode comprising, a BDD WE of 10.18 mm^2, a carbon CE and a silver RE. The experiments were performed using Nova software and further processing was done using an in-house developed MATLAB script.

3.3.2 Rheometer test

To determine the viscosity of the printing ink, which is an important property for the flow behaviour during droplet formation. A rheology test was performed on a Anton Paar Rheometer MCR 302. For this study, a conical measurement plate CP-25 and a parallel PP-50 were used. The conical plate allows for a uniform shear-rate and the larger diameter of the PP-50 results in increased torque. This helped reducing the measurement error from the minimum resolution of the torque measurement. Since the shear rate of the liquid in the piezo nozzle is different throughout the stages of drop formation. The test is performed with a shear sweep between 10 s^{-1} and 1000 s^{-1}.

3.3.3 Dynamic light scattering measurement

Dynamic light scattering (DLS) is a technique that uses light scattering of particles to determine particle size and particle size distribution in a solution on the nanometer scale. A laser with a known wavelength is scattered on the small particles in the solution. Many properties influence the scattering behaviour such as the refractive index of the liquid, laser wavelength, the incident beam angle and absorption coefficient. The light scattering is related to the brownian motion of the particles. Smaller particles have faster brownian motion this results in a faster change in the light scattering intensity. Larger particles scatter more slowly and give a slower change in intensity. The change in

time gives a correlation function depending on particle size. Solving the correlation function results in the solution's diffusion coefficient, from which using the Stokes-Einstein equation the diameter of the particles can be determined.

As agglomerations of the nanoparticles can have an effect on the growth of the diamond thin film, Nanocarbon recommends not storing any solution containing less than 1% (wt/vol) for an extended time and recommends seeding with a concentration of .2% (wt/vol) [80]. To check for agglomerations tests were performed on a Zetasizer Nano ZS available at the Faculty of Applied Sciences to monitor the agglomeration behaviour of the nanoparticles in the inkjet ink. The ink was diluted in milliQ water. A refractive index of 2.41 and absorption of k=0.0 were chosen for this experiment.

3.3.4 Raman spectroscopy

To investigate the crystalline quality of thin-film diamond, Raman spectroscopy is likely the most widely used characterization technique. Raman spectroscopy is a non-destructive method that can be used to analyse the carbon bonding structure and obtain information about the diamond film quality and composition [20]. Raman spectroscopy relies on the inelastic scattering of photons, also referred to as Raman scattering. The incident photon from a light source or laser beam interacts with the molecules of the target material. Due to this interaction there is an increased energy state of the target molecule, changing the energy of the emitted photon. By measuring the intensity of the inelastic scattering these emitted photons have a lower of higher energy state than the incident photons, giving information on the composition of the target. By analysing the peaks in the Raman plot on diamond samples, information about the different states of carbon can be acquired. Pure diamond only contains sp^3 carbon, resulting in a single Raman peak at 1332 cm^{-1}, or the so called diamond peak. A broad band around 1550 cm^{-1}, the G band, specifies the presence of graphitic carbon diamond film, whereas the A band in the 1480 cm^{-1} region specifies the presence of amorphous carbon and a small peak near 1140 cm^{-1} originating from trans-polyacetylene usually indicates the formation of NCD or UNCD film microstructure [12, 81]. The presence of metallic conduction levels of boron doping in BDD shifts the diamond peak (1332 cm^{-1}) from its specific position to lower values and a additional boron-carbon peak is visible in the 500 cm^{-1} range.
The Raman tests analyses in this study were performed using a Horiba LabRAM HR with a 50x magnification lens, a laser wavelength of 514 nm, integration time of 1 s and 5 accumulations.

4 Results and discussion

In this chapter, the experimental results will be discussed. The chapter starts with the properties of the inkjet ink on the drop formation. Followed by how the printer parameters affected the inkjet print seeding results. The description of the effect of the printing steps is based on printing with the PIXDRO LP-50 printer. The liquid-surface interaction and the nanodiamond particle distribution is investigated followed by how the different inkjet seeding methods influence the diamond thin-film formation. To demonstrate the possibility of seeding using inkjet printing using low cost equipment, a similar process is demonstrated using an Epson printer. This chapter will then characterize a commercial sensor chip electrode, fabricated using a combination of CVD and screen printing. The combined information from this chapter serves as a guideline for future fabrication of a BDD chip electrode based on inkjet printing methods.

4.1 Inkjet ink

The most important aspects for the drop formation during inkjet printing, such as consistent jetting, an uniform jetting velocity and trajectory and the absence of satellite droplets are all determined by the properties of the inkjet ink. The basis for successful inkjet printing, the ink characterization results and how the ink properties affected the inkjet printing process are discussed in the following section.

4.1.1 Ink stability

The diamond ink was developed in house and is a combination of water and glycerol in a 1:1 ratio to which a commercial aqueous solution of diamond NPs was added. Different concentration of water and glycerol were tested as well as different ink solutions. One of the first indicators for the inkjet ink containing particles is the ink stability. Shown in Figure 4.1 are different ink mixtures stored in 10 ml glass bottles. The bottles containing the glycerol ink were stored and used for printing for over half a year and visually no indication of instability through sedimentation from the mixture can be detected. The tri(ethylene glycol) monoethylether to which the mother solutions was added, began to precipitate over time. Ethylene glycol did not show the same phase separation, however clusters of particles could be observed on the wall and bottom of the glass bottle after storing them for several months.

4.1.2 Ink viscosity

Secondly as previously discussed in Section 3.1.6, to predict printability of the inkjet ink, the ink should fall within a specific region of Z value. This Z value is mainly related to the surface tension and viscosity of the inkjet ink. The theoretical Z value, 6, for this specific ratio of water glycerol mixture is based on a viscosity of 6.8 mPa s. However, glycerol is very hydrophobic and is known to absorb twice its own mass in water over time. Furthermore, the viscosity of glycerol drops very rapidly with the absorption of water, one percentage of water uptake results in a decrease of the dynamic viscosity from 900 mPa s to around 770 mPa s. Measurements showed that the viscosity value of the stock solution of glycerol was already at a viscosity of 718 mPas, lower than the theoretical value of 900 mPa s for pure glycerol at 25°C. Potentially due to water uptake of the glycerol.

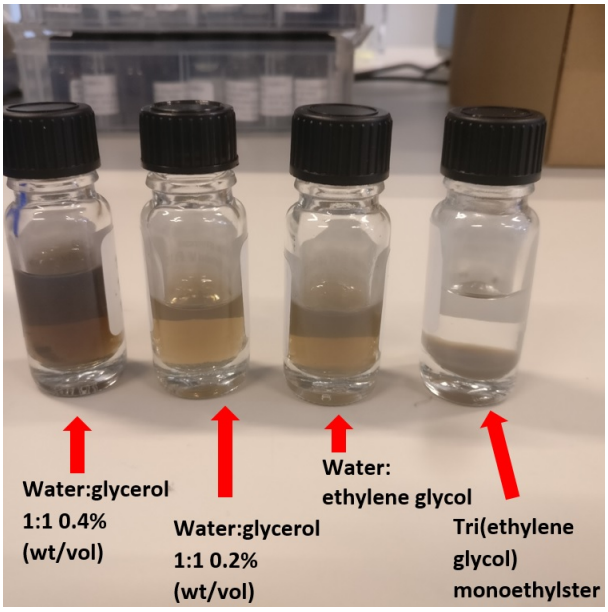

Figure 4.1: From left to right, four 10 ml bottles containing different print liquids, water:glycerol with 0.4% (wt/vol), water:glycerol with 0.2% (wt/vol), water:ethylene glycol 0.2% (wt/vol) and tri(ethylene glycol) monoethylster 0.2% (wt/vol).

To determine the viscosity of the ink, test were performed using the Anton Paar rheometer. The measured viscosity (6 mPa s) at high shear rates, of the water:glycerol mixture is in good agreement with the theoretical value for 50:50 vol.% at 25°C (see Table 3.1). Apart from verification between theoretical and actual viscosity value, the test also reveals information about the flow behaviour of the inkjet ink. Although the liquid is a mixture of water and glycerol both Newtonian fluids, during the initial test using the CP-25, the solution containing diamond NPs appeared to show non-Newtonian shear thinning flow as seen in Figure 4.2a. However, this behaviour can also be contributed to the resolution of the rheometer. The minimal measurable rotational torque value is, according to the manufacturer of the rheometer, 1 nNm and the measured torque is in the μNm range, well within the range of the rheometer. However, the CP-25 measurement plate does require low torque values and as such has an increased chance of invalid measurements. Additional tests using a PP-50 measurement plate were performed, the bigger radius of the measurement plate gives a minimum torque value one factor higher. However, the mixture containing diamond NPs still showed shear thinning flow, the results for the PP-50 measurement are shown in Figure 4.2b. The same test has also been performed on a mixture containing only water and glycerol in a 1:1 ratio without the addition of the diamond NPs, using both measurement plates, CP-25 and PP-50. The test with the PP-50 has been repeated several times for both solutions. Although the error between readings is large, potentially due to the variation of liquid volume underneath the measuring plate, the behaviour is consistent. The solution without NPs showed near linear Newtonian fluid behaviour while the ink showed shear thinning. The shear thinning flow of the liquid containing diamond NPs is in agreement with the result found by Vallejo et al [82] who investigated the influence of carbon-based nanoparticles on the rheological properties of water:ethylene glycol solutions.

4.1.3 Ink evaporation

Another important aspect of the ink is the evaporation rate. It affects the deposition of particles during drying as mentioned in Section 2.4.2, it can cause clogging of the print nozzles and it also influences the behaviour during printing as demonstrated in Section 4.9.2 for printing with a commercial silver ink. The evaporation of ink, being a non-azeotropic mixture of glycerol and water, means that

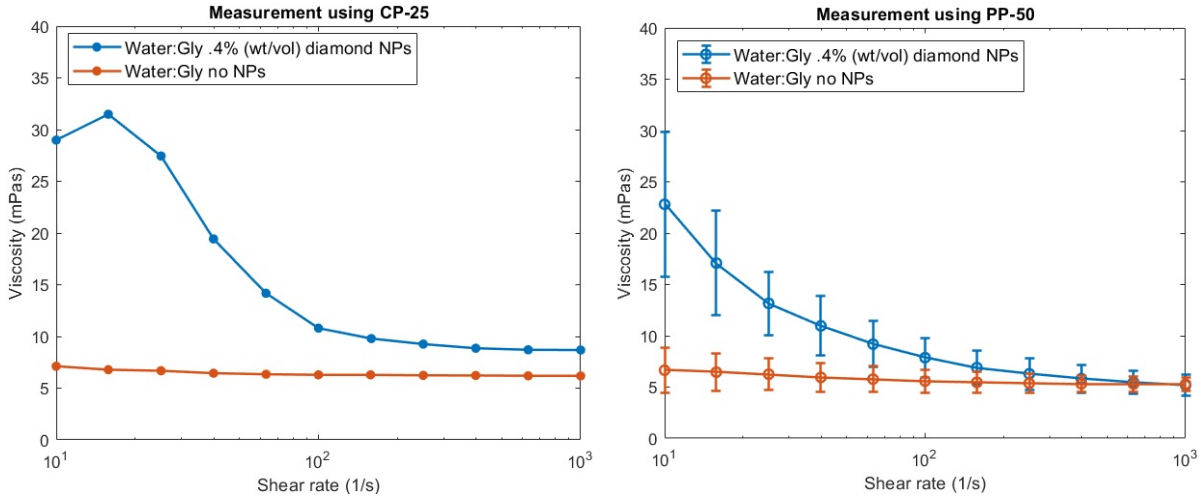

(a) **(b)**

Figure 4.2: Viscosity curves of diamond ink and the solution without nanoparticles, results in **(a)** are based on a single measurement series with the 25mm conical plate and the results in **(b)** are averaged data with standard deviation derived from a total of 3 measurements using the 50mm parallel plate. All experiments are performed at a liquid temperature of 25°C

the boiling point is not altered by the concentration of the solution, but is dependent on the boiling point of the individual components, 100°C and 290°C for water and glycerol respectively. Since the evaporation time for water droplets of picoliter volume is in the microsecond range as reported by [29], water will rapidly evaporate after printing and for the most part the glycerol remains visible, the exact spreading of the droplet is unknown until after CVD diamond growth. At higher contact angles the evaporation effect is reduced as demonstrated by Diddens et al. [83] who modeled the evaporation of water:glycerol droplets and concluded that due to the high viscosity of glycerol, the much lower viscosity of water is blocked from reaching the surface interface and evaporation.

4.2 Print parameters

Specific results related to the printer and printheads on the print quality is discussed in the following section. The print heads used during printing were the DMC-11610 and DMC-11601 cartridges, as depicted in Figure 3.3. For proper droplet ejection careful tuning of the waveform was required. The main aim of the waveform tuning is creating an excitation signal which results in stable drop formation free of satellite droplets. An interesting result is that the drop ejecting with only a single nozzle active is different from all nozzles active. After optimizing the waveform with all nozzles active, for printing with a single nozzle the waveform should be optimized with only one print nozzle active. After proper tuning of the waveform, the print had stable drop formation with circular same size droplets and equal spacing in the y (print direction) and x directions as shown in Figure 4.3.

The tuning of the waveform appeared to be printhead dependent. The same ink on a different, same sized cartridge usually required some altered waveform settings. Even with an 'optimized' waveform, after printing several lines the drop ejecting can change as shown in Figure 4.4a. Where after printing several lines without satellite droplets, the drop formation behaviour changed, resulting in an offset in the print pattern and the formation of satellite droplets on the substrate surface. Finally, the DMC-11601 capable of producing 1 pL droplets, actually ejected droplets in the range of 3-4 pL, reducing the drop volume with the waveform parameters resulted in no drop formation or satellite droplets, potentially due to the composition the ink solution. The waveforms used for different inks with the two printheads are listed in Appendix D.

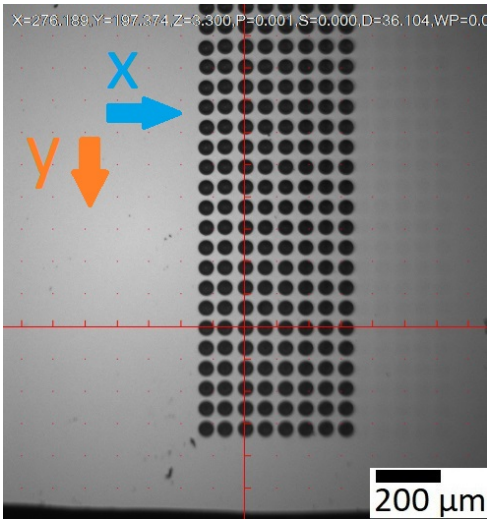

Figure 4.3: Optical image showing a correctly printed pattern with constant drop formation. The print direction is y-normal unidirectional as depicted in Figure 3.4. Note: the offset in printing of the lower left corner of the pattern between the actual print and the programmed position marked by the center of the red axis system, this occurrence is further outlined in Section 4.2.2.

Finally based on the drops per inch (DPI), some of the lines were printed slightly higher or lower with respect to the design. This effect manifested itself once the features of the printer pattern are reduced to the width of a single droplet, a schematic representation of why this happened is depicted in Figure 4.4b. The blue dots are the dots the PIXDRO Human Machine Interface (HMI) decided to print, while the red dot, which doesn't cover enough of the design, is left out. This can be solved by relating the design dimension to the print DPI.

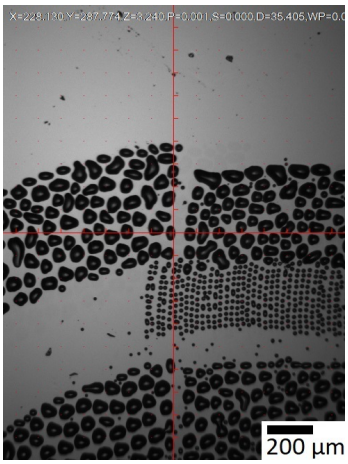

(a)

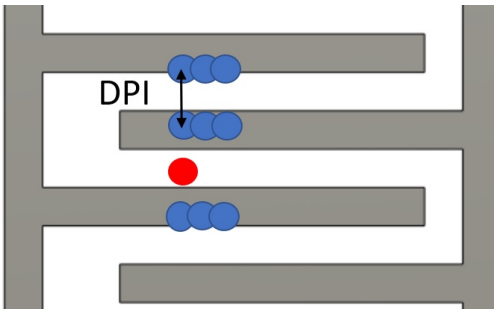

(b)

Figure 4.4: **(a)** Change of drop formation during printing likely due to instability of the ink mixture and **(b)** Schematic representation of the conversion from the design to the placement of the droplet, with the blue drops representing actual print lines and the red dot a skipped print line due to the DPI setting.

4.2.1 Printhead temperature

The printhead temperature is another important control parameter during inkjet printing. The printhead was tuned for the ink at a fixed temperature, a higher or lower temperature resulted in a differ-

ence in viscosity and therefore influenced the drop formation. For stability purposes it was shown to be beneficial to raise the temperature of the printhead, 29°C was chosen for the remainder of the prints. Although the higher temperature did lower the viscosity of the ink, having it at a higher temperature improved the temperature stability of the printhead and resulted in a more consistent print. The printhead temperature at 25°C was affected when the printer was exposed to sunlight, resulting in the formation of satellite droplets during printing.

4.2.2 Print alignment

When printing a new design on an already existing pattern, some additional print alignment steps, as discussed in the following section had to be performed. By default, the printer should place the print design with respect to the lower-left corner of the design in the print recipe. However in reality this was not the case. The difference is illustrated in Figure 4.3. It shows the difference between the starting position marked by the intersection of the red axis system and the actual print position, thus showing an offset of approximately 200 μm on the X-axis and 300 μm on the Y-axis. The difference in offset varied based on the design, its dimensions and likely the flight of ink droplet. To print a pattern in the exact location a test print had to be performed to determine the offset from the printing starting point and the actual starting point of the print. The sample had to be visually aligned with the Y-axis of the printer to within 1 degree. This is the maximum possible rotation of the stage. By jogging and rotating the stage, the electrode can be coincident with the axis of the printer. Once the axis is aligned and compensated for the offset, only then will the printer print in the exact location.

4.3 Ink substrate interaction

The ink-substrate interaction plays an important role in the printing process, it influences the resolution of the printing process and the drop behaviour on the substrate. The interaction of the surface tension of the liquid and surface free energy of the substrate dictates how the droplets interact on the substrate surface. By decreasing the spacing between droplets, i.e. by changing the DPI, an overlap between droplets is achieved and thin lines can be formed depending on the interfacial energy between the ink solution and the substrate surface. Figure 4.5a shows the formation of print lines when sufficient drop overlap and surface wetting is present. However, due to the surface tension of the liquid on silicon substrates with low surface energy, droplets coalesce into separated droplets over time, a phenomenon called dewetting [32]. The time frame for dewetting depends on the surface energy of the substrate, the surface tension and viscosity of the liquid. Dewetting is shown in Figure 4.5b with printing lines on pristine silicon. The left line was printed without overlap between the droplets (400DPI). The second and third lines from the left were printed with approximately 50% overlap between the droplets (800DPI). The print properties of these lines were the same. The only difference between the second and third lines was the time between the prints.

To influence the wetting behaviour of the substrate several surface treatments as discussed in Section 3.1.8 were applied. The influence of the different surface treatments on the wetting behaviour is discussed in the following section.

4.3.1 Contact angle measurement

To demonstrate the influence of different surface treatment methods on the wetting behaviour of the water:glycerol ink, contact angle measurements were performed. They showed that the hydrophilicity was greatly increased after oxygen plasma and slowly got more hydrophobic over time after exposure to air. The contact angle is measured for the water:glycerol ink on the silicon substrate with different surface treatment, the results are illustrated in Figure 4.6. A contact angle of approximately 55° was found on the pristine silicon substrate and complete wetting with a contact angle of less than 4° on the oxygen plasma treated sample. The contact angle measurement for the air-exposed sample was done after verifying perfect film formation during inkjet printing and indicated that a contact angle of approximately $22-24°$ is required for perfect wetting of the substrate. Contact angle

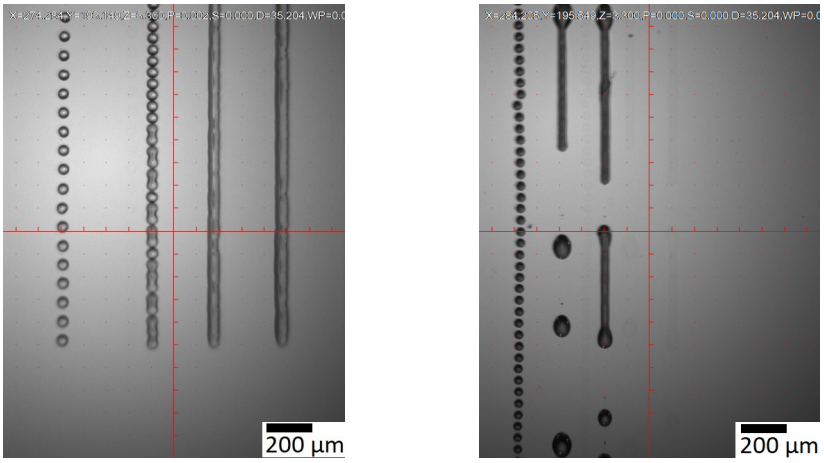

(a) **(b)**

Figure 4.5: Optical image of line prints made by the PIXDRO printer using water:glycerol 1:1 (0.4% (wt/vol)) ink with **(a)** From left to right an increase in DPI between the different print 'lines', 1st line from the left printed at 300DPI, 2nd (500DPI), 3th (700DPI) and the last line at 800(DPI) in **(b)** Three print lines on pristine silicon; the first line droplets are spaced to not overlap (400DPI) and the second and third subsequent droplets have 50% overlap (800DPI)

measurements performed on samples exposed to air after using higher power oxygen plasma treatment, 80W instead of 20W, resulted in contact angles of approximately 40°, higher than the perfect wetting at 22 – 24°. To rule out the effect of contamination already present inside the plasma tool chamber, the plasma tool was run for 30 min at full power before the surface treatment of the silicon samples. This extended cleaning cycle did not affect the wetting behaviour differently compared to that observed by earlier cycles.

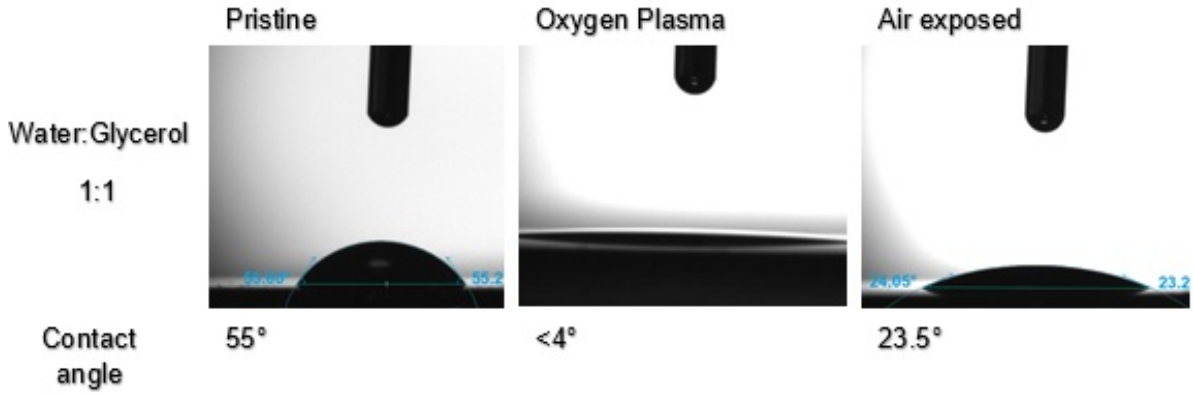

Figure 4.6: Optical image of the contant angle of the ink on different substrates; pristin silicon, oxygen plasma treated silicon (tested within 15 min of the cleaning cycle) and an air exposed sample (tested 2 days after the oxygen plasma treatment).

A higher contact angle will increase the printing resolution. However, the decreased wetting also influenced the liquid film behaviour, as will be demonstrated in the following section with printing on pristine silicon.

4.3.2 Pristine silicon

When printing on pristine silicon with 400 DPI, the surface is covered in individual droplets with no overlap between the separate droplets as demonstrated in Figure 4.7a. The irregularities on the print surface of the Figure 4.7a are due to fluctuations in the printhead during drop formation. A magnification of a single droplet on pristine silicon is shown in Figure 4.9a. Due to the relatively high surface tension versus the interfacial free energy the droplet is completely circular and has a diameter of approximately $47\mu m$. Figure 4.7b illustrates the same ink again printed on a pristine silicon substrate however with a much higher DPI (1000). There is an overlap between individual droplets, which start to merge into larger droplets. The prinstine silicon surface does not have sufficient surface energy for the inkjet liquid to fully wet the substrate. The two other test inks, i.e. ethylene glycol and tri(ethylene glycol) monoethylether both show similar droplet behaviour on the pristine substrate as the water:glycerol solution (see Figure H.1a), i.e. coalescence of small droplets into irregular spaced larger ones.

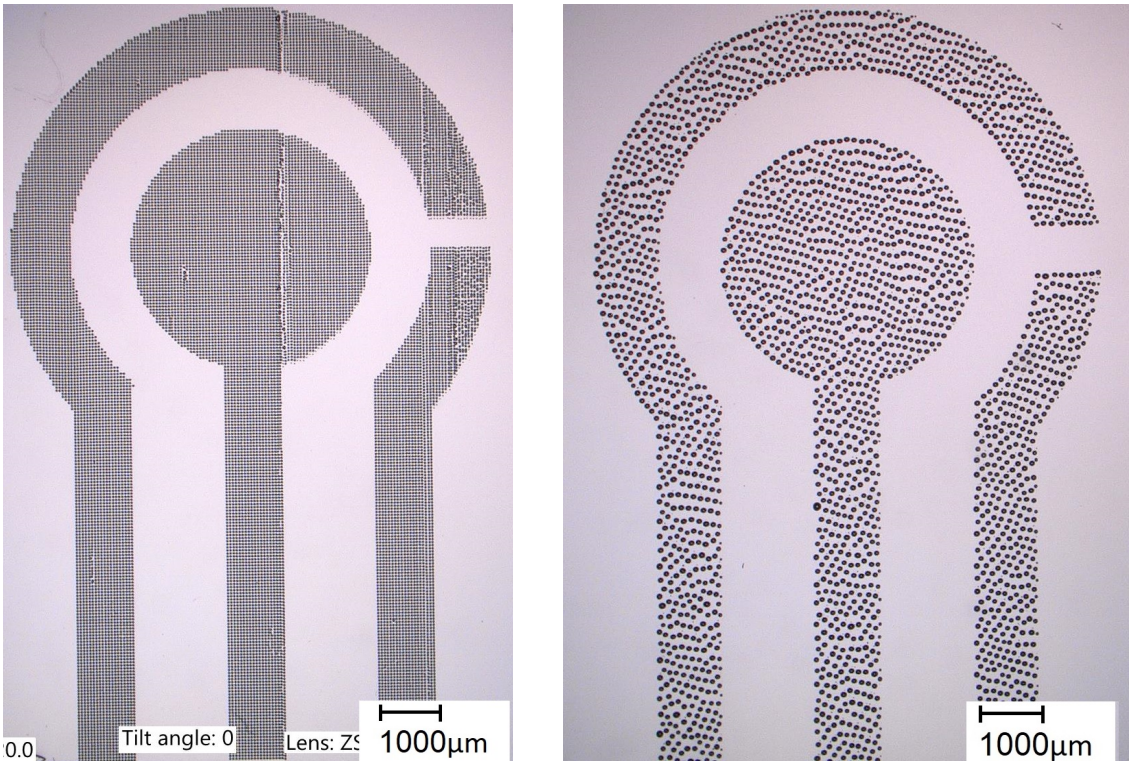

(a) **(b)**

Figure 4.7: Optical image showing of **(a)** printing on pristine silicon, at 400 DPI such that there is no overlap between the different droplets and **(b)** Printing with a DPI twice as high, where droplets start to merge into larger droplets, creating a more uneven print pattern.

4.3.3 Oxygen plasma treated silicon

To increase the hydrophilicity of the substrate surface, an oxygen plasma treatment was performed with different treatment times and power. After printing on this substrate, the substrate surface showed complete wetting independent of the treatment power or time, the result is shown in Figure 4.8. Complete wetting of printed ink droplets on the substrate reduced the feature resolution of the inkjet printed patterns due to feathering at the droplet edge boundary as is illustrated for a single droplet in Figure 4.9b. Ethylene glycol similar to the water:glycerol mixture, shows complete wetting after oxygen plasma treatment. Interesting is the effect of the oxygen plasma treatment on

Figure 4.8: Optical image of water:glycerol ink printed on oxygen plasma treated silicon, using a droplet density of 300 DPI.

the wetting of tri(ethylene glycol) monoethylether, which caused an even higher repellent effect on the liquid as shown in Figure H.1b.

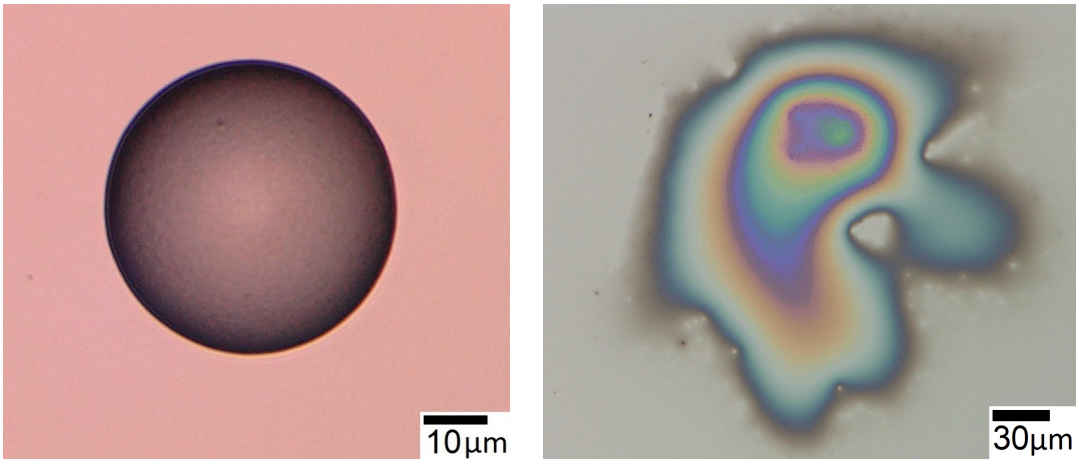

(a) **(b)**

Figure 4.9: Optical images of **(a)** print of a single droplet of water glycerol on pristine silicon and **(b)** a single droplet on the silicon substrate after an oxygen plasma treatment.

4.3.4 Acid cleaned silicon

The next method attempted to change the hydrophilicity of the surface was an acid cleaning treatment, based on the procedure described in Section 3.1.5. This increased the wetting of the substrate surface (Figure 4.10a), although not enough to create a continuous liquid film as shown in Figure 4.10b for the case of printing on an air exposed silicon substrate after oxygen plasma treat-

ment.

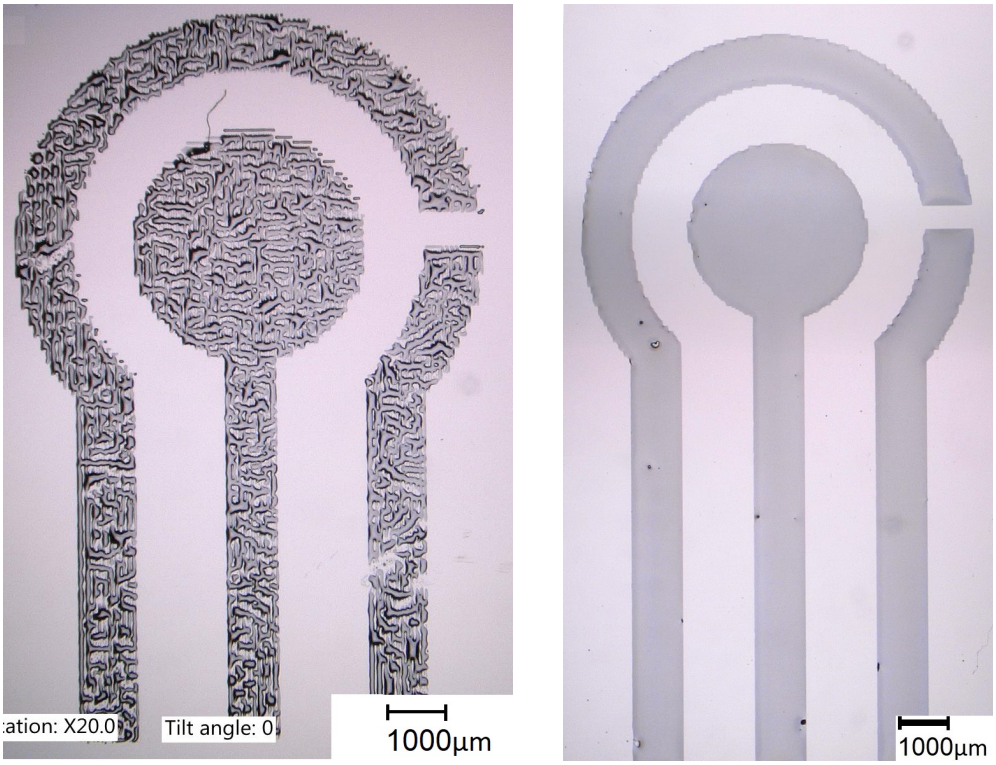

(a) **(b)**

Figure 4.10: Optical microscopy image of **(a)** 1:1 water:glycerol ink print on a acid cleaned silicon substrate at 500 DPI and **(b)** printing on a substrate which was exposed to air for several days after oxygen plasma and printed at 800DPI.

4.3.5 Air-exposure after oxygen plasma

The final method of substrate treatment was based on letting the substrate being exposed to air after oxygen plasma treatment. The air exposure affected the surface energy of the substrate and after some time, the droplets did not fully wet the surface as they did right after the oxygen plasma treatment. Instead, they formed a single liquid region with clear boundaries as shown in Figure 4.10b. The process was stable for some time (over 120 hours), however, the surface slowly turned more hydrophobic after which the droplets again merged in a random and irregular pattern, with bad wetting similar to the pristine substrates. The method of printing with at least 5 hours of air exposure after oxygen plasma treatment is very promising and allows for the printing of uniform films with sharp features.

The duration and power of the plasma treatment had an effect on the hydrophobic recovery. A plasma treated surface for 3 min and 80W returned from full wetting to the pristine stage much faster than a cycle at lower power and shorter time. For plasma treatment times of 2 min at 20W, the surface remained printable approximately between 5 and 120 hours. The process was repeated several times with inks with 1:1 ratio of water and glycerol containing 0.4 and 0.2% (wt/vol) diamond NPs. It appears that a specific range of contact angle the ink made with the silicon substrate led to perfect wetting of the surface, demonstrated in Section 4.3.1. It is expected that the perfect wetting of the substrate was due to an equilibrium between the surface free energy of the substrate and the surface tension of the liquid. It is unclear why the lower power oxygen plasma gave the desired result for a longer time period. It appears counter-intuitive that the higher power oxygen plasma returns to

a hydrophobic state more quickly in time. However, high power oxygen plasma has been demonstrated to affect the surface roughness of silicon substrates and potentially influence the wetting of the surface [84]. Since both cleaning cycles were relatively short and at low power, it is unlikely that the surface roughness was affected during the applied cycles.

Finally, to quantified the surface energy of the substrate after the different treatments, the contact angle measurements were also used to determine the surface free energy (SFE) of the substrate. The surface free energy was determined for the oxygen plasma treated surface, pristine silicon and an air-exposed surface after oxygen plasma treatment. By measuring the contact angle using three different liquids, MillQ Di water, ethylene glycol and a non-polar liquid diodomethane 99%. The SFE energy for the pristine and air-exposed silicon substrate was determined at 42.4 mN/m and 61.6 mN/m respectively by the build-in software. The SFE of the plasma treated surface could not be determined because the angle of contact was less than 4° for both Di water and ethylene glycol. The results of surface free energy for the different surfaces can be found in Figure 4.11.

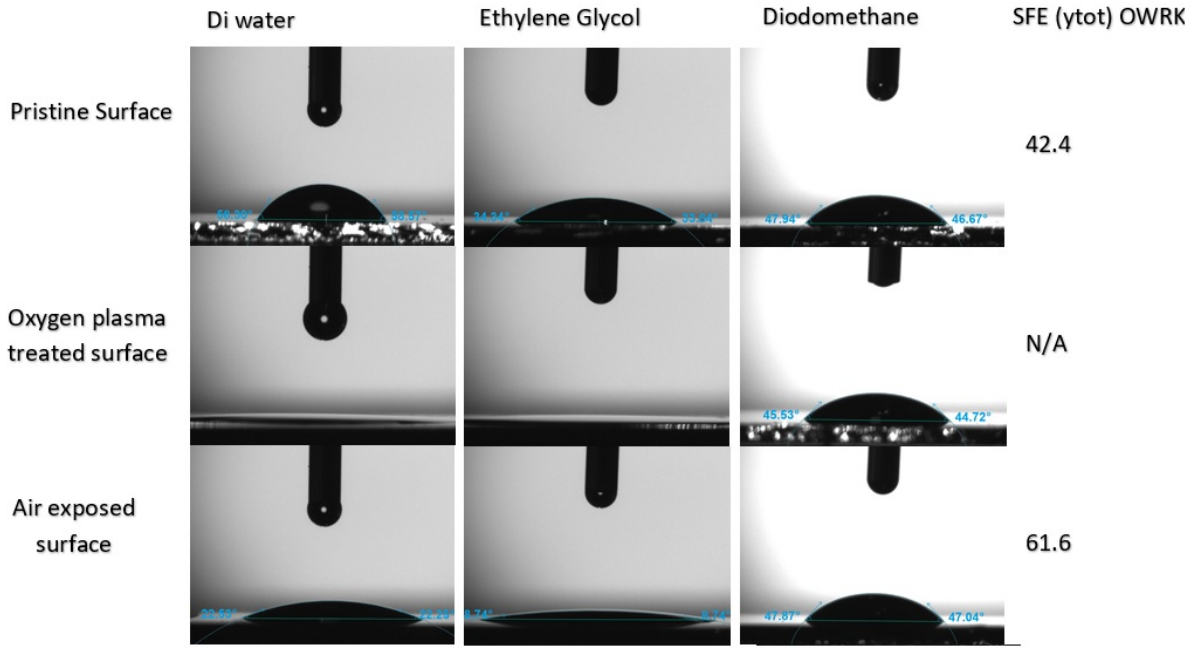

Figure 4.11: Contact angle and surface free energy of the different substrates using the three test liquids: Di water, ethylene glycol and diodomethane.

4.4 Seeding density and distribution

All printing was done in a single run, i.e. the printing process did not consist of multiple passes on the same area. The seeding distribution and density are a function of the surface treatment, the drying step, particle content in the inkjet ink and the drops per inch (DPI). The results in this section show how each of these parameters affected the diamond NP seeding. The surface treatment affected the wetting of the liquid on the substrate surface, therefore with increased wetting the same liquid volume covered a larger area, resulting in a lower seeding density, which can be observed in Figure 4.12b. Figure 4.12a shows the remaining NPs on pristine silicon after the ink was evaporated using a hotplate and the area after evaporation of a droplet with the same volume on an oxygen plasma treated surface (Figure 4.12b).

4.4.1 Particle size

Figures 4.12a and 4.12b do however show agglomerations of NPs on the substrate. To investigate how many of these were already present in the solution measurements were performed on a Zetasizer Nano ZS available at the Faculty of Applied Science, TU Delft, this way the agglomeration behaviour of the nanoparticles in the inkjet ink can be monitored. The results can be found in appendix J however, the results were only partially conclusive. The highest degree of NP dispersion was found for the stock NanoAmando solution, and relatively strongest agglomeration was seen for pure DI water. A high-intensity peak in the 100 nm range was present in all tests. Even though the intensity measured for a single 100-nm is equal to that of 1e6 particles in the 10 nm range [85], when compensated to particle size, a minor fraction of diamond particles smaller than 100 nm appeared to be present even in the stock solution. The stock solution should contain particles in the range of $4.4 \pm 0.7\ nm$ according to the manufacturer.
The drying of the ink droplets after printing also had an effect on the distribution of particles as will be discussed in Section 4.4.2.

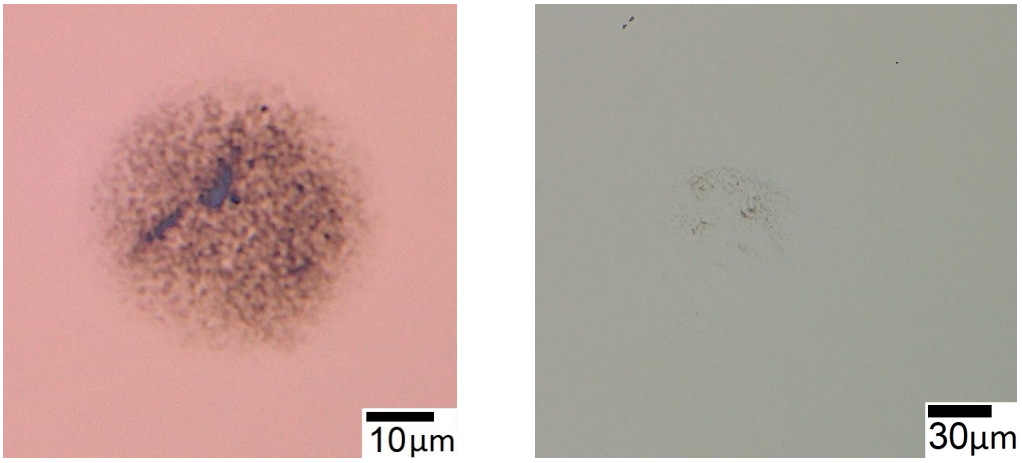

(a) **(b)**

Figure 4.12: Optical microscopy image of **(a)** remaining diamond NPs after drying of a droplet on a pristine silicon substrate and **(b)** a droplet of equal volume and 0.4 %(wt/vol) diamond NPs printed on an oxygen plasma treated substrate, for which case the seeding is barely visible.

4.4.2 Heating ramp during drying

Before diamond growth in the HFCVD reactor, the print samples had to be dried to avoid contamination in the reactor. The samples were therefore placed on a hotplate at a temperature of 200-250 $°C$, to evaporate the liquid. Experiments showed that the rate of heating affected the flow in the droplet and the distribution of the particles. Due to the small size of the nanoparticles, this effect is more easily visualized after CVD diamond growth. A common observation during inkjet printing is the so-called coffee-stain effect as discussed in Section 2.4.2. This effect was not observed with the water:glycerol ink used during this project, high resolution SEM micrographs (Figure F.3) shows that the seeding density is higher towards the center of the droplet pattern. However, the magnified section of Figure 4.13, demonstrates the effect of ramping the temperature too fast, 0-200 $°C$ in 1-2 min, which leads to a large number of particles being present in the centre of the evaporated droplet. When increasing the temperature at a much slower rate (10-20 $°C$ / min) during the drying process, this effect was not observed and the CVD diamond print spot appeared homogeneous (Figure 4.15a).

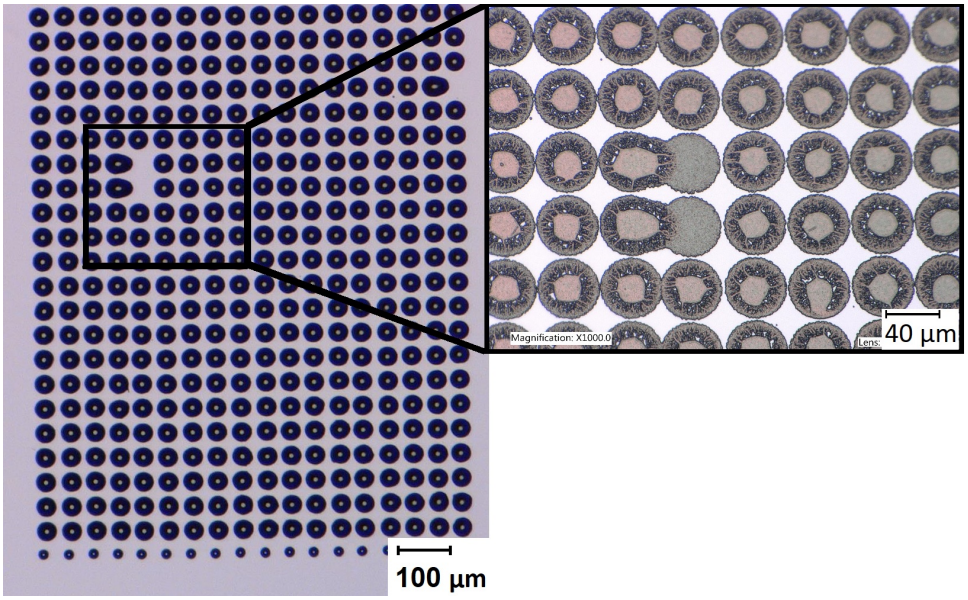

Figure 4.13: Optical microscopy image of the left image showing the inkjet printed pattern with liquid droplets and the right image is a section of this pattern after CVD diamond growth, showing diamond nucleation in the section without liquid droplet. Note the non-homogeneous diamond growth, with high nucleation in the center and boundary of the individual droplet print spots.

4.4.3 Seeding density

From print seeding the substrate with ink, containing different %(wt/vol) diamond NPs, different drop volumes and different surface treatment methods, it was demonstrated that depending on the method used, a different seeding density of the substrate was achieved. By using high resolution SEM the seeding density and particle agglomeration could be assessed. The following SEM micrographs in Figure 4.14 were taken from the substrates after seeding using different methods. The four methods are spin-coating (Figures 4.14a and 4.14b), inkjet printing with a high DPI on the pristine silicon substrate (Figures 4.14c and 4.14d), inkjet printing directly after oxygen plasma (Figures 4.14e and 4.14f) and printing on the air-exposed substrate(Figures 4.14g and 4.14h). During seeding the aim is to cover the substrate covering a high percentage of the area, with as little agglomerations as possible. The results of analysing the seeding density using ImageJ is shown in Table 4.1.
Printing on pristine silicon, with bad wetting of the surface, resulted in large concentrations of diamond NPs on the area covered with the remaining droplets, such a high density that separate agglomerations could not be identified as shown in Figure F.4. The area in between the dried droplets, shown in fig. 4.14c shows much bigger agglomerations relative to the normal spin coating procedure and a similar agglomeration density. The larger agglomerations are likely caused by the addition of glycerol in the as-prepared ink solution. Seeding after oxygen plasma shows large area spreading with small agglomerations, the total area covered according to imageJ is only 25.7% however, from the SEM monograph (Figure 4.14e) this values visually seems to be much higher. The software had difficulty trying to separate image noise from nanoparticles on the surface, the total agglomeration count is therefor in reality likely some what higher.
Seeding on the air exposed substrate showed a more homogeneous distribution of the particles as compare to printing on pristine silicon, still at a much higher surface coverage as compared to the spin coated seeding and printing on oxygen plasma and with bigger agglomerations. The pristine and air exposed samples printed at high DPI (850,750) were difficult to image at high resolution, this is likely caused by contamination of the surface due to the drying on the glycerol. The contrast and magnification were not high enough to accurately determine the mean agglomeration size of these

methods.

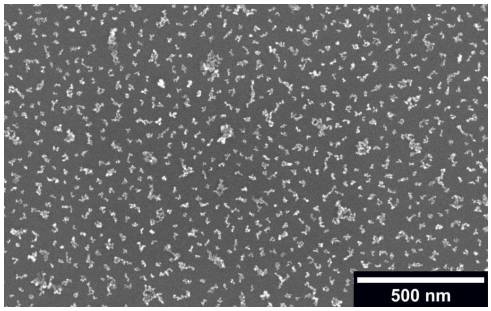

(a) Seeded using Spin coater [16].

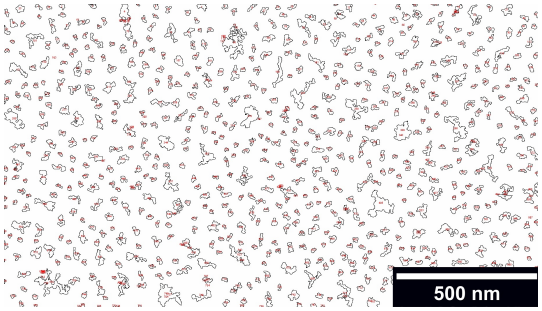

(b) ImageJ particle analysis of the spin coated sample.

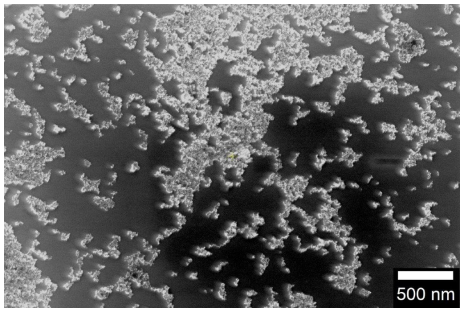

(c) inkjet printed seeding at 850DPI on pristine silicon in between droplet patterns.

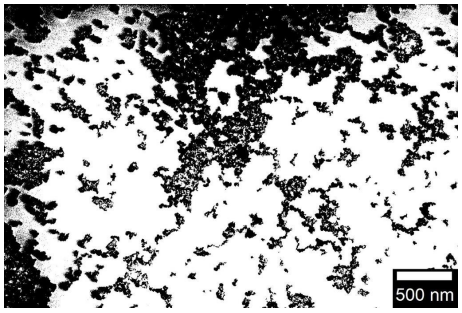

(d) ImageJ particle analysis of printing on a pristine silicon substrate.

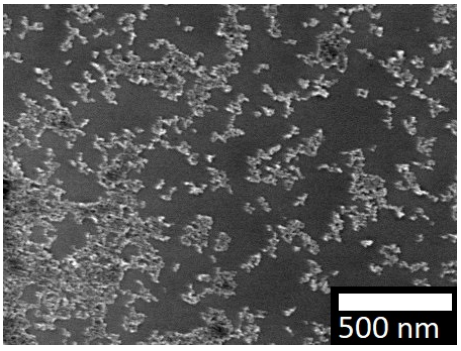

(e) inkjet printed seeding at 350DPI on oxygen plasma treated silicon.

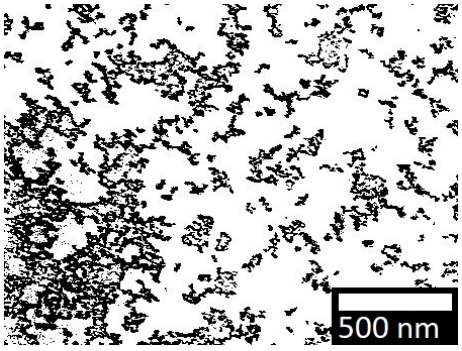

(f) ImageJ particle analysis of printing on oxygen plasma treated silicon.

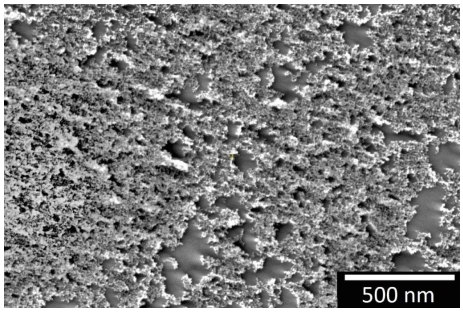

(g) inkjet printed seeding at 750DPI on air exposed substrate.

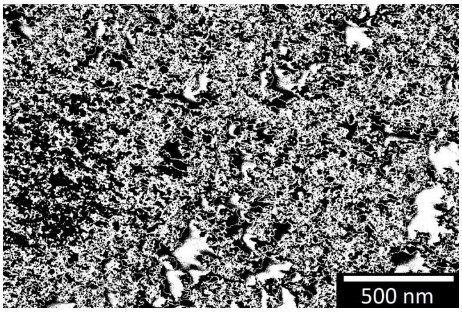

(h) ImageJ particle analysis of printing on air exposed substrate.

Figure 4.14: SEM micrographs (a,c,e,g) of NP-seeded silicon substrate surfaces using different inkjet printing conditions and corresponding ImageJ analysis images (b,d,f,h). (a,b) are a standard spin-seeding procedure similar to [79]. Printed with (0.4% (wt/vol)) water:glycerol ink at (850DPI) on a pristine silicon substrate (c,d), oxygen plasma treated substrate (350DPI) (e,f) and on an air exposed silicon substrate (750DPI) (g,h).

Table 4.1: Area coverage, agglomerate density and average agglomerate size of diamond NPs after spin seeding and after inkjet printing using different substrate treatments. Data were derived from ImageJ software analysis of HR SEM images shown in fig. 4.14

Sample	Area coverage (%)	Agglomerate density ($/cm^2$)	mean agglomerations (nm^2)
Spin coating	13.3	$3.8e^{10}$	351
Print 850DPI (pristine)	31.6	$3.23e^{10}$	2120
Print 350DPI (oxygen plasma)	24	$4.53e^{10}$	329
Print 750DPI (air-exp)	54	-	-

4.5 Diamond nucleation and CVD thin-film growth

The same printed droplets demonstrated as a liquid in Figure 4.9 and after drying in Figure 4.12 are presented in Figure 4.15 after 30 min of diamond growth, showing how the spreading of the oxygen plasma droplet reduced the nucleation density during CVD diamond growth. The following sections demonstrate the effect of the different printing methods and diamond NPs content on the thin-film diamond patterns.

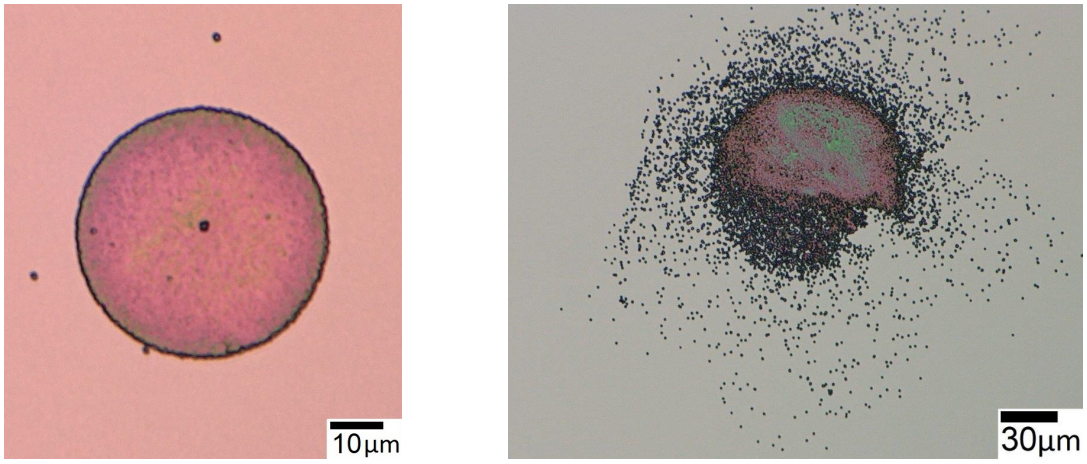

(a) **(b)**

Figure 4.15: Optical microscopy images of **(a)** a single droplet on pristine silicon after 30 min of CVD diamond growth and **(b)** a 30 min CVD diamond droplet of equal volume and 0.4 %(wt/vol) diamond NPs printed on an oxygen plasma treated substrate.

4.5.1 Pristine silicon

From growing diamond samples without changing the surface energy of the substrate, it was shown that bad wetting of the substrates still resulted in seeding of the entire area where the droplet resided as also illustrated in Figure 4.13. This is likely due to a combination of the two effects mentioned in previous sections, namely droplet coalescence and water evaporation. The area where the glycerol does not appear after printing was in fact seeded with diamond NPs. However, with a (wt/vol) of 0.2% diamond NPs, the area in between the droplets showded a low seeding density, not resulting in a closed thin diamond film after 45 min of growth as illustrated in Figure 4.16. The amount of diamond NPs in the ink solution was therefore raised to 0.4% (wt/vol).

With the latter ink solution, a high enough seeding density in between the glycerol droplets was

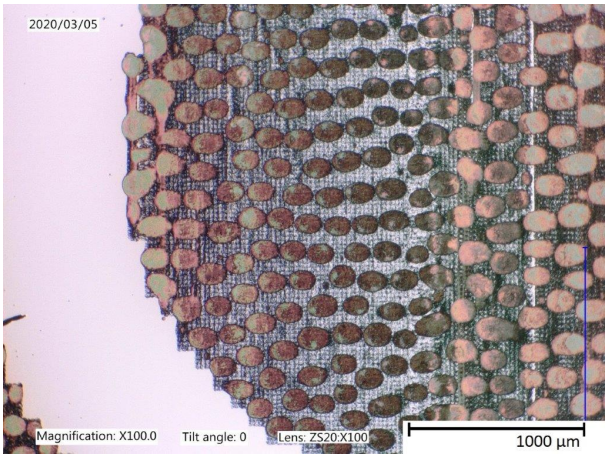

Figure 4.16: Optical microscopy image of a section of a diamond electrode printed with 0.2% (wt/vol) at 800DPI and exposed to 45 min of CVD diamond growth showing low nucleation density in between the pixel areas initially formed by the water:glycerol droplets.

achieved. By printing with different DPI, a certain control over the spreading of the liquid could be achieved and as such the substrate seeding. The effect of changing the DPI on the thin-film diamond growth is illustrated in Figure 4.17. The three samples (a,c,e) are printed with different DPI, resulting in a well-ordered distribution of individual droplets and NP seeds at 500DPI in (a,b). Versus non-uniform distribution of ink liquid, without full surface coverage at 700DPI (c,d) and near-complete thin-film diamond patterns with relatively larger surface coverage at 1000DPI as shown in Figure 4.17 (e,f).

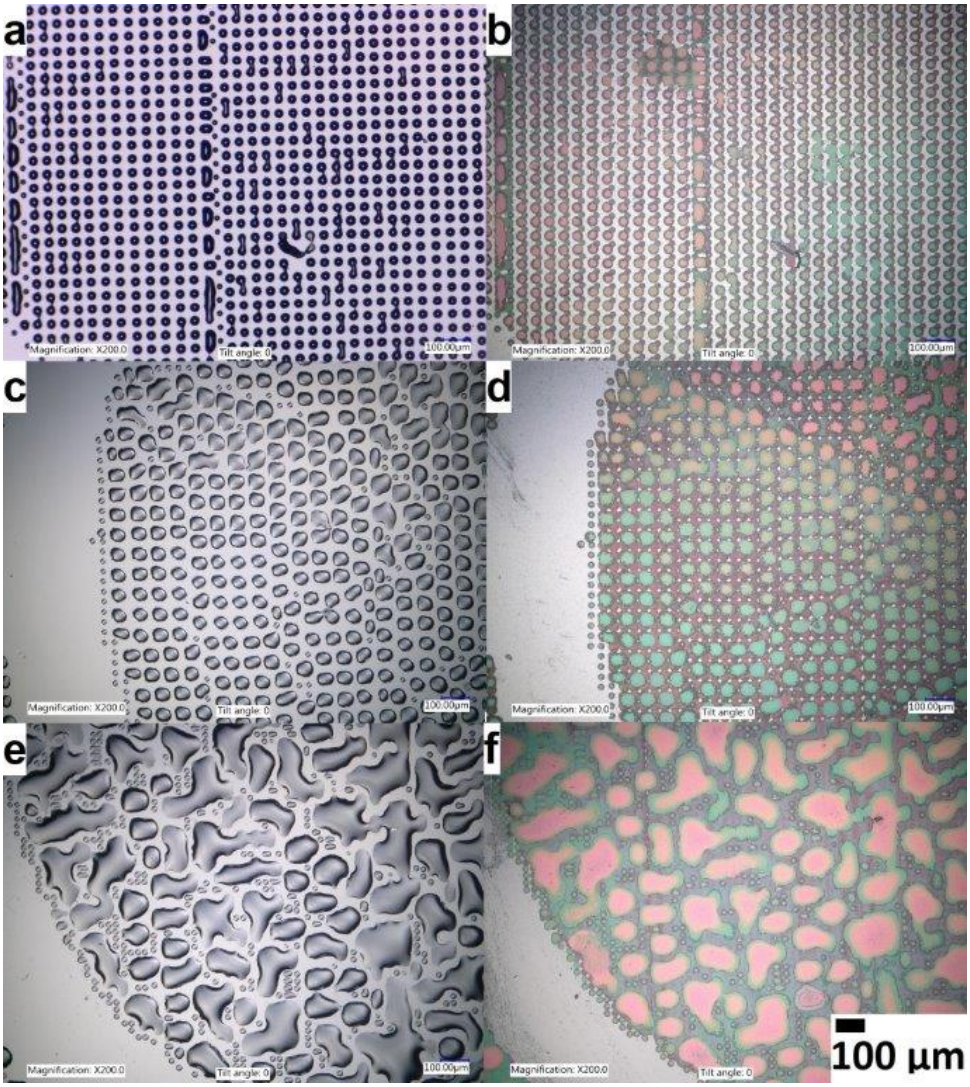

Figure 4.17: Optical microscopy images of diamond-grown print patterns showing the effect of different DPI on the wetting on the substrate surface. Images (a,c,e) show the liquid samples directly after inkjet printing and images (b,d,f) show the final CVD diamond patterns. The DPI for the different prints was 500DPI (a,b), 700DPI (c,d) and 1000DPI (e,f).

Although this method of printing with 0.4 % (wt/vol) at 1000DPI led to a diamond layer covering nearly the entire surface, contrast pictures taken using SEM still demonstrated small gaps in the diamond thin film. In part due to contamination present on the substrate surface. The colour differences present in the optical image illustrated in Figure 4.18a indicate regions of higher and lower concentrations of diamond NPs. The SEM image in Figure 4.18b is a magnified image of the area marked in red on the optical image. On the SEM picture, no boundary between high and low-density seeding region is visible, and a continuous diamond thin film appears. The white-light interferometry image in Figure G.1 shows the pattern (Figure 4.17 f) obtained using 1000 DPI formed a nearly continuous thin diamond layer (thickness 800 nm) with locally approximately 100 nm thicker regions of light blue color contrast. It is unknown how these regions of higher concentrations of intrinsic diamond NPs will affect the performance of the electrode once grown in BDD. With the correct % (wt/vol) and DPI, it is possible to selectively seed the substrate for CVD (boron-doped) diamond growth with this method and create relatively sharp features.

Diamond growth of the patterns printed with the tri(ethylene glycol) monoethylether ink was unsuccessful, showing nearly any nucleation at all, most likely because the diamond NPs rapidly precipitate from the as-prepared ink solution as demonstrated in Figure 4.1, resulting in a print with a low concentration of seeds.

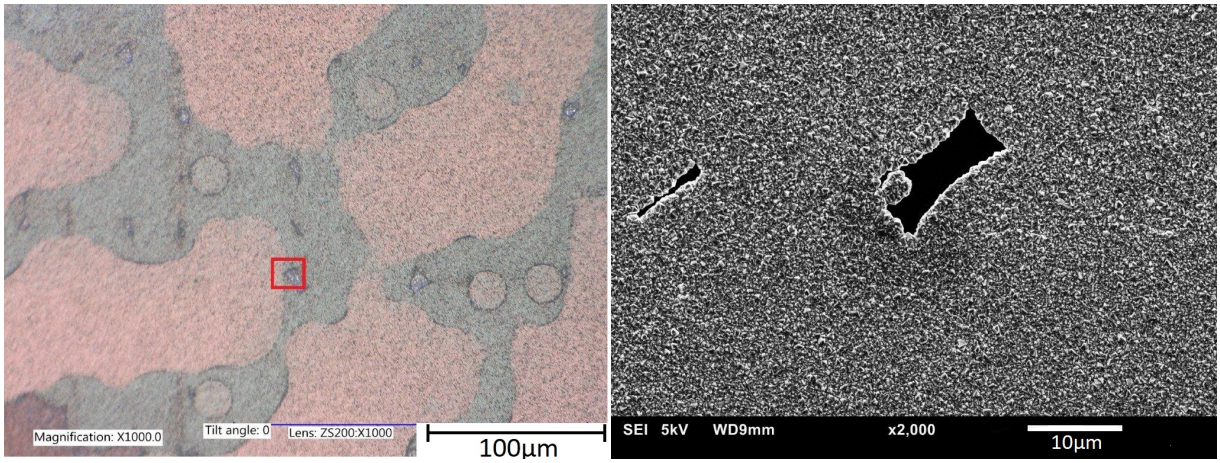

(a) **(b)**

Figure 4.18: **(a)** Optical microscopy image of the surface after diamond growth. The area marked in red is magnified in **(b)** using SEM and shows the NCD surface. Note that the boundaries present in the optical image do not appear in the SEM micrograph.

4.5.2 Oxygen plasma treated silicon

The initial ink solution when printing on an oxygen plasma treated surface contained water:glycerol in a ratio 2:3. This resulted in a boundary region of about 50 μm with lower nucleation density as indicated in Figure 4.19. The boundary region around the print is most likely due to evaporation of the ink after printing, as a result of the high water content in the ink. Although the features are sharp and this process resulted in a continuous diamond thin film, the minimum feature resolution achievable using the inkjet print process is compromised.

To reduce edge evaporation and based on Z number calculations on the effect of increased viscosity, the amount of glycerol was increased to a 1:1 ratio with 0.4% (wt/vol) diamond NPs. This mixture did reduce the edge evaporation, however the effect was replaced by feathering around the edges of the sample as illustrated in Figure 4.20.

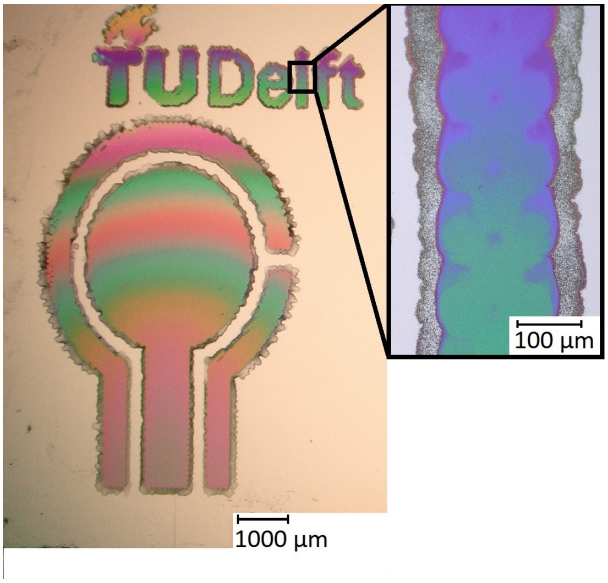

Figure 4.19: Optical microscopy image of a full-diamond three-electrode pattern produced by inkjet printing using 3:2 water:glycerol ink at 400DPI after an oxygen plasma treatment, followed by 30 min of CVD diamond growth. Note: the ink printing step proceeded with complete surface wetting

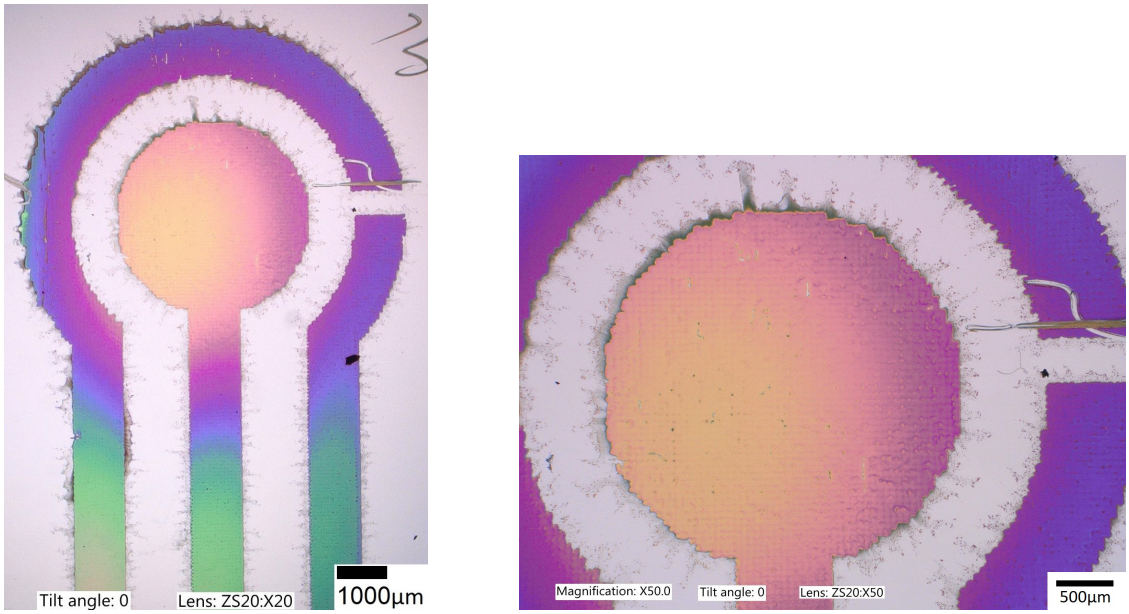

(a) **(b)**

Figure 4.20: optical microscopy image of **(a)** diamond thin-film electrode pattern, printed using water:glycerol 1:1 with 0.4% (wt/vol) at 350DPI and **(b)** showing the same print at a higher magnification, illustrating the feathering around the edges.

4.5.3 Air-exposure after oxygen plasma

The best results for patterning using the inkjet printing process was by letting the substrate surface exposed to air after oxygen plasma for a period of minimal 5 hours, which in the liquid phase already showed complete wetting with sharp features. The same sharp features could be observed after diamond growth which resulted in a continuous diamond thin film. Printing with this technique allowed for printing of nearly 90° angles (see Figure 4.21a). Using SEM (Figure 4.21b), no obvious

defects in the diamond surface were observed. Furthermore using SEM imaging at higher magnification showed the surface morphology of the diamond film consisted of NCD after a growth time of 45mins (Figure F.2).

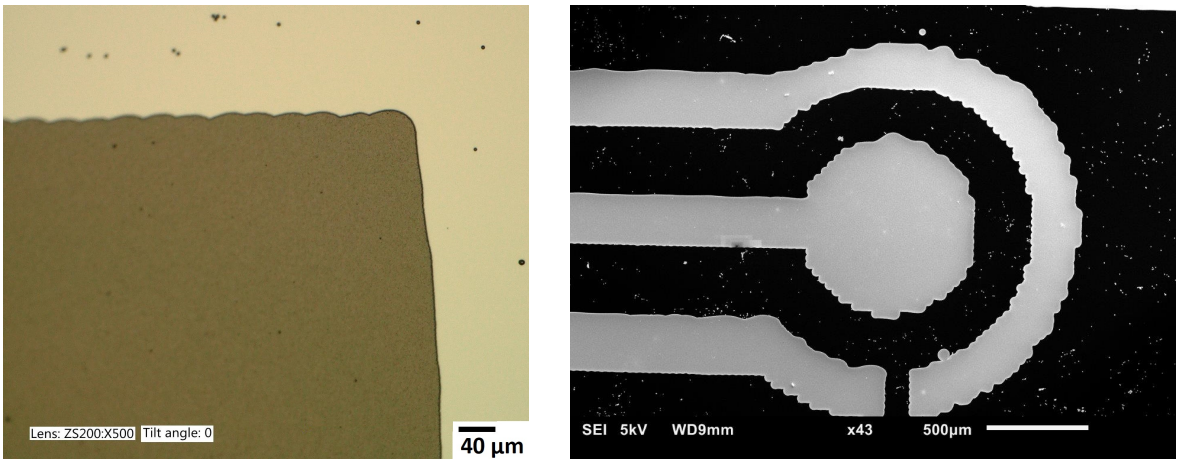

(a) **(b)**

Figure 4.21: **(a)** Optical image of a corner of a thin-film diamond square, grown for one hour after seeded using inkjet printing on an air-exposed oxygen plasma treated silicon substrate and **(b)** SEM micrograph of a diamond electrode printed at 750DPI using water:glycerol 1:1 with 0.4% (wt/vol) on a air exposed silicon substrate.

An attempt to print small features using the DMC-11601 printhead with the optimzed surface treatment and the regular quantity 0.2% (wt/vol) of diamond NPs used for spin coating (as recommended by NanoCarbon research institute Ltd) resulted in a nucleation density too low for thin film growth. The resulting electrode grown from such low nucleation density is illustrated in Figure 4.22.

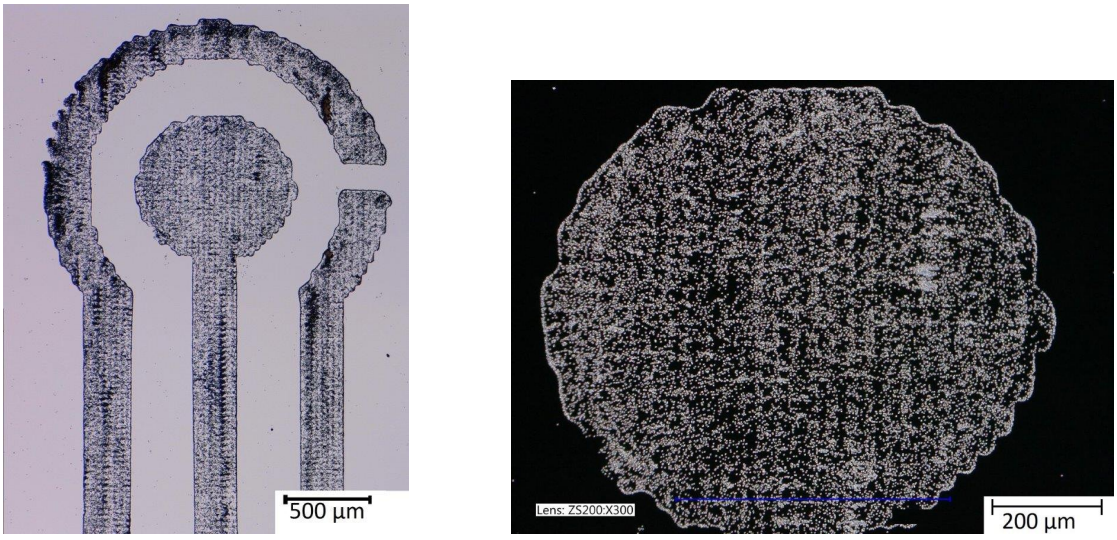

(a) **(b)**

Figure 4.22: Electrode using 1 pL cartridge at 1000DPI with 0.2 % (wt/vol), grown for 1 hour showing **(a)** the electrode surface and **(b)** a zoomed in section of the WE electrode with increased contrast.

4.6 Printing resolution and additional geometries

It is difficult to put a decisive number on the minimum feature size, i.e. the minimum width at which a thin-film diamond pattern can ultimately be produced. The feature size is depends on the geometry of the design, the DPI and the drop size. By employing air-exposure after oxygen plasma and printing with the DMC-11610 cartridge, straight continuous lines of around 60 μm width could be produced. Figure 4.23 shows the effect of reducing the size of the print pattern on the feature size. By decreasing the object size, more line bulging was present. This effect was even larger with a curved pattern due to the way the pattern was printed, namely in the Y-normal uni-directional mode as discussed in section 3.1.2. The line bulging was reduced by changing the DPI and optimizing the image used as input in the PIXDRO HMI, with feature sizes related to the drop diameter. Figure 4.23 Illustrates the reduction of the print patterns down to the minimal feature size. With line width of a single droplet, line bulging started to become more dominant and the spacing of the interdigitated electrode arms was also not consistent.

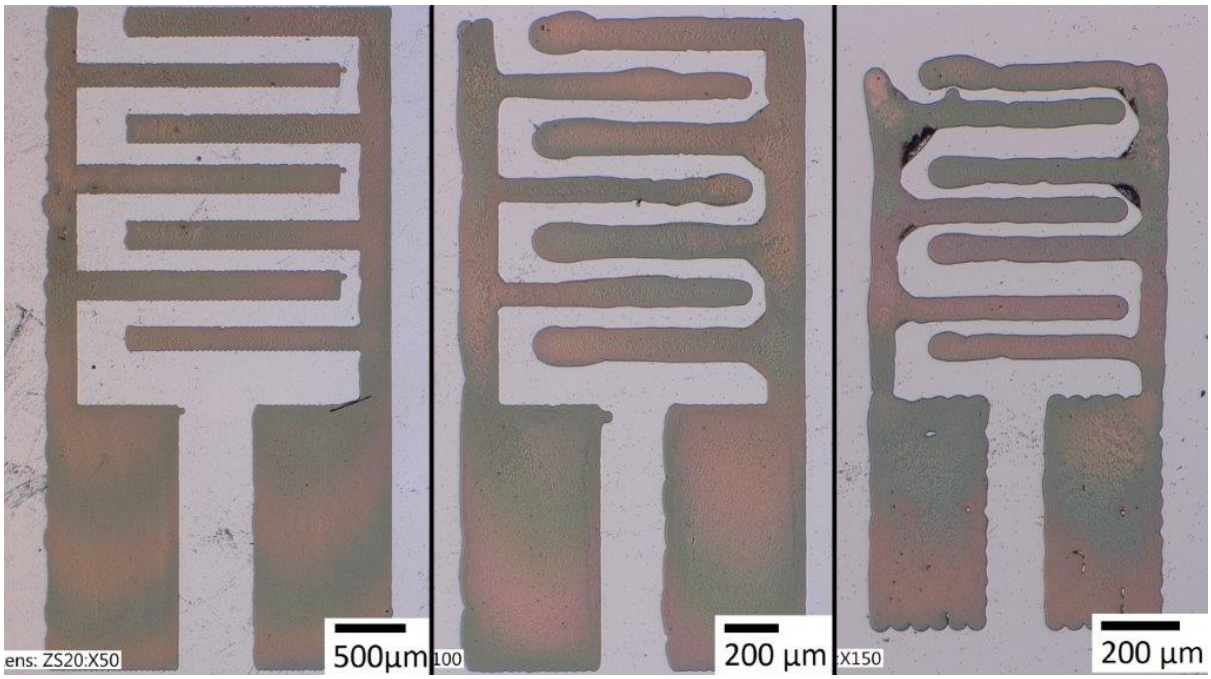

Figure 4.23: Optical microscopy image of interdigitated electrodes reduced in size by 50% from left to right. The right electrode has the smallest possible feature size of approximatly 60 μm with the current contact angle of 24° and a single line of droplets being printed.

4.6.1 Additional geometries

As discussed earlier, inkjet printing being a digital process allows for prototyping with customizable geometries in a bottom-up fabrication approach. Showing this technique is not only applicable for printing electrochemical sensors, several different designs were patterned using the diamond ink. SEM images of these patterns are shown in Figure F.1.

The final results showed that the PIXDRO printer is capable of seeding the substrate with electrode patterns using different approaches. Depending on which printhead and which surface technique is used the amount of added diamond NPs should be changed accordingly to create sufficient nucleation sites.

4.6.2 BDD

With the ongoing construction of the new PME HFCVD reactor capable of producing BDD. 2 $inch$ wafers were prepared for BDD growth by plasma-assisted CVD with the help of Prof. dr. Ken Haenen (UHasselt). Figure H.2 shows one of the wafers prepared for growth in Hasselt. Unfortunately, disaster struck twice, their reactor became inoperable and COVID-19 hampered the repair process significantly. Thus, no BDD electrodes could be manufactured during the course of this MSc thesis.

4.6.3 Black diamond

In the absence of a working BDD reactor, an alternative approach of growing conductive so-called black diamond was initiated. By increasing the amount of methane and nitrogen during CVD growth, the aim was to grow diamond with a higher concentration of sp^2 carbon to enhance conductive properties, as was demonstrated previously [86–88]. All samples were grown for one hour at approximately 425 W filament power on a heated substrate at 725 $^\circ C$ at 10 mbar. Among the growth experiments, the percentages of methane and nitrogen was varied. A total of four growth experiments were performed. Table 4.2 summarizes the growth parameters. When analysed by its Raman spectroscopy (Figure 4.24), specific peaks can be observed around 1140 cm^{-1} associated with trans-polyacetylene, the diamond peak at 1332 cm^{-1}, indicating the presence of sp^3 carbon and a large G band at 1540 cm^{-1} indicating high sp^2 carbon content [89]. The relative intensity of the G band increased for all samples with increased methane, indicating a larger concentration of graphite carbon and the bands associated to trans-polyacetylene decrease with respect to the reference sample and increased methane concentration.

Table 4.2: HFCVD Growth parameters used for the growth of black sp^2-rich diamond.

Sample	Hydrogen (sccm)	Methane (sccm)	Nitrogen (sccm)
3% methane	300	9	0
4% methane	300	12	0
5% methane	300	15	0
3% methane and 1% nitrogen	300	12	3

When using four-point probing to determine sheet resistance of the black diamond films, no conductivity values could be obtained, indicating all samples showed higher resistivity than the default P-doped silicon substrate ($1.6 - 2.4\ \Omega \cdot cm$).

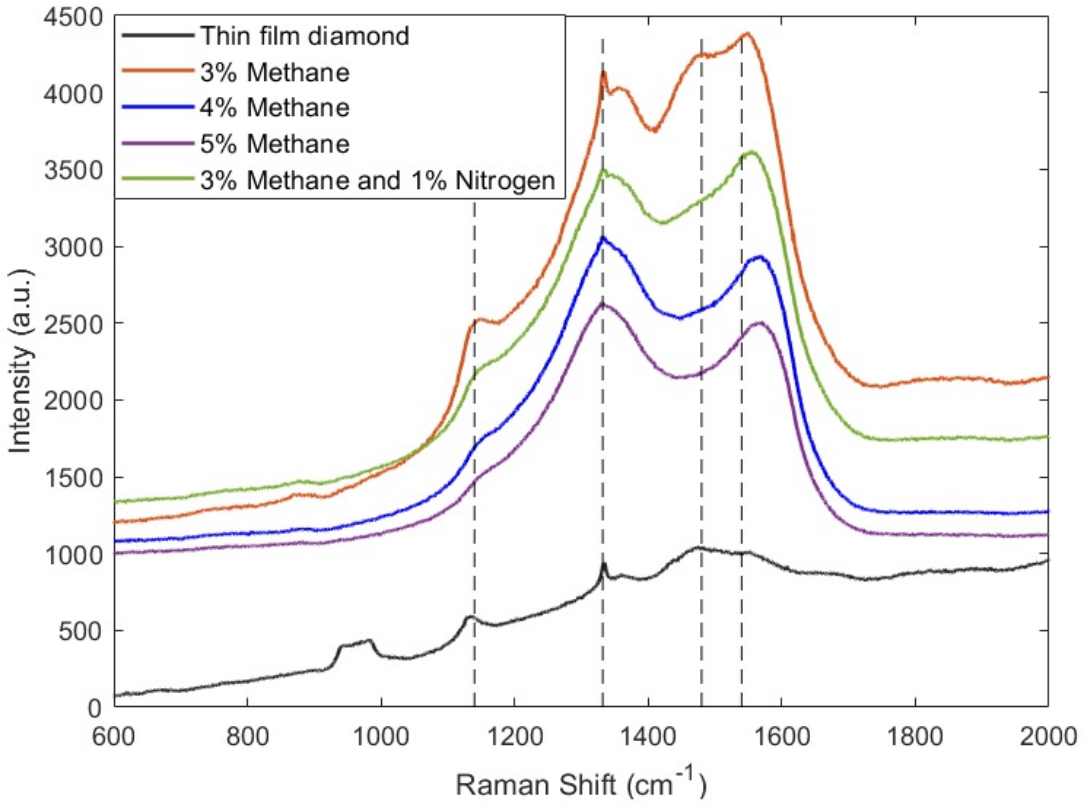

Figure 4.24: Raman spectra on the different diamond thin-films grown with varying methane (and/or nitrogen) flow during HFCVD growth (excitation wavelength 514nm). The dotted lines are placed at 1140 cm^{-1}, 1332cm^{-1}, 1480cm^{-1} and 1540 cm^{-1} respectively.

4.7 EPSON printer

To demonstrate selective seeding without an expensive research-grade printer which might not be available to other research groups, a similar process was performed using a hacked EPSON home-/office printer. The standard inkjet cartridges were replaced with refillable cartridges and filled with the developed 'ink'. The first diamond ink was prepared using DI water and 0.2% (wt/vol) diamond NPs, as previously used by Sartori et al. in the fabrication of diamond micro-disk resonators [16]. These patterns were printed on a diced silicon piece and placed on a glass substrate for which part of the bottom of the printer was removed. The bottom part of the printer was removed to level a glass slide with what would normally be paper height. Printing with a water-based solution resulted in large amounts of satellite droplets. The almost immediate evaporation of the small droplets (3-12 pL) made it hard to assess the printed pattern without CVD diamond growth. The result of the water print is illustrated in Figure 4.25. The print pattern was subjected to a growth process of 20 min, creating a layer thickness of less than 0.5 μm. The inkjet pattern was printed several times with large droplets (12 pL) and was manually shifted to compensate for the gap between the nozzles. The colours in the figure are the natural colours which appear under the Keyence optical microscope due to thin-film interference.

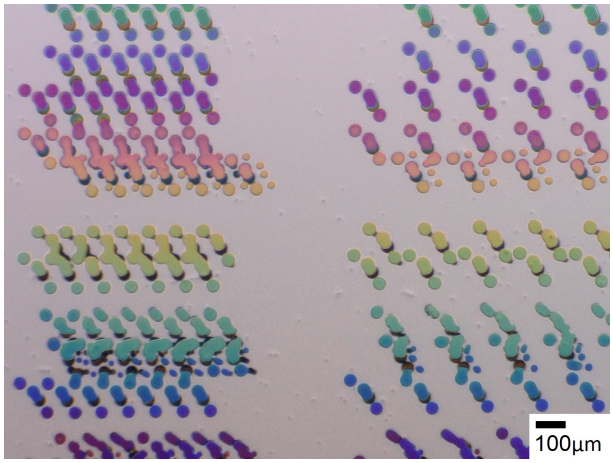

Figure 4.25: Optical microscopy image of CVD diamond spots obtained by printing a silicon substrate using the EPSON printer and water-based ink.

Printing with the ink prepared with added glycerol increased the viscosity of the ink to a value compatible with the ink requirements for the EPSON home/office printer. The results of printing with this mixture on pristine silicon are shown in Figure 4.26a. The 2:3 ratio water:glycerol resulted in equally spaced circular droplets without any satellite droplets but with no overlap between the droplets. Thus, it can be concluded that the wetting of the surface has to be increased to be able to print liquid films instead.

Acid cleaning was the first method used to increase the hydrophilicity of the surface, decrease the contact angle of the liquid and increase the wetting. After acid cleaning, the contact angle the droplets make with the substrates was reduced and the wetting increased. However, six passes with large droplets did not result in enough spreading to cover the entire surface as illustrated in Figure 4.26b. Oxygen plasma treatment using the Diener Femto plasma cleaner for 3 min at 80W resulted in complete wetting of the droplets. After oxygen plasma, by printing with multiple (2-3) passes, thus depositing several droplets on the same location, it was possible to print continuous lines and thin films. However, the frequent failure of a single nozzle had a significant effect on the final result, as demonstrated in Figure 4.27a. After diamond growth, there were two (horizontal) boundaries formed visible with low nucleation density. These gaps visible after diamond growth are much less visible in

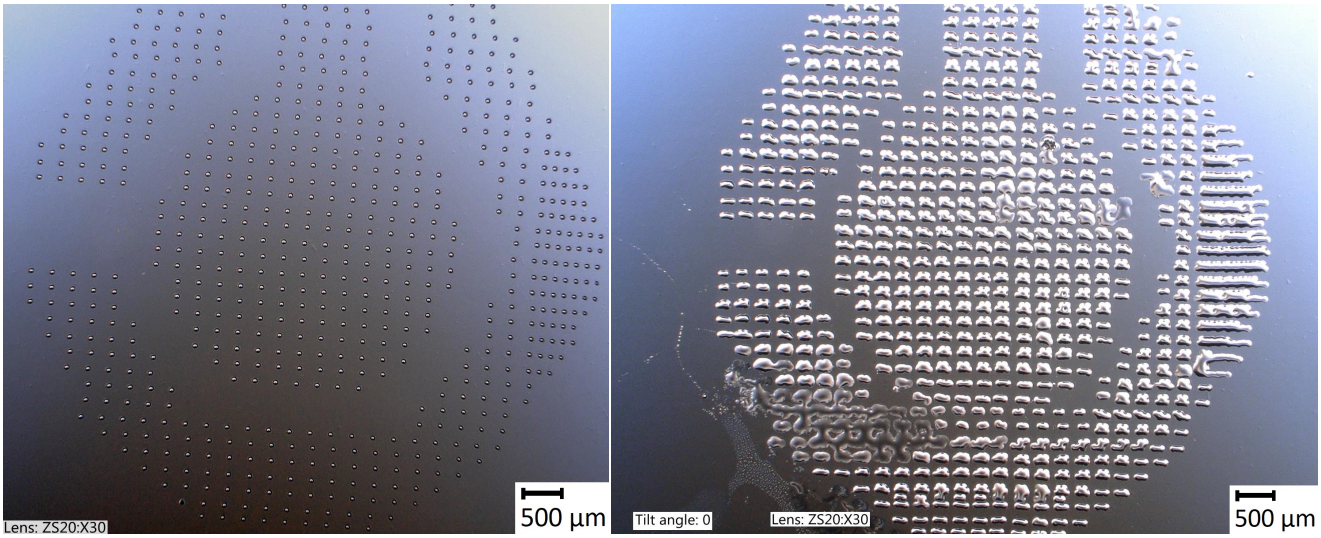

(a) **(b)**

Figure 4.26: **(a)** Epson print result with water:glycerol mixture (wt/vol), a single pass of large droplets and **(b)** 6 passes on a acid cleaned surface.

the preceding liquid ink stage as shown in Figure H.4.

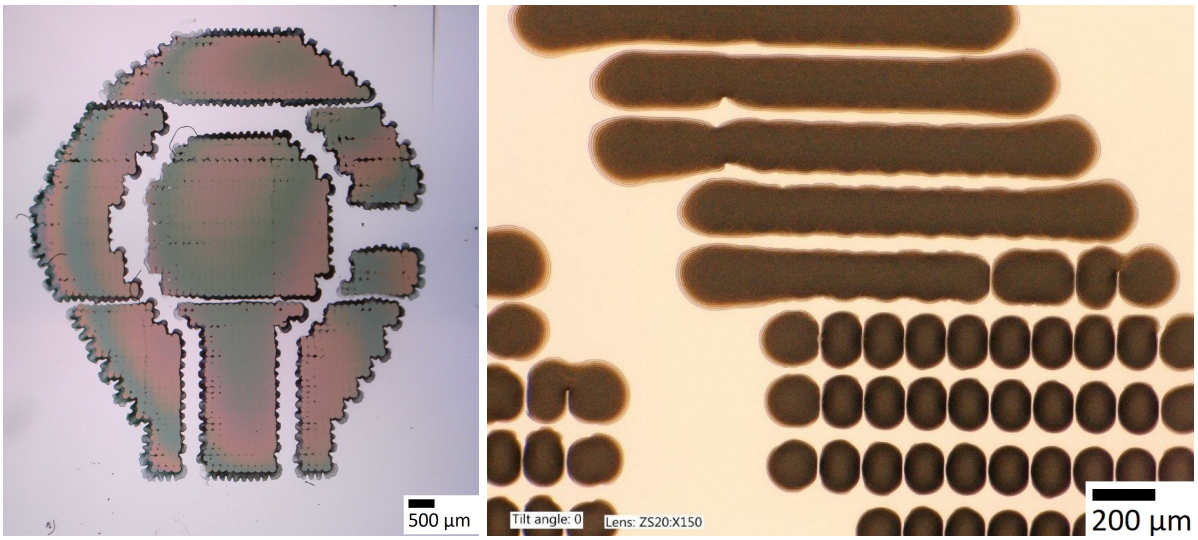

(a) **(b)**

Figure 4.27: Optical microscopy images showing **(a)** Nozzle failure during print and **(b)** a print with commercial silver ink using the Epson printer.

An advantage of the Epson printer is the fact that the ink cartridges can be replaced with refillable ones, to print with different materials at the same time. By replacing the magenta ink cartridge with silver ink, both diamond ink and silver ink are printed at the same time. However, the silver ink has a higher contact angle than the diamond ink and does not show full wetting of the surface, even after oxygen plasma as illustrated in Figure 4.27b. It was therefore impossible to cover the entire surface using the silver ink without any hardware modifications or additional surface modifications.

A motion stage was designed and fabricated based on two mini linear stepper motors. The motion stage was made to fit on the bottom of the inside of the printer, the final result is illustrated in

Figure H.5. The linear stepper motors are controlled using drv8833 stepper drivers and an Arduino microcontroller. By implementing a serial communication in the ECSP-tweak software the steppers can be controlled through the ECSP GUI. However, due to the availability of the PIXDRO printer and the extensive hard coding required for each design with the use of the motion stage, this approach was not continued.

4.8 Characterization of commercial screen-printed electrode (DropSens)

The composition and overall layout of the screen-printed BDD electrode chip from DropSens was characterized using optical microscopy, SEM, Raman and electrochemical characterization. After the dicing and polishing steps as described in section 3.3.1, the different layers of the DropSens chip electrode were measured using optical microscopy. This resulted in the following layer thicknesses as indicated in Table 4.3. An optical microscopy image of the layers is shown in the appendix Figure H.3. The dielectric layer of the electrode helps define the region where the electrochemical process takes place and also prevents any current to flow between the leads of the electrode instead of between the electrodes surfaces.

Table 4.3: Layer thickness of the different layers of the DropSens chip electrode

Material	**Thickness** (μm)
Silver RE	10-15
Carbon CE	30-35
Boron doped diamond WE	1-2
Dielectric layer	10-20
Al_2O_3 Substrate	500

4.8.1 SEM imaging

Using SEM imaging, the individual layers of the DropSens could not be detected and only the surface morphology of the DropSens electrode was evaluated. The surface appears to be a relatively low quality BDD with renucleation and a ballas morphology as shown in Figure 4.28a. From Figure 4.28b even holes can be detected in the BDD electrode layer.

The composition and production of the electrode chip appear to be based on the specifications depicted in Figure 4.29.

4.8.2 Raman spectroscopy

Raman spectroscopy was performed on the surface of the BDD WE and its Raman spectral data were compared to those of a highly doped BDD reference sample provided by Imec (Belgium); see Figure 4.30. The graph was normalised to the background around 1850 cm^{-1} region, compensated for the signal to noise ratio and vertically shifted. The diamond peak is clearly present in the case of the DropSens electrode and no indication of Fano resonance can be detected, unlike the highly doped Imec reference sample, where the Fano resonance shows as two broad bands located at ca. 500 cm^{-1} and 1200 cm^{-1} [90]. This indicates that the DropSens electrode is not as heavily doped and appears not to have metal-like conductivity. The B-C peak in the 500 cm^{-1} region still indicates the presence of a high boron concentration though. Doping levels in the range just before metallic transition give BDD an advantage when used for electrochemical analysis, i.e. it is conductive enough to act as a sensor, however, it does not suffer from the narrower potential window at higher boron doping levels.

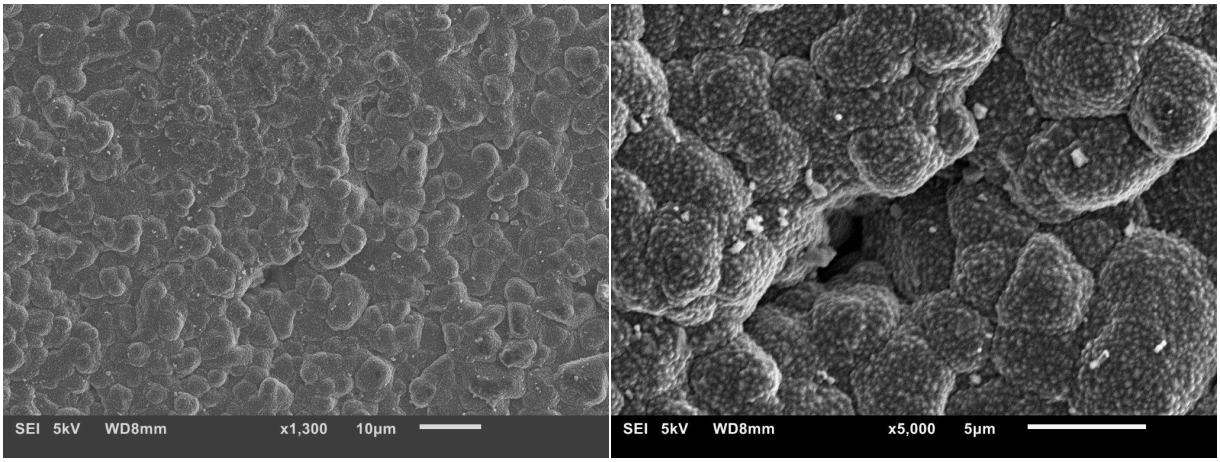

(a) **(b)**

Figure 4.28: SEM micrograph showing the surface morphology of the DropSens BDD at **(a)** 1300x magnification and **(b)** 5000x magnification. Note the presence of a (pin)hole in the electrode surface near the center of image **(b)**.

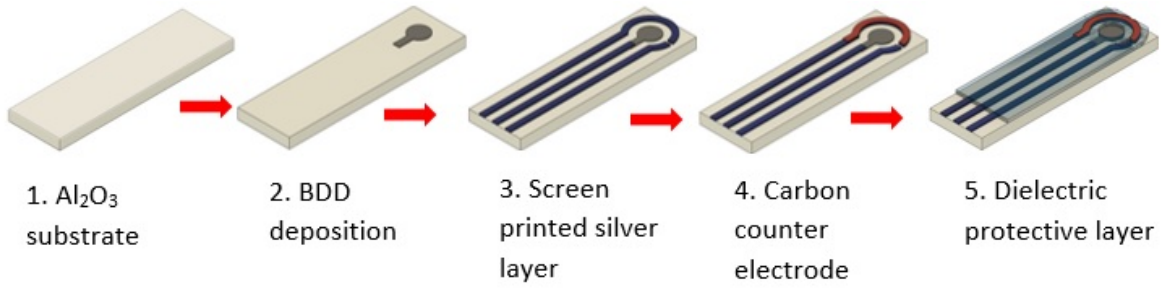

Figure 4.29: Buildup of layers on the DropSens chip electrode

4.8.3 Electrochemical characterization

The final characterization of the DropSens electrode was electrochemical characterization. The CVs for RuHex and ferrocyanide are shown in the appendix Figure E.1. The criteria for ideal reversibility of a one-electrode redox transfer is approximately 58.5 mV peak-to-peak separation at room temperature. The Peak-to-Peak separation for RuHex and ferrocyanide are $\Delta E_p = 122 \pm 18mV$ and $\Delta E_p = 202 \pm 40.5mV$ respectively. Both CVs thus indicate quasi reversibility of the electrode. The larger peak-to-peak separation for ferrocyanide was potentially due to the surface morphology and specific nanocrystalline nature of thet of the DropSens electrode. However, it can also be attributed to oxygen-termination of the surface, since the kinetics of ferrocyanide is sensitive to oxygen on the surface. From the electrochemical experiments, it also became clear that the reference electrode of the chip electrode is problematic for two reasons. The first being that due to exposure to the analyte the reference electrode is not stable. Visually, a colour difference on the reference electrode was observed after use and after the RuHex cycle (Figure E.1a) a new electrode had to be used to get good results from the ferrocyanide scan (Figure E.1c). Another issue is the potential of the silver electrode, this resulted in the anodic peak for RuHex at the point of reversibility (0v), making data processing difficult.

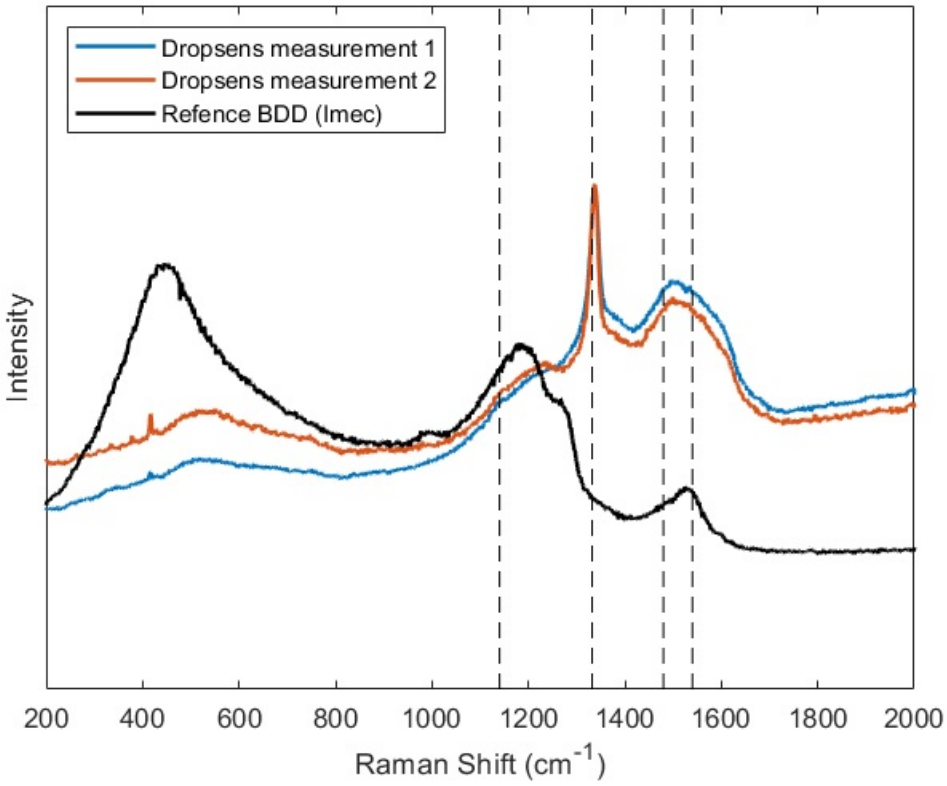

Figure 4.30: Raman spectroscopy of the DropSens and a highly doped BDD electrode as reference, the dotted lines are placed at 1140 cm^{-1}, 1332cm^{-1}, 1480cm^{-1} and 1540 cm^{-1} respectively.

4.9 Future BDD sensor chip fabrication

4.9.1 Boron concentration

For the inkjet printed BDD chip electrode, a higher electrical resistivity ($0.5-2e^{-3}\ \Omega\cdot cm$ [12]) is foreseen as compared to the silver ink ($5e^{-6}\,\Omega\cdot cm$ [91]). The low growth rate of BDD ($\approx 1\,\mu m/h$) and therefore the finite BDD layer thickness obtainable through HFCVD will further limit the conductivity in the leads of the electrode. This is a potential issue for the proper functioning of the future sensor device.

By applying Equation (4.1), a $4-\mu m$ thick BDD layer of width (a) of 1 mm and length (l) of 10 mm results in ohmic resistance between 50-1250 Ω.

$$\omega = \rho \cdot \frac{l}{a} \tag{4.1}$$

Therefore, the thickness of the BDD layer and the boron doping level should be investigated. Potentially boron doping levels just below the metallic threshold, with leads covered by conductive silver, could be advantageous over high boron levels for electrochemical analysis, due to the wider potential window. By printing the leads with silver ink, ohmic resistance in the leads can be reduced by a possible factor three.

4.9.2 Silver printing

As a proof of concept a print using silver ink was done to coat the surface of a diamond electrode pattern. This method may be used to create conductive tracks or print the reference electrode.

One of the issues with printing silver or any ink containing low vapor pressure solvents is the fact that due to solvents present in the ink, the ink quickly dries near the nozzles. Evaporation on the

nozzle plate increases the viscosity, preventing the nozzles from ejecting. After some time, the high viscosity ink mixes with the lower viscosity bulk ink and the desired printing pattern can be produced. This effect is visible on the first print lines, resulting in no drop ejection or satellite droplet formation. There are two ways of solving this issue. One is to directly start printing from the dropview position. The second is to print with a leader bar outside the region of interest to make sure the mixing happens outside of the actual print.

To be able to align the silver ink with the grown diamond film, the steps as discussed in Section 4.2.2 have to be followed. Figure 4.31 shows a thin-film diamond micro-electrode of which a selective region is coated using silver ink. Further research needs to be done into the required amount of silver print layers and optimizing the annealing step has to take place to get high conductivity values for the silver ink.

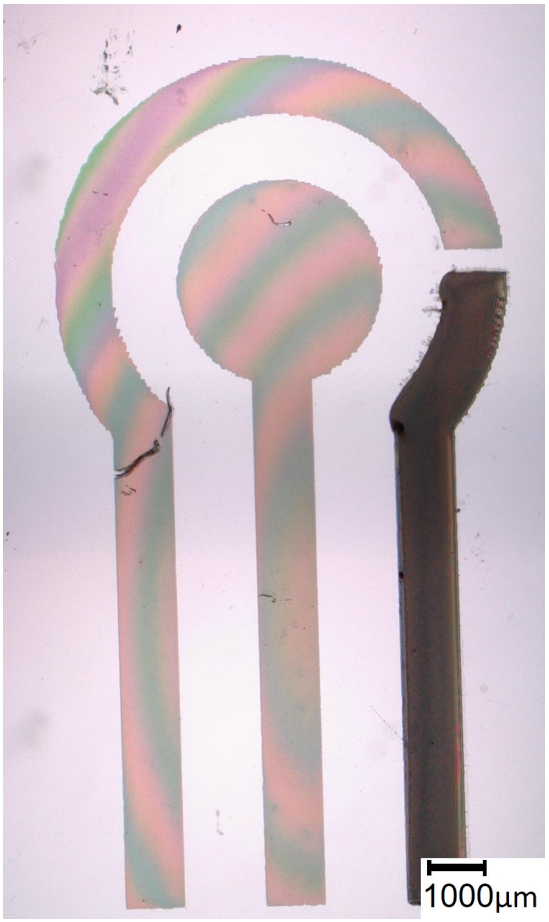

Figure 4.31: Optical microscopy image of a diamond three-electrode sample after CVD diamond growth. Print seeding with diamond NPs was done on an air-exposed, oxygen-plasma treated silicon substrate. The reference electrode (lower right structure) was print-coated with silver ink.

4.9.3 Dielectric layer

To better define the region where the electrochemical detection occurs, and to prevent any electrical contact outside of the working, counter and reference electrodes, printing of a dielectric layer should be investigated as well. There are some SU-8 based dielectric inkjet inks available on the market [92,93], which are used for this purpose. The same layer can also be applied using dip or spin-coating however, the region where the electrochemical reaction is to take place has to be exposed in some way, without leaving residue influencing its electrochemical performance.

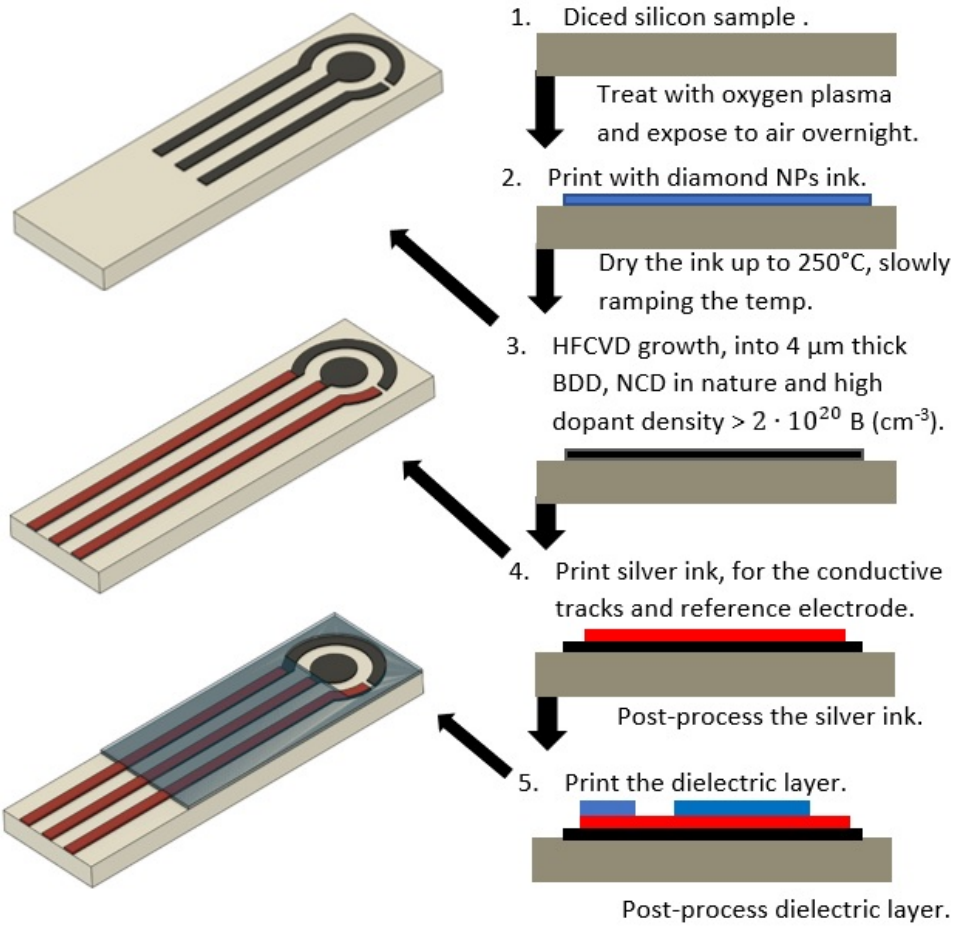

Figure 4.32: Production steps for a BDD sensor chip electrode, using CVD and inkjet printing,

To conclude this chapter the following steps as shown in Figure 4.32 are proposed to produce the BDD sensing chip electrode in follow-up research.

5 Conclusions and Recommendations for future work

5.1 Conclusions

The aim of the project was to develop a BDD sensing chip electrode using bottom-up fabrication techniques. Although no functional BDD could be grown in-house, in this thesis the first steps were taken in producing bottom-up fabricated diamond prototypes using inkjet printing.

Both the Epson and PIXDRO printers are capable of selective seeding the surface for diamond growth and producing continuous micro-electrode shapes. The Epson printer however relies on complete wetting of the substrate, which limits the feature size of the print considerably. Printing with a large number of nozzles simultaneously increases the speed of the printing process for the Epson printer. However, the current hard coding of the designs and the frequent clogging of the nozzles make it a time-consuming process. As compared to the DMC printheads of the PIXDRO printer, the Epson XP-235 does possess a better quality printhead capable of consistently producing drops absent of satellite droplets for a large number of nozzles.

The PIXDRO LP-50, comprising a high resolution motion stage combined with software functionality to quickly translate images into printing patterns, makes printing different designs effortless as compared to the Epson printer, currently the major drawback being the quality of the DMC printheads. The printview camera also makes it possible, unlike the Epson printer, to print directly in a specific location as demonstrated by printing the silver ink layer in section 4.9.2. By modifying the surface with different surface treatments, the PIXDRO printer is able to selectively seed the silicon substrate with sharp features for diamond growth, and the first steps in the bottom-up fabrication of thin-film diamond micro-electrodes have been demonstrated.

Seeding using the inkjet printing process by letting the silicon substrate surface expose to air after an oxygen plasma treatment (2 min at 20W) for a minimum of five hours gave the best result between the various surface treatments. This surface treatment resulted in a state, were with the as-prepared ink solution, 1:1 water:glycerol 0.4% (wt/vol) diamond NPs, continuous films with sharp features and corners could be printed. This method resulted in a contact angle on the silicon substrate of approximately 23°, with a surface free energy of the substrate at 61.6 mN/m. High resolution SEM imaging revealed that the substrate surface is densely seeded with over 50% area coverage. Unfortunately the drying of glycerol left residue on the surface which made it difficult to assess the agglomeration density. However, using standard HFCVD diamond growth (300 $sccm\ H_2$, 6 $sccm\ CH_4$ at 10 mbar, 725°C and 425W filament power) several different micro-electrodes geometries, such as a circular, interdigitated and conventional electrode have been grown in micrometer thick, nanocrystalline diamond, with minimal surface defects. The feature size, achievable with the current technique is approximately 60 μm.

A variety of characterizations (incl. viscosity, optical microscopy, SEM, Raman and electrochemical analyses) were performed on the ink, substrate and commercially available DropSens electrode.

They gave a better understanding on what is required for selective seeding during the inkjet printing process and what properties the electrochemical chip sensor should possess. The seeding requirements and desired sensing electrode properties serve as a guideline for immediate future work, once the new BDD reactor is operational, and BDD electrodes can be fabricated. Electrochemical tests using a DropSens CBDD10 electrode demonstrated that the stability of a solid-state silver reference electrode in contact with solution is problematic for sustained use.

Inkjet printing is a digital, quick and low-cost manufacturing technique, which enables not only the selective seeding of substrates for bottom-up growth of diamond, but additionally is capable of printing additional materials which contribute to the overall performance of the device. Using the optimal print parameters, this thesis demonstrated the ability to produce continuous shapes in thin-film diamond with line feature resolution of approximately 60 μm using a PIXDRO LP-50 printer and DMC 10 pl cartridges. The technique is a viable bottom-up manufacturing process for BDD chip electrodes and potentially other BDD devices, such for example a gas sensors or 2D heater. Yet, due to the instability of the drop ejecting and the relatively slow printing speed, the current DMC-11610 printhead is not suited for larger series production and appears to be limited to prototyping. For large scale production a different printhead is required.

5.2 Recommendations for future work

Inkjet printing has proven to be a promising technique for bottom-up growth of diamond thin-film, the method is fast, low-cost and digital. Due to the fact that during this project no BDD electrodes could be grown, the functionalization test for the electrochemical sensor still has to be performed. Once the new CVD reactor is operational, the technique demonstrated in this thesis can be employed to fabricate, a variety of thin-film BDD sensor devices. Recommendations for future work are proposed as follows.

- There are several ways to increase the printing resolution and produce smaller features. Smaller feature sizes make the inkjet printing technique a potential candidate for bottom-up fabrication technique for MEMS devices. Reduced feature size is required to make it competitive towards more expensive, however often more accurate, top-down processes. Being able to print continuous films at a higher contact angle reduces the spreading of the liquid and thus, the feature size as described by Equation (2.1). Surfactants can be added to the ink to decrease the surface tension and print on pristine silicon, which eliminates the additional oxygen plasma treatment step and can potentially increase the contact angle while still perfectly wetting the surface. Printing with 1 pL printhead properly tuned to produce 1 pL droplets can further reduce the feature resolution.
- The production steps for the dielectric layer, required to define the region where the electrochemical reaction takes place and isolate the electronic leads, requires further research. The dielectric ink based on on SU-8 ink exist however, other production techniques such as dip-coating or spin-coating or potentially even manual application can also be employed.
- During the electrochemical tests performed with the DropSens electrode it became clear that the stability of the reference electrode is a concern. Commercial reference electrodes are stored in a solution of KCl and separated from the analyte to maintain a stable reference potential. Using a solid-state reference electrode, contact with the solution is difficult to prevent. However literature provides examples for coating the reference electrode with Nafion or polyurethane to increase its stability. Additional BDD as a quasi-reference electrode can be investigated, not only does it reduce the production steps for the chip electrode, since BDD is chemical inert it offers chemical stability.
- The thickness of the BDD layer should be investigated. Due to the relatively low growth rate of diamond by HFCVD, layers of only several microns in thickness can be grown in a single deposition run. This limits the cross-sectional area of the leads and can cause high resistance in the leads of the electrodes. By increasing the doping concentration the conductivity can be increased. This does however negatively affect the potential window. The leads of the chip electrode can be coated with a layer of silver ink to increase the conductivity, however this technique might result in an increased contact resistance due to the Schottky barrier between the metal-semiconductor interface, depending on the boron doping level.
- One of the main properties that makes BDD a good candidate for electrochemical analysis in water treatment is its anti-fouling property. However, this property also affects the adhesion of any additional layers to the diamond thin-film. Poor adhesion might result in stripping or delamination of any additional layers, such as the dielectric or silver layers.
- The DPI method for inkjet printing resulted in concentrated spots with a higher density of NPs. These spots remained visible with optical microscopy even after extended growth time whilst SEM imaging shows continuous thin-film, since the diamond NPs used during the seeding steps are intrinsic isolating diamond. These clusters can affect the conductivity of the BDD thin-film. It would be interesting to investigate the effects of these subsurface agglomerations and non-uniformity on the electric and electrochemical properties of boron doped diamond.

Bibliography

[1] NWO-TTW project 16361. Diamond makes sense: Fabrication of novel micro/nano-structured diamond microelectrodes for advanced electrochemical sensing, 2019. URL: https://www.nwo.nl/onderzoek-en-resultaten/programmas/open+technologieprogramma/projecten/2018/2018-16361.

[2] Maxim B. Joseph, Eleni Bitziou, Tania L. Read, Lingcong Meng, Nicola L. Palmer, Tim P. Mollart, Mark E. Newton, and Julie V. Macpherson. Fabrication route for the production of coplanar, diamond insulated, boron doped diamond macro- and microelectrodes of any geometry. *Analytical Chemistry*, 86(11):5238–5244, 2014. doi:10.1021/ac501092y.

[3] Ai Sugitani, Michinobu Katayama, Takeshi Watanabe, Yoshinori Matsumoto, and Yasuaki Einaga. Fabrication of boron doped diamond chip electrodes for single drop analysis. *RSC Adv.*, 3:25636–25639, 2013. doi:10.1039/C3RA44090G.

[4] Supil Raina, W.P. Kang, and J.L. Davidson. Nitrogen incorporated nanodiamond film with 'ridge' surface morphology for detection of bio-analyte. *Diamond and Related Materials*, 18(2):574 – 577, 2009. NDNC 2008 Proceedings of the International Conference on New Diamond and Nano Carbons 2008. doi:10.1016/j.diamond.2008.11.016.

[5] Violette Geissen, Hans Mol, Erwin Klumpp, Günter Umlauf, Marti Nadal, Martine van der Ploeg, Sjoerd E.A.T.M. van de Zee, and Coen J. Ritsema. Emerging pollutants in the environment: A challenge for water resource management. *International Soil and Water Conservation Research*, 3(1):57 – 65, 2015. doi:10.1016/j.iswcr.2015.03.002.

[6] Marianne Stuart, Dan Lapworth, Emily Crane, and Alwyn Hart. Review of risk from potential emerging contaminants in uk groundwater. *Science of The Total Environment*, 416:1 – 21, 2012. doi:10.1016/j.scitotenv.2011.11.072.

[7] Susan D. Richardson and Thomas A. Ternes. Water analysis:emerging contaminants and current issues. *Analytical Chemistry*, 77(12):3807–3838, 2005. doi:10.1021/ac058022x.

[8] Jafar Safaa Noori, Maria Dimaki, John Mortensen, and Winnie E. Svendsen. Detection of glyphosate in drinking water: A fast and direct detection method without sample pretreatment. *Sensors*, 18(9), 2018. doi:10.3390/s18092961.

[9] Torsten C. Schmidt. Recent trends in water analysis triggering future monitoring of organic micropollutants. *Analytical and Bioanalytical Chemistry*, 410(17):3933–3941, Jul 2018. doi:10.1007/s00216-018-1015-9.

[10] Carlos A Martinez-Huitle. Conductive diamond electrodes for water purification. *Materials Research-ibero-american Journal of Materials*, 10, 10 2007. doi:10.1590/S1516-14392007000400016.

[11] Nianjun Yang, Siyu Yu, Julie V. Macpherson, Yasuaki Einaga, Hongying Zhao, Guohua Zhao, Greg M. Swain, and Xin Jiang. Conductive diamond: synthesis, properties, and electrochemical applications. *Chem. Soc. Rev.*, 48:157–204, 2019. doi:10.1039/C7CS00757D.

[12] Julie Macpherson. A practical guide to using boron doped diamond in electrochemical research. *Physical chemistry chemical physics : PCCP*, 17, 12 2014. doi:10.1039/c4cp04022h.

[13] O.A. Williams. Nanocrystalline diamond. *Diamond and Related Materials*, 20(5):621 – 640, 2011. doi:10.1016/j.diamond.2011.02.015.

[14] Awadesh Mallik, Joana Mendes, Shlomo Z Rotter, and Sandip Bysakh. Detonation nanodiamond seeding technique for nucleation enhancement of cvd diamond – some experimental insights. *Advances in Ceramic Science and Engineering*, 3, 05 2014. doi:10.14355/acse.2014.03.005.

[15] Chia-Fu Chen, Sheng-Hsiung Chen, Tsao-Ming Hong, and Ming-Hsing Tsai. Improvement of selectivity during diamond growth utilizing a new process. *Journal of Applied Physics*, 77(2):940–942, 1995. doi:10.1063/1.359023.

[16] André F. Sartori, Pierpaolo Belardinelli, Robin J. Dolleman, Peter G. Steeneken, Murali K. Ghatkesar, and Josephus G. Buijnsters. Inkjet-printed high-q nanocrystalline diamond resonators. *Small (online)*, 15(4), 2019. doi:10.1002/smll.201803774.

[17] Alice C. Taylor, Robert Edgington, and Richard B. Jackman. Patterning of nanodiamond tracks and nanocrystalline diamond films using a micropipette for additive direct-write processing. *ACS Applied Materials & Interfaces*, 7(12):6490–6495, 2015. doi:10.1021/am507900a.

[18] André F. Sartori, Bart H.L. Overes, Paola Fanzio, Menelaos Tsigkourakos, Luigi Sasso, and Josephus G. Buijnsters. Template-assisted bottom-up growth of nanocrystalline diamond micropillar arrays. *Diamond and Related Materials*, 95:20 – 27, 2019. doi:10.1016/j.diamond.2019.03.017.

[19] Menelaos Tsigkourakos, Thomas Hantschel, Christophe Bangerter, and Wilfried Vandervorst. Electrical probing of b-doped diamond seeds embedded into the interfacial layer of a conductive diamond film. *physica status solidi (a)*, 211(10):2284–2289, 2014. doi:10.1002/pssa.201431215.

[20] Abdulkareem Afandi, Ashley Howkins, Ian W. Boyd, and Richard B. Jackman. Nanodiamonds for device applications: An investigation of the properties of boron-doped detonation nanodiamonds. *Scientific Reports*, 8(1):3270, 2018. doi:10.1038/s41598-018-21670-w.

[21] Laia Ginés, Soumen Mandal, David John Morgan, Ryan Lewis, Philip R. Davies, Paola Borri, Gavin W. Morley, and Oliver A. Williams. Production of metal-free diamond nanoparticles. *ACS Omega*, 3(11):16099–16104, 2018. doi:10.1021/acsomega.8b02067.

[22] Steffen Heyer, Wiebke Janssen, Stuart Turner, Ying-Gang Lu, Weng Siang Yeap, Jo Verbeeck, Ken Haenen, and Anke Krueger. Toward deep blue nano hope diamonds: Heavily boron-doped diamond nanoparticles. *ACS Nano*, 8(6):5757–5764, 2014. doi:10.1021/nn500573x.

[23] Fabrizio Cleri, P Keblinski, L Colombo, D Wolf, and R Phillpot. On the electrical activity of sp2-bonded grain boundaries in nanocrystalline diamond. *EPL (Europhysics Letters)*, 46:671, 01 2007. doi:10.1209/epl/i1999-00318-5.

[24] Samuel J. Cobb, Zoe J. Ayres, and Julie V. Macpherson. Boron doped diamond: A designer electrode material for the twenty-first century. *Annual Review of Analytical Chemistry*, 11(1):463–484, 2018. doi:10.1146/annurev-anchem-061417-010107.

[25] Danyelle Medeiros de Araújo, Pablo Cañizares, Carlos A. Martínez-Huitle, and Manuel Andrés Rodrigo. Electrochemical conversion/combustion of a model organic pollutant on BDD anode: Role of sp3/sp2 ratio. *Electrochemistry Communications*, 47:37 – 40, 2014. doi:10.1016/j.elecom.2014.07.017.

[26] Kateryna Muzyka, Jianrui Sun, Tadesse Haile Fereja, Yixiang Lan, Wei Zhang, and Guobao Xu. Boron-doped diamond: current progress and challenges in view of electroanalytical applications. *Anal. Methods*, 11:397–414, 2019. doi:10.1039/C8AY02197J.

[27] Ana Moya, Gemma Gabriel, Rosa Villa, and F. Javier del Campo. Inkjet-printed electrochemical sensors. *Current Opinion in Electrochemistry*, 3(1):29 – 39, 2017. doi:10.1016/j.coelec.2017.05.003.

[28] Helmut Kipphan, editor. *Handbook of Print Media*. Springer Berlin Heidelberg, 2001. doi:10.1007/978-3-540-29900-4.

[29] Taewoong Lim, Sewoon Han, Jaewon Chung, Jin Taek Chung, Seunghwan Ko, and Costas P. Grigoropoulos. Experimental study on spreading and evaporation of inkjet printed pico-liter droplet on a heated substrate. *International Journal of Heat and Mass Transfer*, 52(1):431 – 441, 2009. doi:10.1016/j.ijheatmasstransfer.2008.05.028.

[30] Anke Teichler, Jolke Perelaer, and Ulrich S. Schubert. Inkjet printing of organic electronics – comparison of deposition techniques and state-of-the-art developments. *J. Mater. Chem. C*, 1:1910–1925, 2013. doi:10.1039/C2TC00255H.

[31] Brian Derby. Inkjet printing of functional and structural materials: Fluid property requirements, feature stability, and resolution. *Annual Review of Materials Research*, 40(1):395–414, 2010. doi:10.1146/annurev-matsci-070909-104502.

[32] K. Ton, T. Chu, Z. Zhang, and Y. Tao. Printing contractive silver conductive inks using interface interactions to overcome dewetting. *IEEE Journal of the Electron Devices Society*, 7:756–760, 2019.

[33] Hua Hu and Ronald G Larson. Marangoni effect reverses coffee-ring depositions. *The journal of physical chemistry. B*, 110(14):7090—7094, April 2006. doi:10.1021/jp0609232.

[34] Xuefeng Xu, Jianbin Luo, and Dan Guo. Criterion for reversal of thermal marangoni flow in drying drops. *Langmuir*, 26(3):1918–1922, 2010. doi:10.1021/la902666r.

[35] Emine Tekin, Berend-Jan Gans, and Ulrich Schubert. Ink-jet printing of polymers—from single dots to thin film libraries. *J. Mater. Chem.*, 14, 08 2004. doi:10.1039/B407478E.

[36] Pavan Pujar, Pallapati Anusha, Dipti Gupta, and Saumen Mandal. Investigation of sintering kinetics and morphological evolution of silver films from nano-dispersion. *Applied Physics A*, 124, 11 2018. doi:10.1007/s00339-018-2249-2.

[37] Hongming Dong, Wallace W. Carr, and Jeffrey F. Morris. An experimental study of drop-on-demand drop formation. *Physics of Fluids*, 18(7):072102, 2006. doi:10.1063/1.2217929.

[38] Junchun Yu Tuser T. Biswas and Vincent A. Nierstra. Effects of ink characteristics and piezo-electric inkjetting parameters on lysozyme activity. *Scientific Reports*, 9, 2019. doi:10.1038/s41598-019-54723-9.

[39] Douglas Rice, Paul Westerhoff, Francois Perreault, and Sergio GARCIA SEGURA. Electrochemical self-cleaning anodic surfaces for biofouling control during water treatment. *Electrochemistry Communications*, 96:83–87, 11 2018. doi:10.1016/j.elecom.2018.10.002.

[40] Susha Cheriyedath. Electrochemical analysis, 2019-02-26. URL: https://www.news-medical.net/life-sciences/Electrochemical-Analysis.aspx.

[41] Noémie Elgrishi, Kelley J. Rountree, Brian D. McCarthy, Eric S. Rountree, Thomas T. Eisenhart, and Jillian L. Dempsey. A practical beginner's guide to cyclic voltammetry. *Journal of Chemical Education*, 95(2):197–206, 2018. doi:10.1021/acs.jchemed.7b00361.

[42] Munawar Khalil, Sai Wang, Jianjia Yu, Robert Lee, and Wenbing Li. Electrodeposition of iridium oxide nanoparticles for ph sensing electrodes. *Journal of The Electrochemical Society*, 163:B485–B490, 01 2016. doi:10.1149/2.0391609jes.

[43] Ltd ALS Co. Counter electrode, 2019-06-30. URL: https://www.als-japan.com/1787.html.

[44] Yasuaki Einaga. Diamond electrodes for electrochemical analysis. *Journal of Applied Electrochemistry*, 40(10):1807–1816, Oct 2010. doi:10.1007/s10800-010-0112-z.

[45] Yongtak Yang, Jeong Wook Oh, Yang Rae Kim, Chiaki Terashima, Akira Fujishima, Jong Seung Kim, and Hasuck Kim. Enhanced electrogenerated chemiluminescence of a ruthenium trisbipyridyl/tripropylamine system on a boron-doped diamond nanograss array. *Chemical Communications*, 46(31):5793–5795, 8 2010. doi:10.1039/c0cc00773k.

[46] Amanda B. Lima, Eric O. Faria, Rodrigo H. O. Montes, Rafael R. Cunha, Eduardo M. Richter, Rodrigo A. A. Munoz, and Wallans T. P. dos Santos. Electrochemical oxidation of ibuprofen and its voltammetric determination at a boron-doped diamond electrode. *Electroanalysis*, 25(7):1585–1588, 2013. doi:10.1002/elan.201300014.

[47] Jayakumar Shalini, Kamatchi Jothiramalingam Sankaran, Chung-Li Dong, Chi-Young Lee, Nyan-Hwa Tai, and I-Nan Lin. In situ detection of dopamine using nitrogen incorporated diamond nanowire electrode. *Nanoscale*, 5:1159–1167, 2013. doi:10.1039/C2NR32939E.

[48] Ademar Wong, Anderson Martin Santos, and Orlando Fatibello-Filho. Simultaneous determination of dopamine and cysteamine by flow injection with multiple pulse amperometric detection using a boron-doped diamond electrode. *Diamond and Related Materials*, 85:68 – 73, 2018. doi:10.1016/j.diamond.2018.03.034.

[49] Katarzyna Tyszczuk-Rotko, Izabela Jaworska, and Katarzyna Jędruchniewicz. Application of unmodified boron-doped diamond electrode for determination of dopamine and paracetamol. *Microchemical Journal*, 146:664 – 672, 2019. doi:10.1016/j.microc.2019.01.064.

[50] Simona Baluchová, Aleš Daňhel, Hana Dejmková, Veronika Ostatná, Miroslav Fojta, and Karolina Schwarzová-Pecková. Recent progress in the applications of boron doped diamond electrodes in electroanalysis of organic compounds and biomolecules – a review. *Analytica Chimica Acta*, 1077:30 – 66, 2019. doi:10.1016/j.aca.2019.05.041.

[51] Omar Tall, Nicole Jaffrezic-Renault, Monique Sigaud, and Olivier Vittori. Anodic stripping voltammetry of heavy metals at nanocrystalline boron-doped diamond electrode. *Electroanalysis*, 19:1152 – 1159, 06 2007. doi:10.1002/elan.200603834.

[52] Su Li, Chencheng Zhang, Shengnan Wang, Qing Liu, Huanhuan Feng, Xing Ma, and Jinhong Guo. Electrochemical microfluidics techniques for heavy metal ion detection. *Analyst*, 143:4230–4246, 2018. doi:10.1039/C8AN01067F.

[53] Omar El Tall, Nicole Jaffrezic-Renault, Monique Sigaud, and Olivier Vittori. Anodic stripping voltammetry of heavy metals at nanocrystalline boron-doped diamond electrode. *Electroanalysis*, 19(11):1152–1159, 2007. doi:10.1002/elan.200603834.

[54] Christophe Provent, Werner Haenni, Eduardo Santoli, and Philippe Rychen. Boron-doped diamond electrodes and microelectrode-arrays for the measurement of sulfate and peroxodisulfate. *Electrochimica Acta*, 49(22):3737 – 3744, 2004. The role of electrochemistry in the sustained development of modern societies. doi:10.1016/j.electacta.2004.02.047.

[55] Amel Sbartai, Philippe Namour, Abdelhamid Errachid, Jan Krejči, Romana Šejnohová, Louis Renaud, Mohamed Larbi Hamlaoui, Anne-Sophie Loir, Florence Garrelie, Christophe Donnet, Hervé Soder, Eric Audouard, Julien Granier, and Nicole Jaffrezic-Renault. Electrochemical boron-doped diamond film microcells micromachined with femtosecond laser: Application to the determination of water framework directive metals. *Analytical Chemistry*, 84(11):4805–4811, 2012. PMID: 22510091. doi:10.1021/ac3003598.

[56] Eleni Bitziou, Maxim B. Joseph, Tania L. Read, Nicola Palmer, Tim Mollart, Mark E. Newton, and Julie V. Macpherson. In situ optimization of ph for parts-per-billion electrochemical detection of dissolved hydrogen sulfide using boron doped diamond flow electrodes. *Analytical Chemistry*, 86(21):10834–10840, 2014. doi:10.1021/ac502941h.

[57] Takeshi Watanabe, Shuhei Shibano, Hideto Maeda, Ai Sugitani, Michinobu Katayama, Yoshinori Matsumoto, and Yasuaki Einaga. Fabrication of a microfluidic device with boron-doped diamond electrodes for electrochemical analysis. *Electrochimica Acta*, 197:159 – 166, 2016. doi:10.1016/j.electacta.2015.11.035.

[58] M. Bonnauron, S. Saada, C. Mer, C. Gesset, O. A. Williams, L. Rousseau, E. Scorsone, P. Mailley, M. Nesladek, J.-C. Arnault, and P. Bergonzo. Transparent diamond-on-glass micro-electrode arrays for ex-vivo neuronal study. *physica status solidi (a)*, 205(9):2126–2129, 2008. doi:10.1002/pssa.200879733.

[59] Yu-Chun Chen, Yonhua Tzeng, Ahbishek Davray, An-Jen Cheng, Ramesh Ramadoss, and Minseo Park. Fabrication of diamond micro-structures by ink-jet printed diamond seeding and microwave plasma assisted chemical vapor deposition. *Diamond and Related Materials*, 17(4):722 – 727, 2008. NDNC 2007 Proceedings of the International Conference on New Diamond and Nano Carbons 2007. doi:10.1016/j.diamond.2008.01.021.

[60] Yu-Chun Chen, Yonhua Tzeng, An-Jen Cheng, Robert Dean, Minseo Park, and Bogdan M. Wilamowski. Inkjet printing of nanodiamond suspensions in ethylene glycol for cvd growth of patterned diamond structures and practical applications. *Diamond and Related Materials*, 18(2):146 – 150, 2009. NDNC 2008 Proceedings of the International Conference on New Diamond and Nano Carbons 2008. doi:10.1016/j.diamond.2008.10.004.

[61] Ryan P. Tortorich, Hamed Shamkhalichenar, and Jin-Woo Choi. Inkjet-printed and paper-based electrochemical sensors. *Applied Sciences*, 8(2), 2018. doi:10.3390/app8020288.

[62] Laxmidhar Nayak, Smita Mohanty, Sanjay Kumar Nayak, and Ananthakumar Ramadoss. A review on inkjet printing of nanoparticle inks for flexible electronics. *J. Mater. Chem. C*, 7:8771–8795, 2019. doi:10.1039/C9TC01630A.

[63] Wijitar Dungchai, Orawon Chailapakul, and Charles S. Henry. Electrochemical detection for paper-based microfluidics. *Analytical Chemistry*, 81(14):5821–5826, 2009. doi:10.1021/ac9007573.

[64] Ehab Saleh, Fan Zhang, Yinfeng He, Jayasheelan Vaithilingam, Javier Fernandez, Ricky Wildman, Ian Ashcroft, Richard Hague, Philip Dickens, and Christopher Tuck. 3d inkjet printing of electronics using uv conversion. *Advanced Materials Technologies*, 2, 06 2017. doi:10.1002/admt.201700134.

[65] Agostino Romeo, Ana Moya, Tammy S. Leung, Gemma Gabriel, Rosa Villa, and Samuel Sánchez. Inkjet printed flexible non-enzymatic glucose sensor for tear fluid analysis. *Applied Materials Today*, 10:133 – 141, 2018. doi:0.1016/j.apmt.2017.12.016.

[66] Alina Vasilescu, Gilvanda Nunes, Akhtar Hayat, Usman Latif, and Jean Marty. Electrochemical affinity biosensors based on disposable screen-printed electrodes for detection of food allergens. *Sensors*, 16:1863, 11 2016. doi:10.3390/s16111863.

[67] Methrohm dropsens. Screen printed bdd electrode, 2019-08-18. URL: http://www.dropsens.com/en/pdfs_productos/new_brochures/bdd10-cbdd10.pdf.

[68] Jaymin K. Jadav, Valentina V. Umrania, Khyati J. Rathod, and Baljibhai A. Golakiya. Development of silver/carbon screen-printed electrode for rapid determination of vitamin c from fruit juices. *LWT*, 88:152 – 158, 2018. doi:10.1016/j.lwt.2017.10.005.

[69] Michael E. Hyde, Robert M.J. Jacobs, and Richard G. Compton. An electrodeposition study of the nucleation and growth of silver on boron-doped diamond electrodes. *Journal of Electroanalytical Chemistry*, 562(1):61 – 72, 2004. doi:10.1016/j.jelechem.2003.08.009.

[70] Brian Polk, Anna Stelzenmuller, Geraldine Mijares, William MacCrehan, and Michael Gaitan. Ag/agcl microelectrodes with improved stability for microfluidics. *Sensors and Actuators B: Chemical*, 114(1):239 – 247, 2006. doi:10.1016/j.snb.2005.03.121.

[71] Mary Ensch, Vanessa Y. Maldonado, Greg M. Swain, Robert Rechenberg, Michael F. Becker, Thomas Schuelke, and Cory A. Rusinek. Isatin detection using a boron-doped diamond 3-in-1 sensing platform. *Analytical Chemistry*, 90(3):1951–1958, 2018. doi:10.1021/acs.analchem.7b04045.

[72] Yinyue Wang, XQ Liu, Congmian Zhen, Hengxiang Gong, Zhijun Yan, Yinghu Yang, and Shuyi Ma. Ohmic contacts and interface properties of au/ti/p-diamond prepared by r.f. sputtering. *Surface and Interface Analysis - SURF INTERFACE ANAL*, 29:478–481, 07 2000. doi:10.1002/1096-9918(200007)29:7<478::AID-SIA887>3.0.CO;2-A.

[73] Jiro Nakanishi, A. Otsuki, T. Oku, O. Ishiwata, and Masanori Murakami. Formation of ohmic contacts to p-type diamond using carbide forming metals. *Journal of Applied Physics*, 76(4):2293–2298, 1994. doi:10.1063/1.357649.

[74] Rick Waasdorp, Oscar van den Heuvel, Floyd Versluis, Bram Hajee, and Murali Krishna Ghatkesar. Accessing individual 75-micron diameter nozzles of a desktop inkjet printer to dispense picoliter droplets on demand. *RSC Adv.*, 8:14765–14774, 2018. doi:10.1039/C8RA00756J.

[75] Koichi Takamura, Herbert Fischer, and Norman Morrow. Physical properties of aqueous glycerol solutions. *Journal of Petroleum Science and Engineering*, 98-99:50 – 60, 2012. doi:10.1016/j.petrol.2012.09.003.

[76] Emma Spooner. A Guide to Surface Energy. Technical report, University of Sheffield in collaboration with Ossila Ltd, 2020. URL: https://www.ossila.com/pages/a-guide-to-surface-energy.

[77] SK. TN310e Effect of drop volume on static contact angles. Technical report, KRÜSS GmbH, 2004. URL: https://www.kruss-scientific.com/fileadmin/user_upload/website/literature/kruss-tn310-en.pdf.

[78] CR. TN306e So You Want to Measure Surface Energy? Technical report, KRÜSS GmbH, 06 1999. URL: https://www.kruss-scientific.com/fileadmin/user_upload/website/literature/kruss-tn306-en.pdf.

[79] Menelaos Tsigkourakos, Thomas Hantschel, Stoffel D. Janssens, Ken Haenen, and Wilfried Vandervorst. Spin-seeding approach for diamond growth on large area silicon-wafer substrates. *physica status solidi (a)*, 209(9):1659–1663, 2012. doi:10.1002/pssa.201200137.

[80] NanoCarbon Research Institude LTD. Important notice on the use of our nanoamando as seeding, 2018. URL: http://nano-carbon.jp/english/item_100.html.

[81] M. Rudigier and R Haubner. Characterisation of diamond coatings with different morphologies by raman spectroscopy using various laser wavelengths. *Analytical and Bioanalytical Chemistry volume*, 403:675–681, 01 2012. doi:10.1007/s00216-012-5808-y.

[82] Javier P. Vallejo, Gaweł Żyła, José Fernández-Seara, and Luis Lugo. Influence of six carbon-based nanomaterials on the rheological properties of nanofluids. *Nanomaterials*, 9(2):5821–5826, 2019. doi:10.3390/nano9020146.

[83] C. Diddens, J.G.M. Kuerten, C.W.M. van der Geld, and H.M.A. Wijshoff. Modeling the evaporation of sessile multi-component droplets. *Journal of Colloid and Interface Science*, 487:426 – 436, 2017. doi:10.1016/j.jcis.2016.10.030.

[84] Arif Ul Alam, Matiar Howlader, and M.J. Deen. The effects of oxygen plasma and humidity on surface roughness, water contact angle and hardness of silicon, silicon dioxide and glass. *Journal of Micromechanics and Microengineering*, 24:035010, 02 2014. doi:10.1088/0960-1317/24/3/035010.

[85] Mike Kaszuba. Dynamic Light Scattering:An Introduction in 30 Minutes. Technical report, Malvern instruments, 2017. URL: https://warwick.ac.uk/fac/cross_fac/sciencecity/programmes/internal/themes/am2/booking/particlesize/intro_to_dls.pdf.

[86] Qing Zhang, Yanming Liu, Shuo Chen, Xie Quan, and Hongtao Yu. Nitrogen-doped diamond electrode shows high performance for electrochemical reduction of nitrobenzene. *Journal of Hazardous Materials*, 265:185 – 190, 2014. doi:10.1016/j.jhazmat.2013.11.065.

[87] Supil Raina, W.P. Kang, and J.L. Davidson. Nitrogen incorporated nanodiamond film with 'ridge' surface morphology for detection of bio-analyte. *Diamond and Related Materials*, 18(2):574 – 577, 2009. NDNC 2008 Proceedings of the International Conference on New Diamond and Nano Carbons 2008. doi:10.1016/j.diamond.2008.11.016.

[88] M. Mertens, I.-N. Lin, D. Manoharan, A. Moeinian, K. Brühne, and H. J. Fecht. Structural properties of highly conductive ultra-nanocrystalline diamond films grown by hot-filament cvd. *AIP Advances*, 7(1):015312, 2017. doi:10.1063/1.4975226.

[89] Josephus G. Buijnsters, Jean-Pierre Celis, Ruud W. A. Hendrikx, and Luis Vázquez. Metallic seed nanolayers for enhanced nucleation of nanocrystalline diamond thin films. *The Journal of Physical Chemistry C*, 117(44):23322–23332, 2013. doi:10.1021/jp4071482.

[90] Determination of atomic boron concentration in heavily boron-doped diamond by raman spectroscopy. *Diamond and Related Materials*, 93:54 – 58, 2019. doi:10.1016/j.diamond.2019.01.028.

[91] NovaCentrix. Metalon JS-B25P. Technical report, NovaCentrix, 2011. URL: https://www.novacentrix.com/sites/default/files/pdf/Metalon%20JS-BxxP_2226_6-en.pdf.

[92] Malo Robin, Wenlin Kuai, Maria Amela-Cortes, Stéphane Cordier, Yann Molard, Tayeb Mohammed-Brahim, Emmanuel Jacques, and Maxime Harnois. Epoxy based ink as versatile material for inkjet-printed devices. *ACS applied materials & interfaces*, 7, 09 2015. doi:10.1021/acsami.5b06678.

[93] KAYAKU. Prielex® jettable polymeric materials, 2020. URL: https://kayakuam.com/products/prielex-jettable-polymeric-materials/.

A Step by step guide: Printing with the Epson Printer

Setup virtual enviroment and ESCP-tweak This chapter is a detailed description of how to print using the Hacked Epson printer using the ESCP-tweak software. The manual will start with the software side and continue with the hardware steps. The Tweak ESCP software is run using python V3 and it is recommended to run it in a virtual environment. This manual will run the virtual environment using Anaconda and does any scripting using Spyder. Create a new virtual environment for the Epson printer based on python V3 and the following packages.
∘ Pillow
∘ Pyserial
∘ Tk
∘ Prettytable (requires installation through the terminal using the following command:
"conda install -c conda-forge prettytable". The terminal can be accessed through the arrow symbol next to your virtual environment. Now start the Spyder and run main_gui.py

Setup Network printer
The network location and the printer is required as input for the Graphical User Interface (GUI) Figure A.1 to be able to parse the print file to the printer. It is also recommended to hardcode this location into the script in line 2071. Figure A.2.

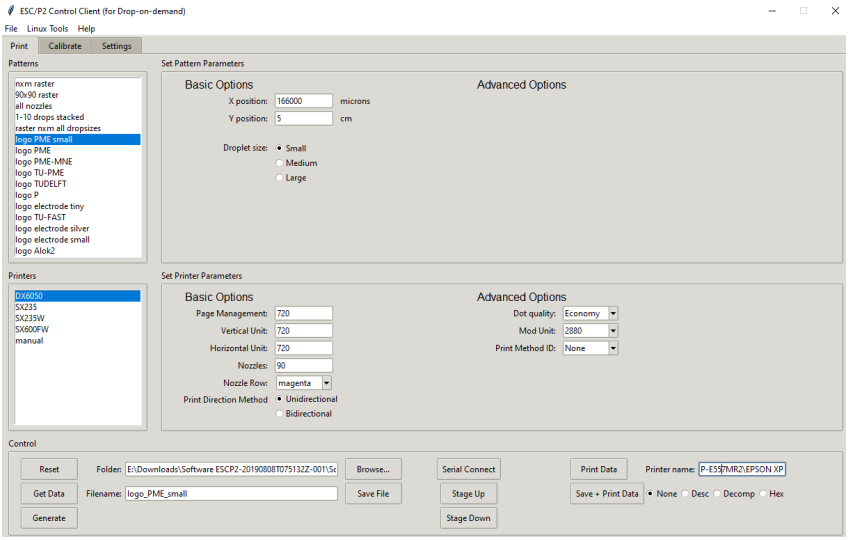

Figure A.1: the ESCP-Tweak Graphical User interface.

Using the GUI, several print settings can be set according to the scripting of the print pattern. Options include: which color to use, the droplet size and the X and Y position of the print pattern. The Y position change is limited and only possible while printing with a small number of nozzles, it relies on changing the starting nozzle number. By selecting print, a print file will be parsed and send to the printer.

Scripting
The hard coding is done in 3 different sections of the main_gui script. The pattern names listed in Figure A.3 are available for printing through the GUI, they can be defined from line 1344. The parameters define the default values when opening a specific pattern in the GUI, the most important line is the command variable, which refers to the print pattern definition. The print pattern definitions shown in Figure A.4 can either be used to create simple script, similar to line 356-368, or refer

```
2064 # ============================
2065 # CONTROL FRAME
2066 # ============================
2067 current_dir = os.path.dirname(os.path.realpath(__file__))
2068 save_dir_var = tk.StringVar()
2069 save_dir_var.set(current_dir+'/output')
2070 lpname_var = tk.StringVar()
2071 lpname_var.set(r'\\DESKTOP-E557MR2\EPSON XP-235 Series')
2072
2073 ParseOpt = [("None", "None"), ("Desc", "v"), ("Decomp", "V"), ("Hex", "ghex")]
2074 ParseOpt_var = tk.StringVar()
2075 ParseOpt_var.set("None")
2076
```

Figure A.2: Example of how to hardcode the printer location in the ESCP-tweak

```
1343 # ---- Initialisation of Contstants
1344 patterns={}
1345 def load_patterns(event=None):
1346     global patterns
1347     patterns = {
1348         # 'Load Bitmap':{'posx':      [True, 14],
1349         #                'posy':      [True, 5],
1350         #                'dx':        [False, 250],
1351         #                'dy':        [False, 0],
1352         #                'rdx':       [False, 0],
1353         #                'widthn':    [False, 6],
1354         #                'heightm':   [False, 10],
1355         #                'dropsize':  [False, 1],
1356         #                'fan':       [False, 0],
1357         #                'rep':       [True, 1],
1358         #                'stretch':   [True, 3],
1359         #                'color':     [True, 'black'],
1360         #                'command':   [nothing, 0]},
1361         'nxm raster' : {'posx':     [True, 166000],
1362                         'posy':     [True,5],
1363                         'dx':       [True, 250],
1364                         'dy':       [True, 0],
1365                         'rdx':      [False, 0],
1366                         'widthn':   [True, 1],
1367                         'heightm':  [True, 1],
1368                         'dropsize': [True, 1],
1369                         'fan':      [True,0],
1370                         'rep':      [True,1],
1371                         'stretch':  [False,0],
1372                         'color' :   [False,'magenta'],
1373                         'command' : [p_raster_nxm,0]},
1374         '90x90 raster' : {'posx':   [True, 166000],
1375                         'posy':     [True,5],
1376                         'dx':       [True, 211.6666666666667],
1377                         'dy':       [False, 0],
1378                         'rdx':      [False, 0],
1379                         'widthn':   [False, 90],
1380                         'heightm':  [False, 90],
1381                         'dropsize': [True, 1],
1382                         'fan':      [False,0],
1383                         'rep':      [True,1],
1384                         'stretch':  [False,0],
1385                         'color' :   [False,'magenta'],
1386                         'command' : [p_raster_90x90,0]},
```

Figure A.3: Script defines the print patterns available in the ESPC GUI.

to the create definition, called in line 373, which is discussed in the next section.

Figure A.5 illustrates a brief example script for printing the letter *P*. The start of the script defines the spacing of the droplets. The separation between the individual nozzles is 1/120 inch; therefore there is no control over the *dy* direction, line 3. However, the distance between vertical lines can be controlled by changing the *dx* value, line 4, change from 1/120 to 1/240, reduces the drop spacing by half, alternatively this can be set location of the nozzle lists, line 20-22, by changing the value before dx. In this example, there is equal spacing in x and y directions given that $dx = 1/120 Inch$. With the list definition, line 7-9, different nozzles can be selected for the vertical print lines. The letter *P* in this example is printed using three vertical lines. The first list addresses nozzles 1-5 of the available 42 nozzles in each colour. The second list addresses only two nozzles, and the third addresses three nozzles. The image is created by determining the horizontal position of the nozzle lists, line 20-22. Furthermore, for every nozzle list a specific colour can be selected from the graphical user interface (GUI), representing the different inks, if the value is set to r like line 20, however by hard coding the color like line 21 and 22, the GUI input value have no effect. To print with different inks or colours at the same time, the colours must be hard coded. In addition, droplet sizes can be selected based on the three available options from the Epson firmware. These can again be hard code, specifying, small, medium or large or selected using the GUI, by inputting size. Once the scripting is done, we can start to loot at the hardware side of printing with the Epson.

Printing

Place a glass microscopic slide on the left side of the printer, in the case of printing with the printer modified for this project. There is a slot at the bottom where the glass slides fits level with the bottom of the printer Figure A.6, or the motion stage, which also has slot for a glass slide. The print location for this glass slide is between 110000-190000 microns in the ESPC-Tweak GUI. Otherwise, remove the bottom of the printer using a screw at both sides. Cut the removed part in half

```
355
356 def p_black_line(**kwargs):
357     nozzlelist = createnozzlelist(42,42,0,0)
358     size = 1
359     raster1 = b''
360     raster2 = b''
361     raster3 = b''
362     # color = black
363     for k in range(1):
364         raster1 += ESC_dollar(hor,x+dx*k) + ESC_i_nrs(nozzlelist,color,size)
365         #raster2 += ESC_dollar(hor,x+dx*k) + ESC_i_nrs(nozzlelist,black2,size)
366         #raster3 += ESC_dollar(hor,x+dx*k) + ESC_i_nrs(nozzlelist,black3,size)
367         rasterdata = ESC_v(pmgmt,y) + raster1+ b'\x0c'
368         return rasterdata
369
370 def p_electrode_tiny(**kwargs):
371     dy = 0
372     dx = (dy + 1) * (1 / 240)
373     rasterdata = ESC_v(pmgmt, y) + (createElectrodeTiny(x, size=size, pmgmt=pmg
374     return rasterdata
375
```

Figure A.4: Caption

```
1
2   def createPs(x, r=b'\x00', size=1, **kwargs):
3       dy = 0
4       dx = (dy + 1) * (1 / 120)
5       hor = 5760
6
7       list1 = createnozzlelistsp(42, [1, 2, 3, 4, 5])
8       list2 = createnozzlelistsp(42, [1, 3])
9       list3 = createnozzlelistsp(42, [1, 2, 3])
10      m = len(list1)
11      prefix = b'\x1b' + str_hex('i')  # ESC i
12      c = b'\x01'  # COMPRESSED
13      b = b'\x02'
14      n = 1
15      nL = dec_hex(n % 256)
16      nH = dec_hex(n / 256)
17      mL = dec_hex(m % 256)
18      mH = dec_hex(m / 256)
19
20      image = ESC_dollar(hor, x) + ESC_i_nrs(list1, r, size) + \
21              ESC_dollar(hor, x + dx) + ESC_i_nrs(list2, magenta,size) + \
22              ESC_dollar(hor,x + 2 * dx) + ESC_i_nrs(list3, black2, size)
23
24      # suffix1 = b'\x0d' #b'\x0d\x0c'
25      total = image
26
27      return total
```

Figure A.5: Example script for printing a letter P, constructed out of 3 vertical lines, consisting out of 10 drops in total.

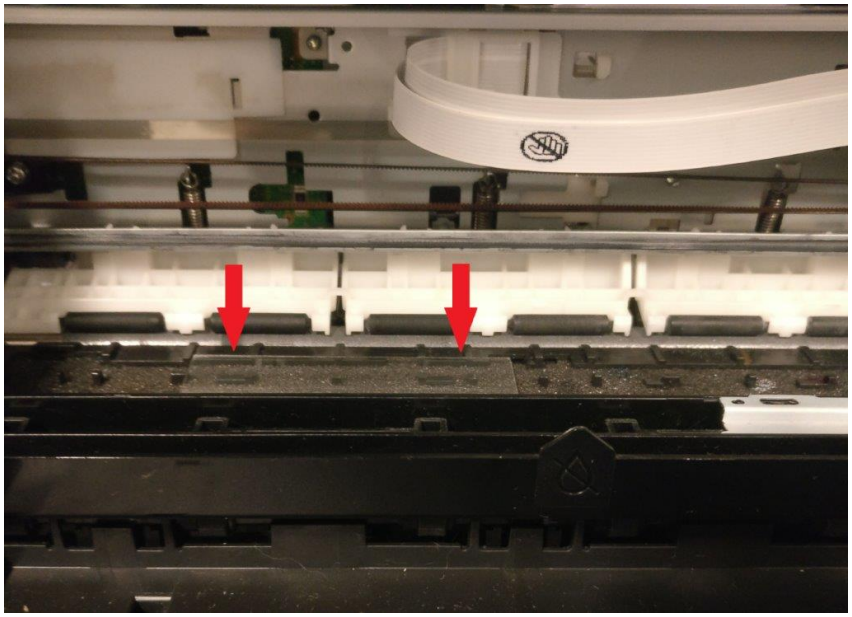

Figure A.6: Epson printer with indication of glasslide location.

and place the right side of the bottom back, this is required for the paper not to get stuck during printing. Fill the gap on the left side till the right print height. Even though printing on a solid substrate, the printer has a internal paper feed sensor which needs to be tricked. By cutting A4 in $\frac{1}{3}$ strips in the lengthwise direction. These strips can then be place on the right side of the printer. During the printing process the printer will feed a paper sheet through, satisfying the paper sensor condition, in a region not interesting for the actual print process. After printing the printhead will move to a resting position on the right side of the printer. **Be aware** the printhead will still move after a few minutes and will hit you trying to take out the sample. Only once it is fully inside the housing of the printer after a purging line, the printhead is at rest!

B | Cleaning the Epson printhead

This appendix will describe different cleaning techniques for the Epson printhead, which will have to be frequently performed to be able to have all 254 nozzle unclogged.

Software purging

The fastest way to unclog the nozzle is by running a nozzle cleaning cycle, which becomes available after installing the Epson firmware. This will take several minutes and its effectiveness depends on the ink present in the cartridge.

Flushing with a pippette

One of the best ways to get a good print results is to flush the nozzles with the print ink using a 5.8mm plastic pipette. Move the printhead out of its storing position. Place a piece of Tork paper onto the bottom of the printer and move the printhead over it. Take the ink cartridge you want to print with out of the printer and flush the print nozzle shown in Figure B.1a with the ink, until you see wetting of the paper underneath. Perform a test print, a vertical print line with all nozzles activated is the fastest method.

Taking the printhead out

If none of the other options work, the best way to clean the printhead is to take the printhead out of the printer. Use the following youtube movie to see how [https://www.youtube.com/watch?v=Xb7Bc1jGIrA Once the printhead is out. Place it in a glass dish and clean the top side shown in Figure B.1a thoroughly with DI water and Isopropyl . Once the outside is clean we can now clean the nozzle itself. Flush a glass dish with DI water to hopefully remove most of the dust particles and fill it with a thin layer of cleanroom Isopropyl. Place the printhead, with nozzle plate down in the liquid. Using a syringe with black tubing as shown in the Figure B.1b suck the liquid from the glass dish through the nozzles until only clean liquid comes out. The printhead should now be fully cleaned. Install the printhead back into the printer and purge the printhead with the inkjet ink by creating a word document solely in the color of the ink to print with.

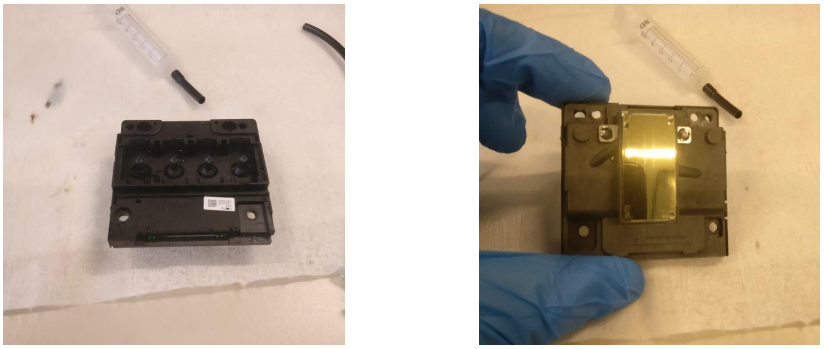

(a) **(b)**

Figure B.1: Printhead of the Epson XP-235 showing in (a) the topside fully cleaned and (b) the nozzle plate

C | Step by step guide: Printing with the PIXDRO LP-50

Ink preparation
The printing of the Inkjet printing starts with the inkjet ink preparation. DI water and the NanoAmando 'mother solution' can be measured and dispensed in the right am mount using the auto pipettes. However due to the viscosity of glycerol, the auto pipette does not work well and it is difficult accurately dispense the liquid. Therefore a plastic manual pipette and a glass graduated cylinders are used. Fill the graduated cylinder with the right volume of glycerol and mix DI water and glycerol in a glass beaker under high ultrasonication, manually mixing with a swirling motion speeds up the mixing process. Under ultrasonication, slowly add the mother solution to the water glycerol mixture until the solution has an uniform brownish color. Start by breaking of the lips as shown in Figure C.1b, this will allow to later refill the ink cartridge if needed. It helps to place the cartridge upside down in a old tape spool as shown in Figure C.1a. Get a syringe and fill it with the ink. Apply a syringe particle filter with poresize of .45 μm and a needle and slowly fill the cartridge. If you fill it to fast, air will be trapped inside and the cartridge will overflow. Once the cartridge is full place it on top of a 302 clean room paper inside the degasser and apply vacuum for 5 min. Click the printhead on the ink cartridge and place it in the printer.

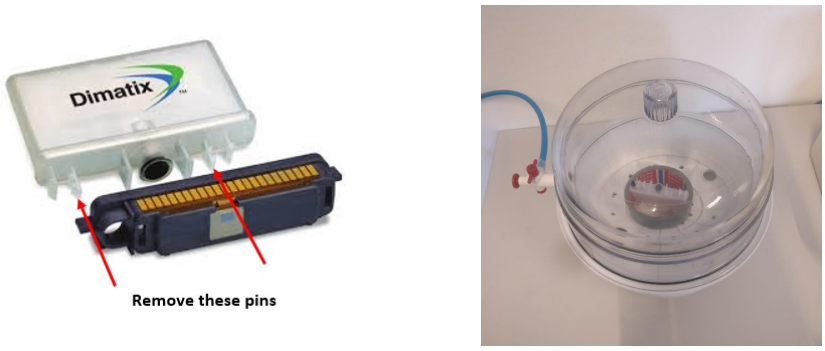

(a) **(b)**

Figure C.1: A The DMC-11610 cartridge and the pins to remove to be able to refill **b** Degassing of the ink after filling

PIXDRO HMI
After switching on the printer, start the PIXDRO software Human Machine Interface (HMI).In the HMI go to the controls window Figure C.2, and thick all check boxes marked in the figure. The printhead is set to 29°C, increasing the printhead temperature improves the jetting stability. Internal heating from the printer itself and external heating due to the sun is limited this way. The printhead will now light up. Click initialize on the right side of the window for an auto calibration of the printer axes.

After the initialization. From the control window, select the maintenance tab and check the purging pressure. Depending on the viscosity of the ink and the cartridge used (1 or 10pl) this value should be changed. For the water:glycerol diamond ink 200mbar is the default value, for silver ink change it to 50 or 100mbar. Switch to the dropview window Figure C.3 and purge the printhead 2 times. Clean the printhead and purge two more times and clean again. Move the printhead to the nozzles by clicking "go to nozzle" when selecting start head all nozles selected in "Dropview activated nozzles" will start jetting. By going to the wave tab, the waveform now needs to be tuned, untill stable drop formation of the right size and with a speed of around 6m/s is achieved. The 3 main parameters to start out with are in order of importance, Time low, Fire ramp and Voltage high. The other parameters are best tuned by varying the value with ±.5 and observing the change. Once the wave form is properly tuned, in the "Dropview activated nozzle" select one of the better nozzles and active only this nozzle. The waveform behaves differently when only a single nozzle is activated. Once the

Figure C.2: Controls window of the PIXDRO HMI

waveform is properly tuned, we'll have to test how it prints. **stop the head**, before moving to the next step. A common mistake is moving the printhead while still jetting. Deposition droplets all over the printer.

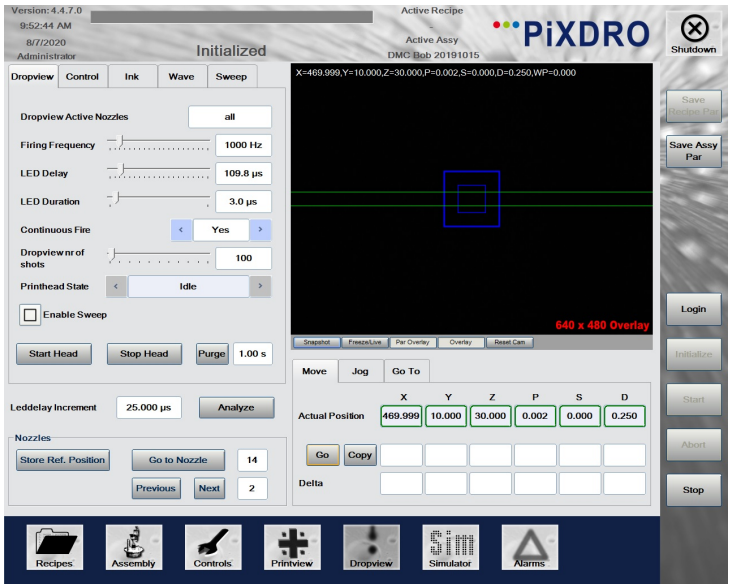

Figure C.3: Dropview window of the PIXDRO HMI

Assembly and Recipe settings

Change to the assembly tab, select DMC and change the settings or create a new assembly under your own name. In the assembly settings the printhead is selected and in the printhead setting Figure C.4, you can select which nozzle to use for printing. Now go to the Recipe settings and create a new recipe. In the setting of the recipe you can locate the image file to print. At the bottom of this setting window are some important parameters, such as scaling and the DPI. By switching Bitmap scale to yes, with the settings below the dimension of the print pattern can be changed. In Figure C.5 and object of 2 by 1mm will be printed.This dimension is based on the total image including any white boundaries around the object. It is therefor recommended to crop up to the boundaries of your image. The DPI determines in the drop separation and/or drop overlap during printing. To first check the print quality of the selected nozzle. Print at a DPI value low enough so the droplets don't overlap, this will also allow to measure the diameter of the individual drops, which is use full in calculation the right dpi required for drop overlap.

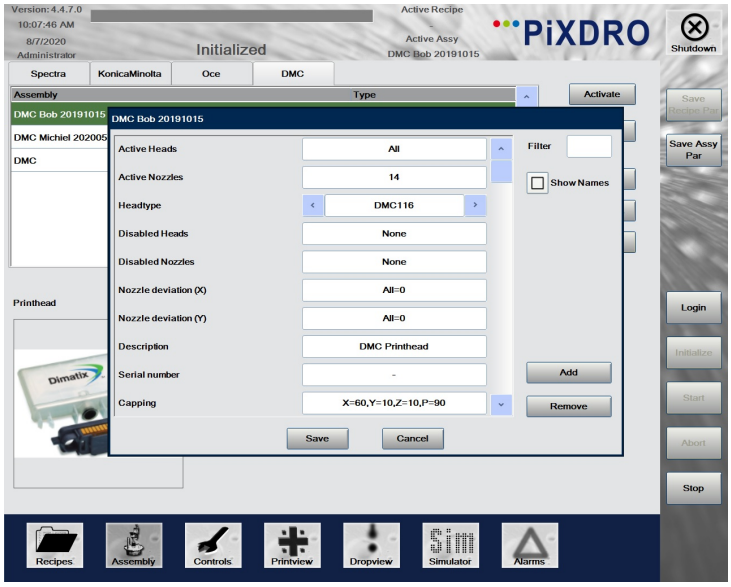

Figure C.4: Assembly setting window of the PIXDRO HMI

Print alignment

It is **important** that before this step you check the substrate height settings. Is this setting is to low for the substrate you're printing with the printhead will collide with the substrate. The printbed consist of small holes for the application of vacuum which helps with the stability of the print lines. Using a laminating sheet the samples can be placed on remaining open holes Figure C.6. Now switch on the vacuum, make sure all holes are covered, as open holes can result in a vacuum drop and an error during printing. The circular hole has been cut to be able to print on 2inch wafers. Using the printview window, the samples should be around the position defined in "alligned start position", by clicking 'Go To', the printhead camera will move to the alligned start position. To help locate your sample, the camera has a red light to indicate where it is viewing. Using the jog command locate the south west corner of the printer, by clicking the jog value with either right and left, the jog increment is decreased or increased respectively. Press teach to define the starting position of the print. There is a slight offset between the set starting position and the actual print position, therefor, recommended is to stay at least .5mm from the edge. Now move to the dropview position, start the print head, and from here select to start the print. Printing from the dropview position will make sure the print nozzles have not dried, resulting in bad quality prints. Once the print is done the printhead will move to the service position. You can inspect the sample by moving back to the print allign position of take the sample out for further processing. While leaving the printer unattended move the printhead to the dropview position and start the printhead with a jetting frequentie of 1Hz, continuous jetting prevents drying of the printhead. When done printing, remove all power form the printhead, using the control tab, shutdown the printer and take out the printhead. Leaving the printhead in the printer will turned off will cause leakage of the ink. The printheads are best stored in ziplock bags covered in a 402 cleanroom cloth and depending on the ink, for example in case of the silver Metalon® JS-B25P, slightly wetting this cloth with IPA, again to prevent clogging of the nozzles while stored. The Metalon® JS-B25P should also be stored in the fridge when not in use.

Drying

After printing with the diamond ink, to evaporate the glycerol before diamond growth a drying step is required. This is done putting the sample on a microscopic glass slide and placing it on a hot plate. The hot plate is then slowly increased with steps of $50°C$ until a temperature of $200°C$ is reached, leave it for 5 more minutes. All the liquid should now have been evaporated. Take the glass slide off by using metal tweezers and let it cool for a couple minutes. The samples is now ready for the diamond growth process.

Figure C.5: Recipe setting window of the PIXDRO HMI

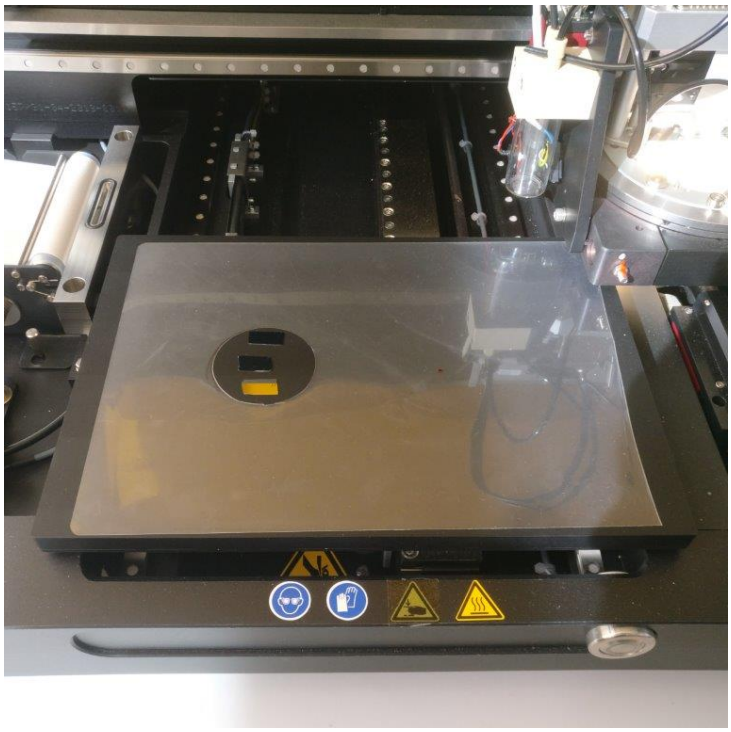

Figure C.6: Printbed with the laminate sheet on the PIXDRO printer

D DMC waveforms for different inks

This chapter shows the waveform settings for different cartridges with the different inks. These waveform settings can act as a baseline for tuning. Note that the 1 pl cardridges have a lower supply voltage.

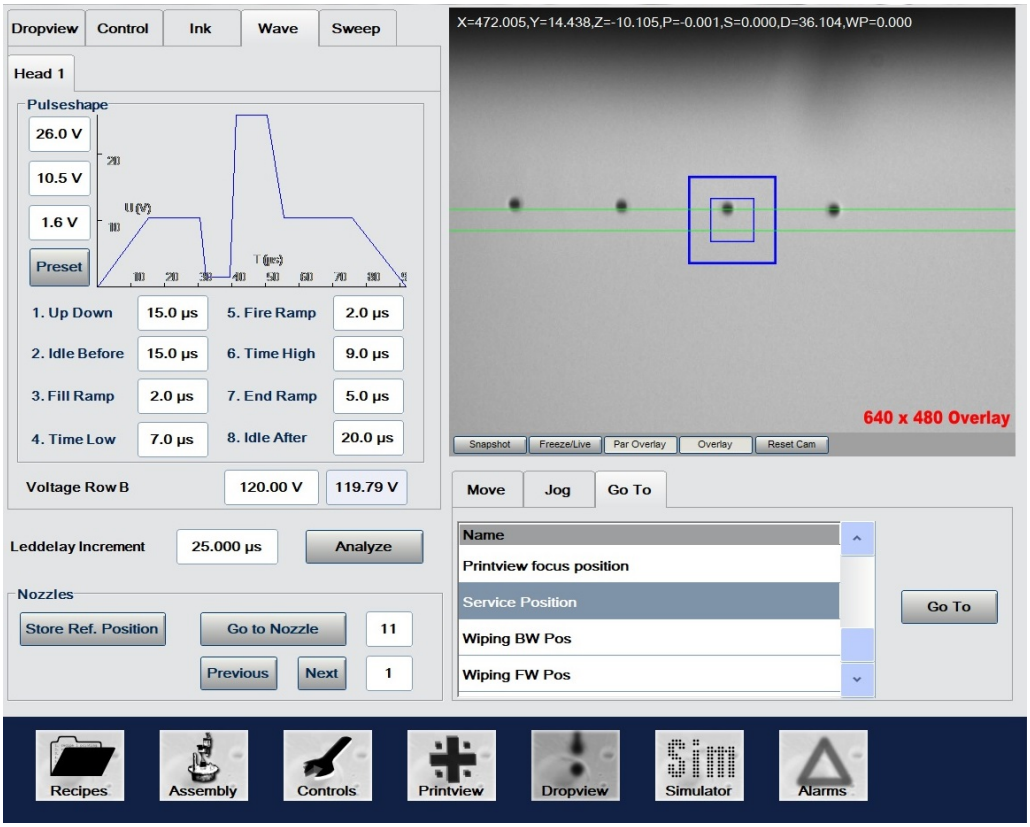

Figure D.1: Waveform settings for 10 pL printhead with metalon silver ink

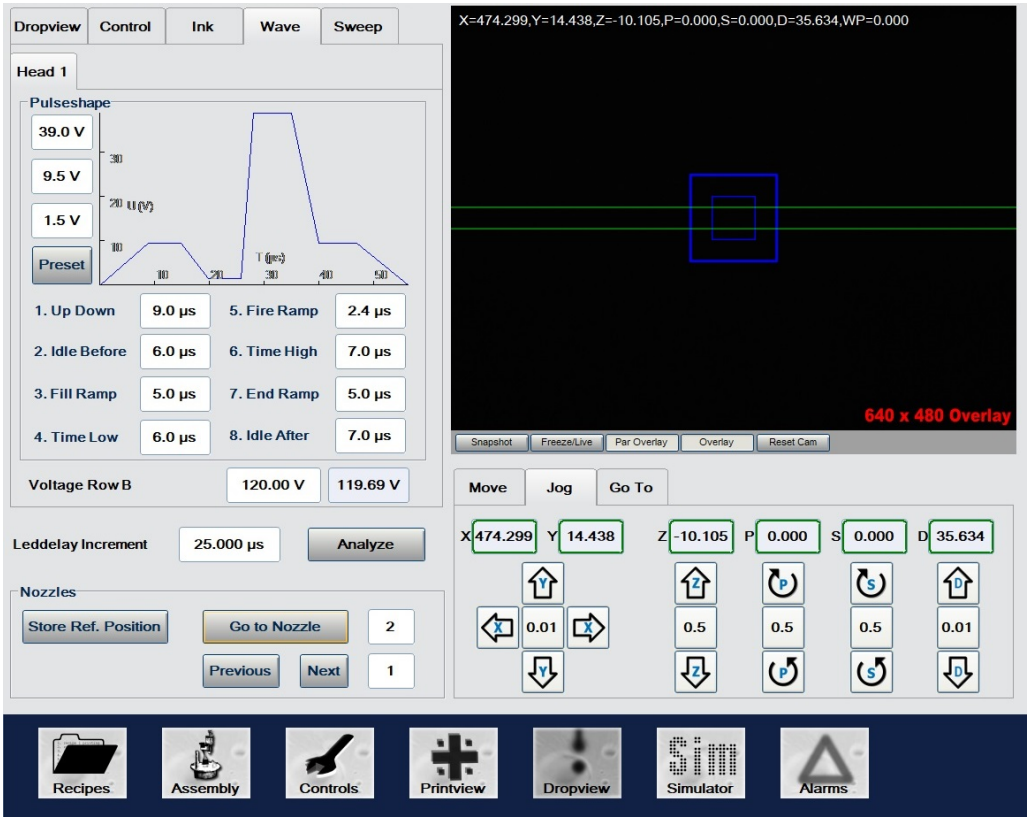

Figure D.2: Waveform settings for 10 pL printhead with water:glycerol 50:50 vol.%

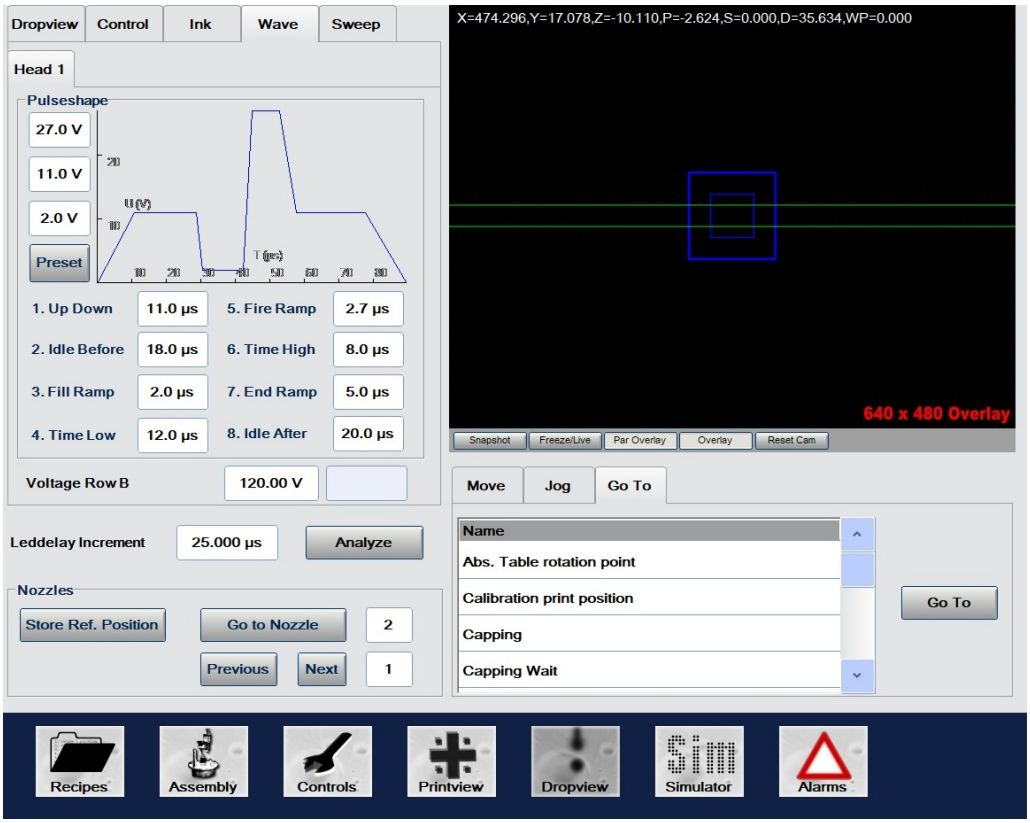

Figure D.3: Waveform settings for 1 pL printhead with water:glycerol 50:50 vol.%

E Electrochemical data

In this appendix, the graphs associated to the electrochemical analysis using the DropSens electrode are shown. Cyclic voltammogram of RuHex is shown in Figure E.1a and Figure E.1b the linear regression, whereas the CV of Ferrocyanide is presented in Figure E.1c and linear regression in Figure E.1d. The data is IR corrected for a value determined using frequency response analyzer (FRA) of 560Ω and 588Ω for RuHex and Ferrocyanide respectively.

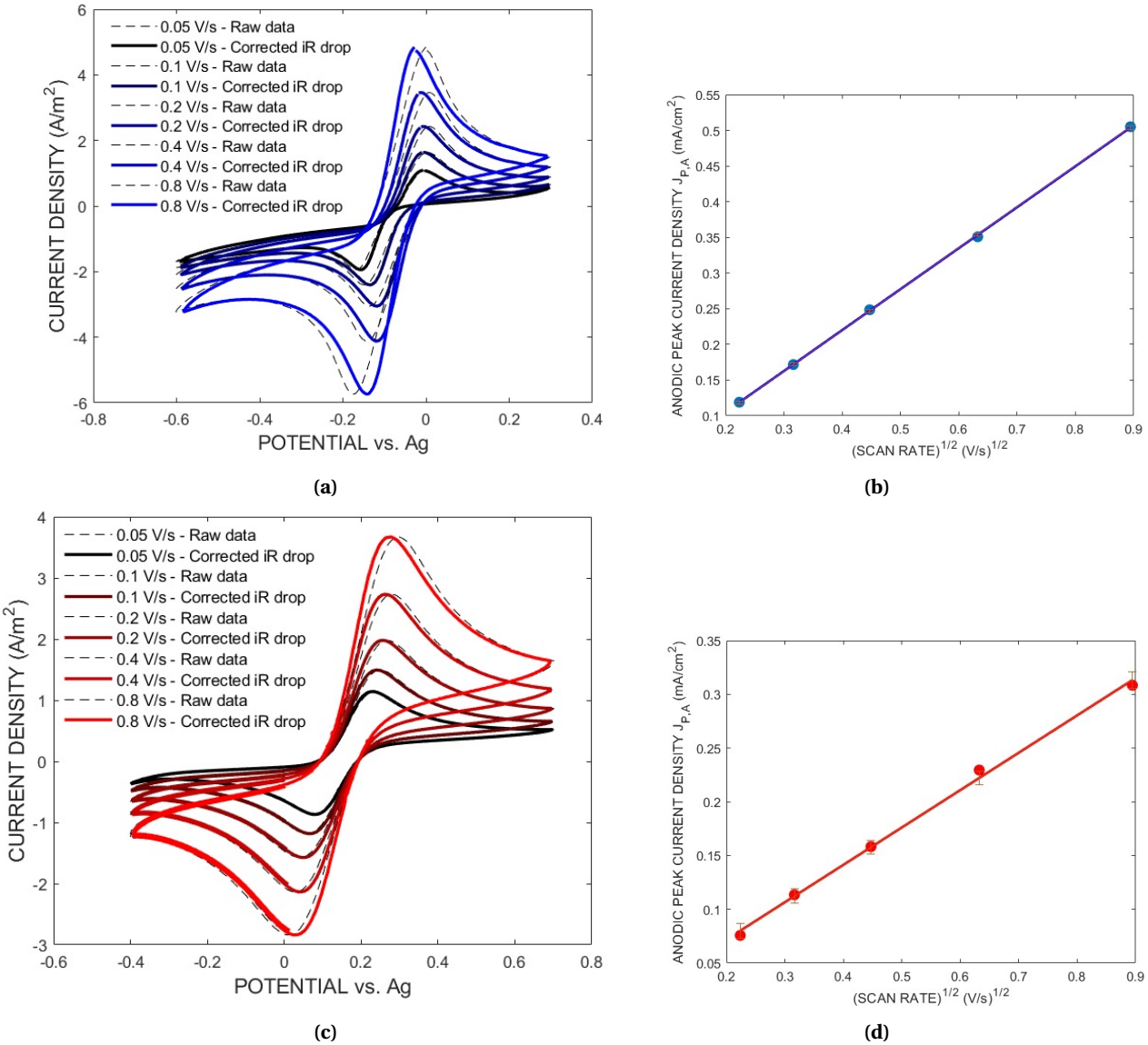

(a) **(b)**

(c) **(d)**

Figure E.1: **(a)** Cyclic voltammogram and **(b)** linear regression for 1 mM $Ru(NH_3)_6^{3+/2+}$ in a solution of 0.1M KCl and **(c)** CV of and **(d)** linear regression for $Fe(CN)_6^{3-/4-}$ in a solution of 0.1M KCl

F | SEM images

This appendix illustrates a selection of SEM images of different electrode geometries. The high contrast helps to detect any defects in the thin film layer.

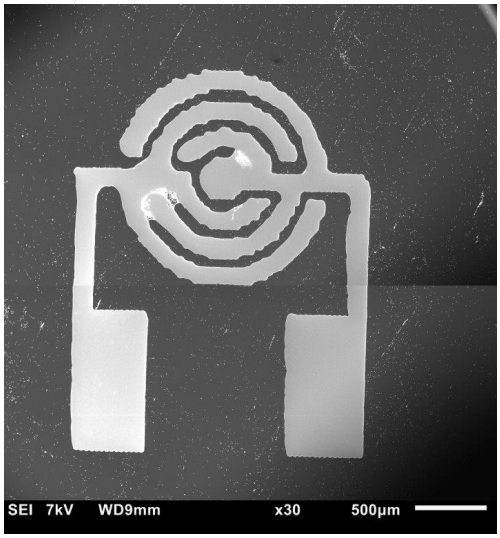

(a)

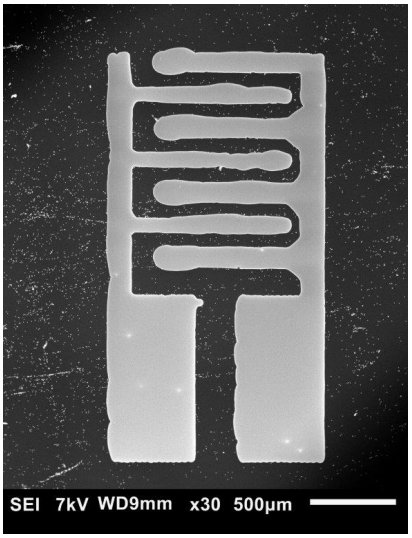

(b)

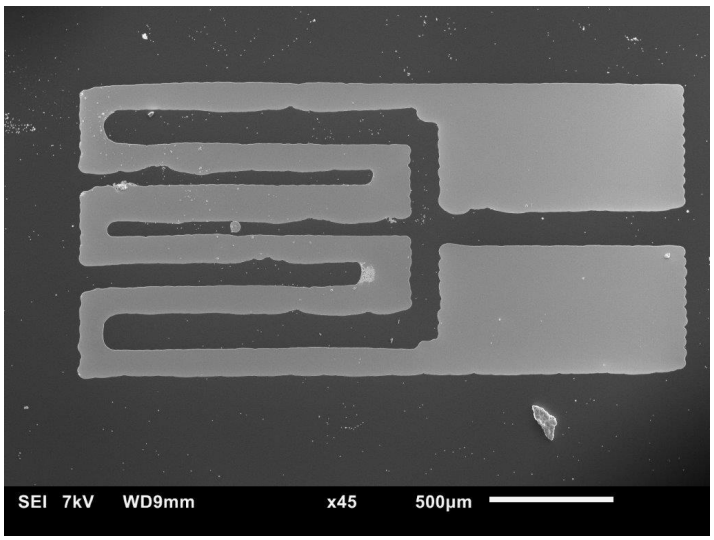

(c)

Figure F.1: SEM images of thin film diamond geometries with in **(a)** a circular electrode, **(b)** an interdigitated electrode and **(c)** a 2D heater.

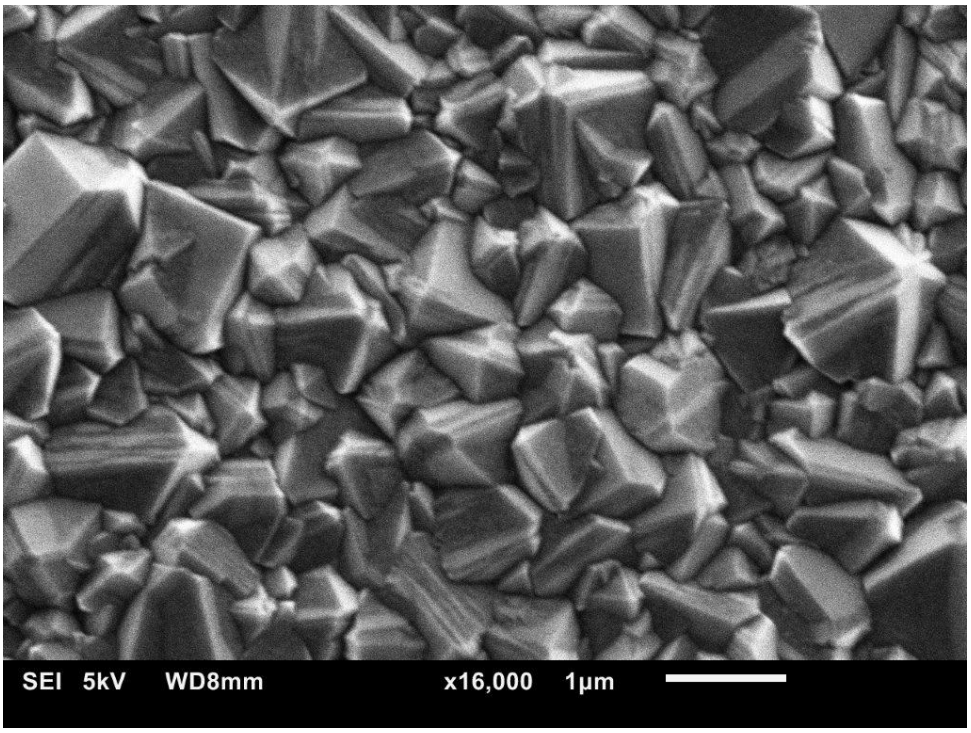

Figure F.2: SEM image depicting the diamond surface morphology of a thin-film approximately 1 μm thick, grown after seeding the surface using inkjet printing.

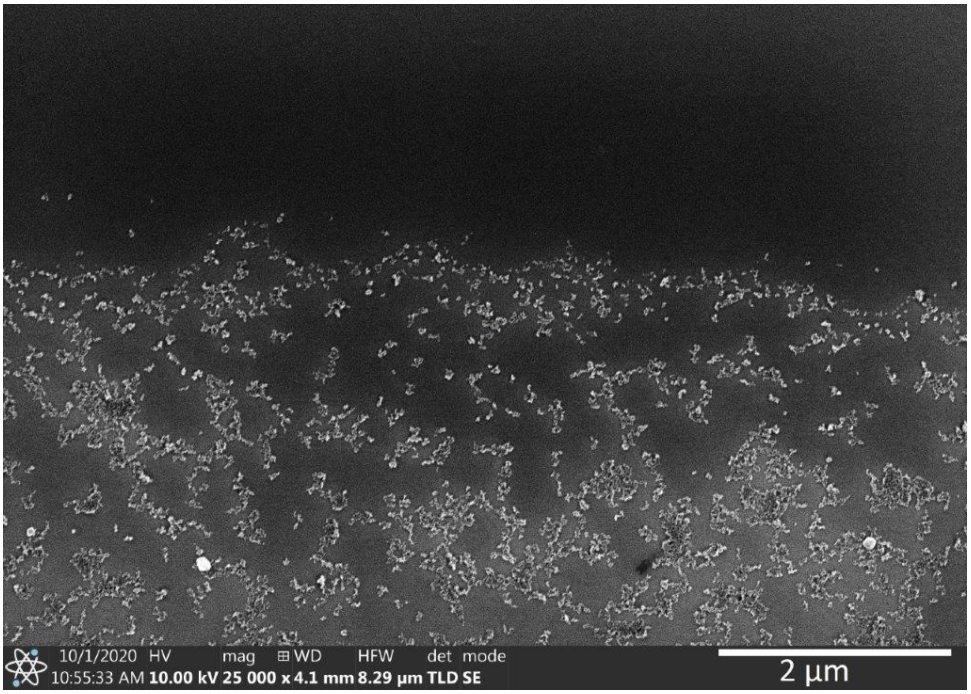

Figure F.3: High Resolution SEM image of the particle distribution after printing with 0.4% (wt/vol) diamond NPs at 850DPI on an air exposed silicon substrate, on the top side the boundary of the droplet, showing a gradient with a larger concentration of particles towards the center of the droplet.

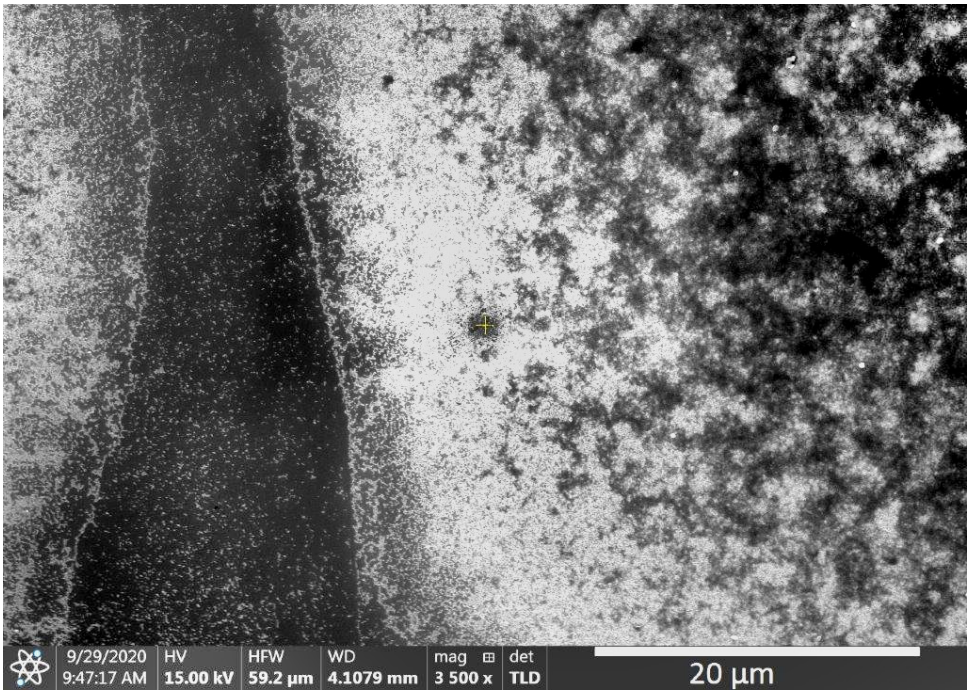

Figure F.4: High Resolution SEM image of the particle distribution of a print with 0.4% (wt/vol) diamond NPs at 850DPI on pristine silicon. Showing the seeding on the droplet pattern and inbetween.

G White-light interferometry images

The following images are white-light interferometry images taken on samples printed on pristine silicon at 1000DPI.

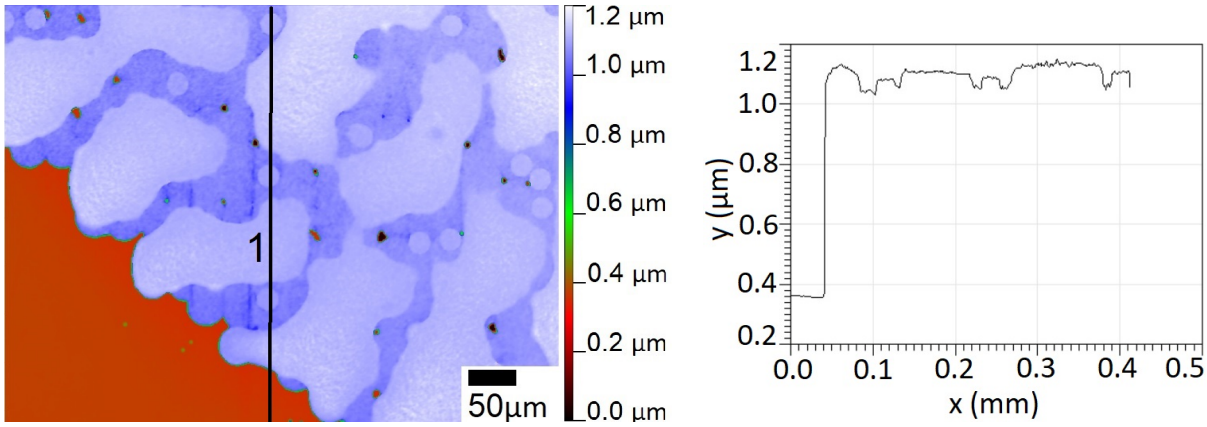

(a) **(b)**

Figure G.1: White-light interferometry images with in **(a)** 2d section view of part of an diamond electrode pattern printed at 1000DPI after CVD growth for 45mins. Line (1) marks region for the section view shown in **(b)** showing total diamond thin-film thickness of 0.8 μm and approximately 100 nm local height difference due to the inkjet seeding process.

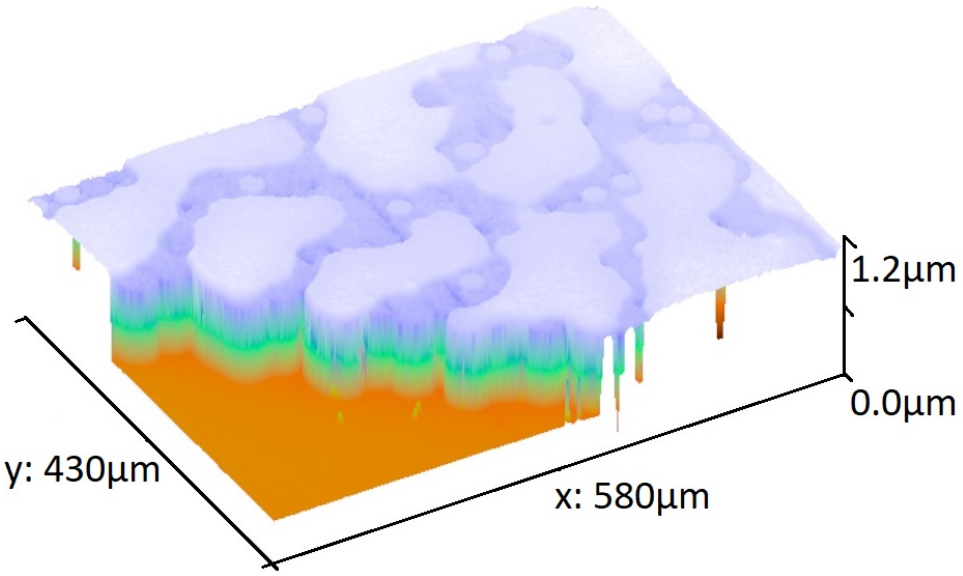

Figure G.2: 3d view of while-light interferometry data of the section shown in fig. G.1.

H Additional images

The following images are a collection of optical images, print patterns using various techniques, diamond patterns, printer components and a cross-section view of the DropSens electrode

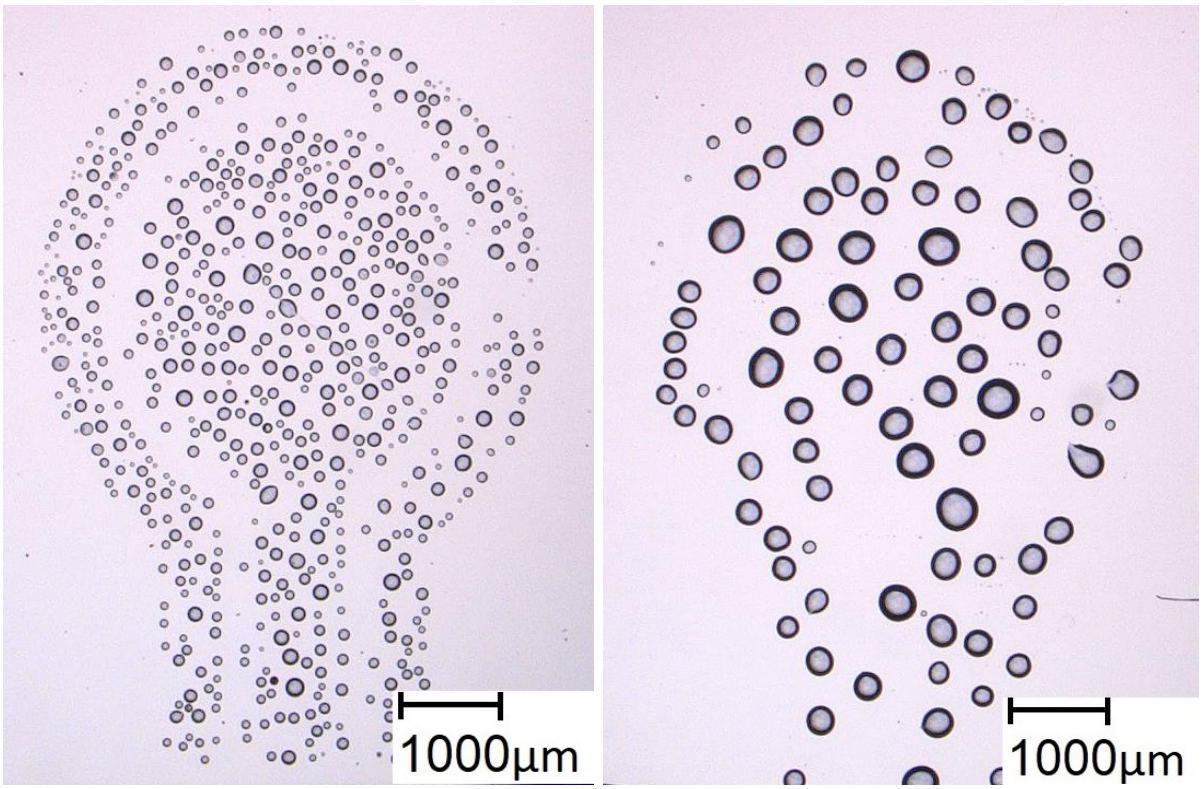

(a) **(b)**

Figure H.1: **(a)** Printing with Tri(Ethylene glycol) Monoethylether on pristine silicon and **(b)** on the substrate after oxygen plasma treatment.

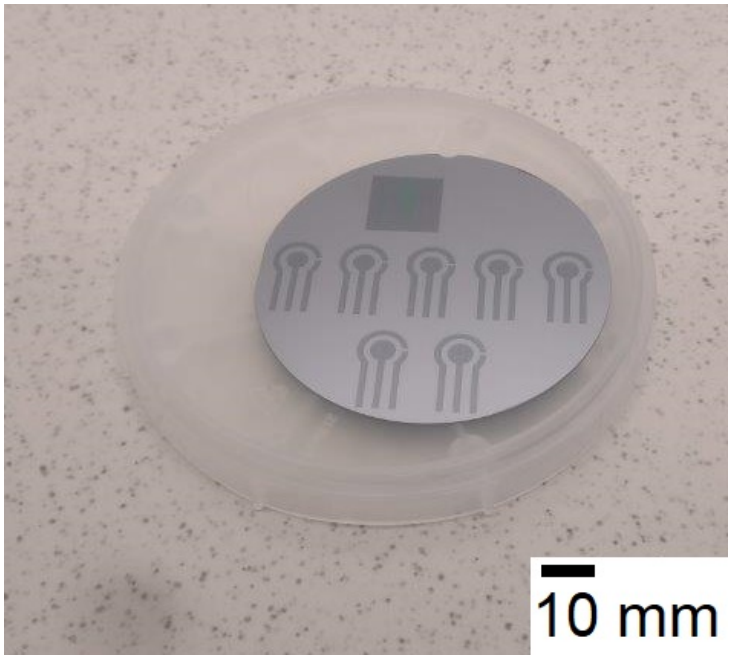

Figure H.2: Wafer perpared for BDD growth, with inkjet printed patterns using the air-exposed method.

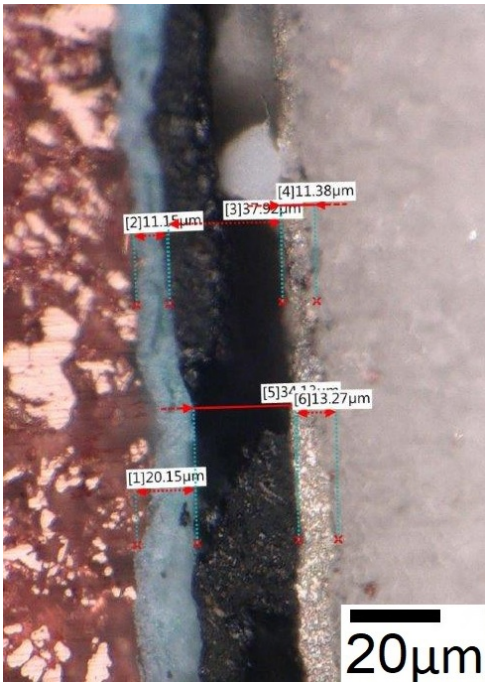

Figure H.3: Optical image of the cross-section of the DropSens electrode, showing the approximate thickness of the different layers in micrometers, from left to right; the conductive polymer required for the polishing step, the dielectric layer in blue, carbon, silver and the alumina substrate.

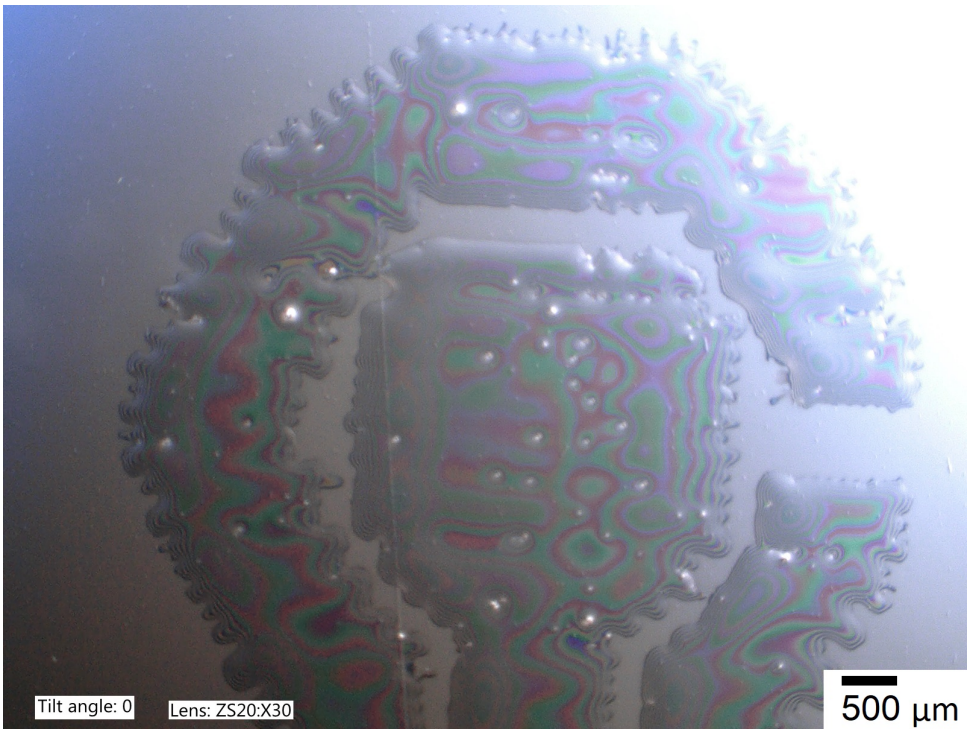

Figure H.4: Epson printed pattern after oxygen plasma treatment and 3 print passes.

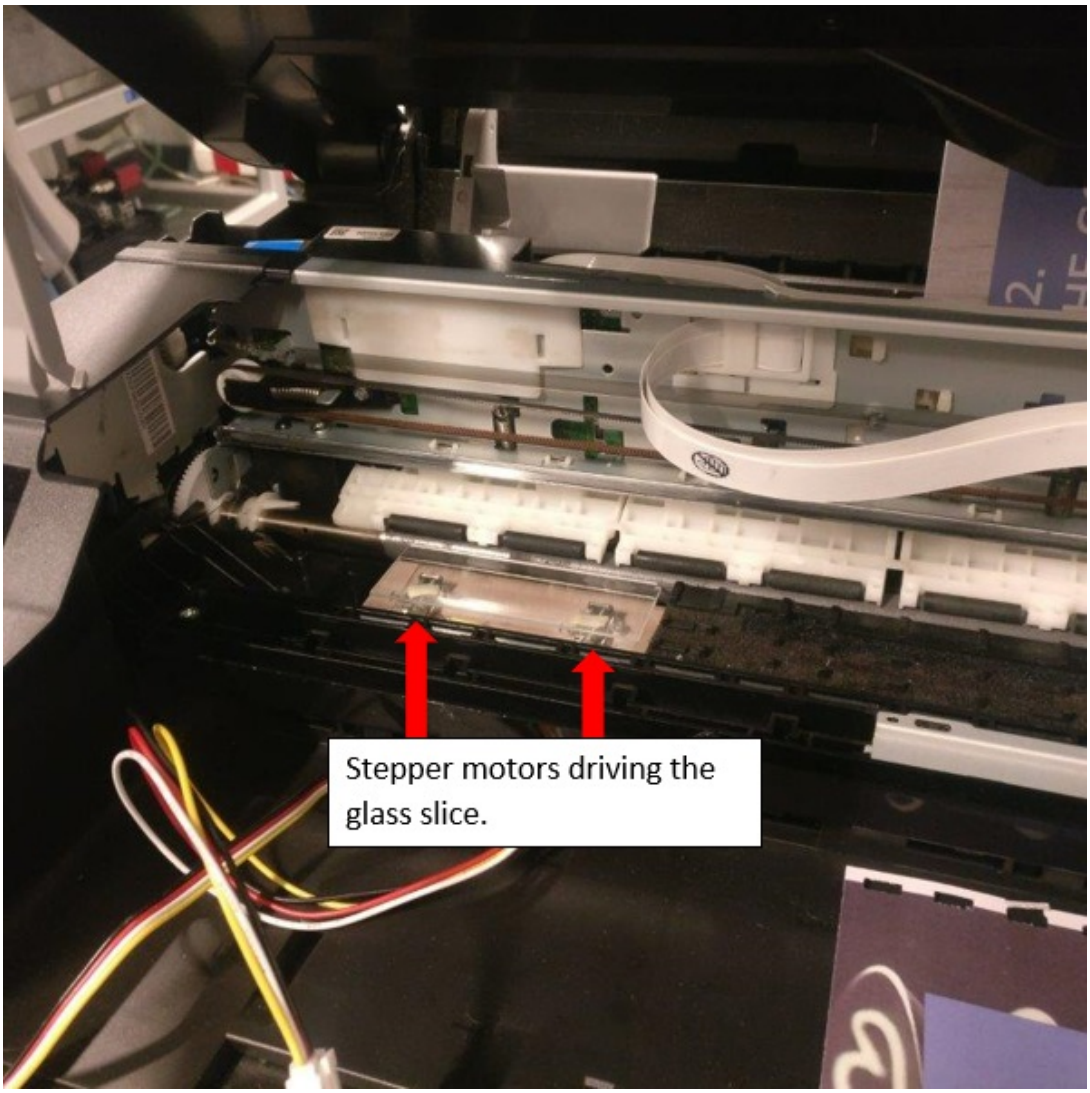

Figure H.5: The motion stage, controlled by two linear stepper motors inside the bottom of the Epson XP-235

I Print designs

The following appendix shows the technical draws used as print design for the conventional chip electrode design, a design for the 2d heater, the interdigitated electrode and the circular electrode.

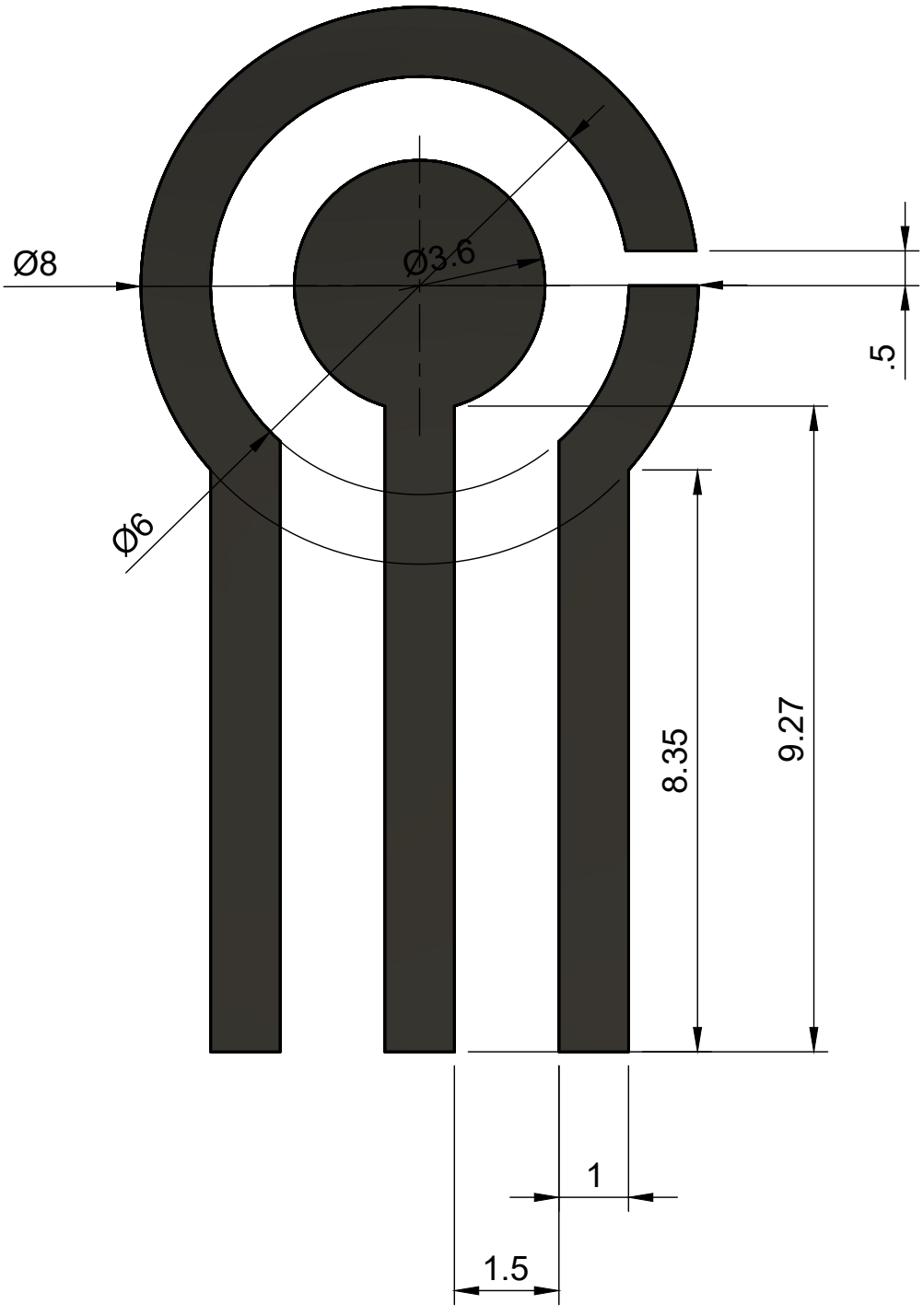

Dept.	Technical reference	Created by Bob Brocken 15-06-2020	Approved by
		Document type	Document status
		Title Resistivity test 3.6mm Scale 10:1	DWG No.
			Rev. / Date of issue / Sheet 1/1

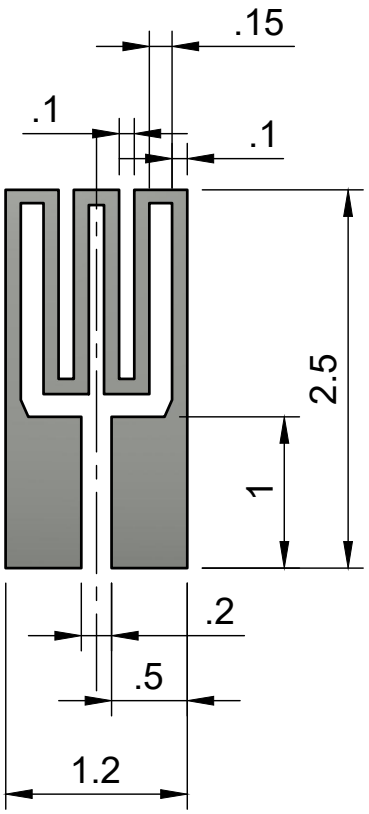

Dept.	Technical reference	Created by	Approved by
PME		Bob Brocken 13-7-2020	
		Document type	Document status
		Title Heater Scale 20:1	DWG No.
			Rev. / Date of issue / Sheet: 1/1

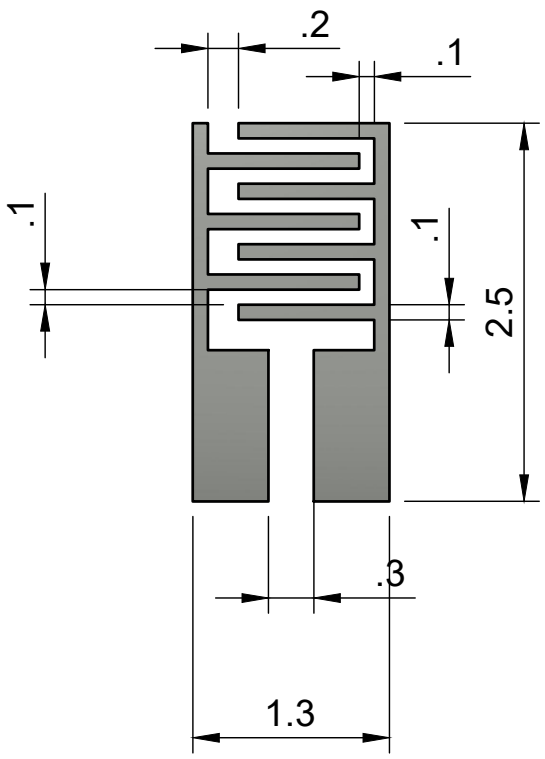

Dept.	Technical reference	Created by	Approved by
PME		Bob Brocken 13-7-2020	
		Document type	Document status
		Title: interdigitated electrode sensor	DWG No.
		Scale 20:1	Rev. / Date of issue / Sheet: 1/1

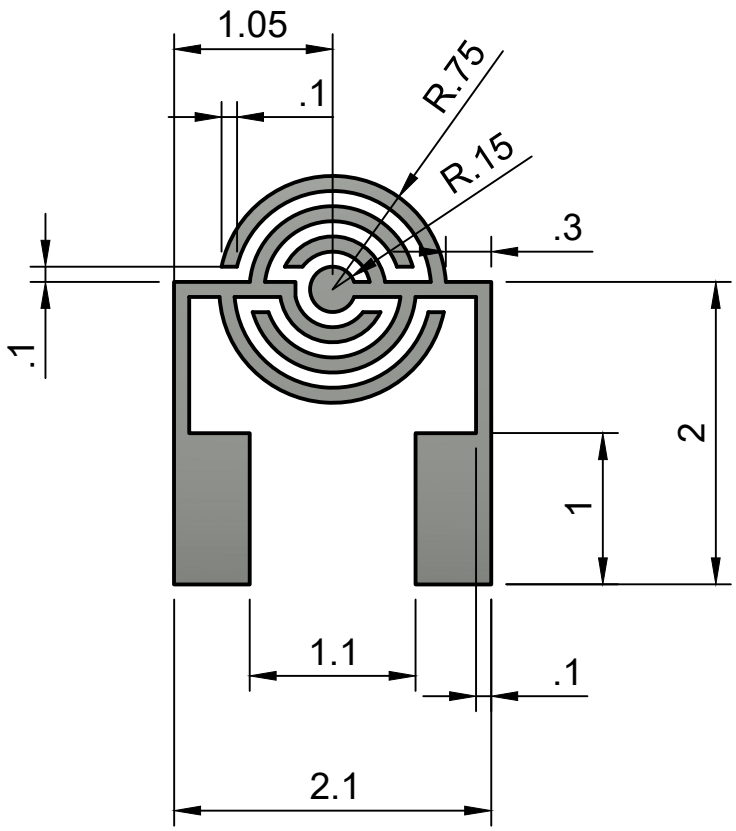

Dept.	Technical reference	Created by	Approved by
PME		Bob Brocken 13/07/2020	
		Document type	Document status
		Title Spiral Scale 20:1	DWG No.
			Rev. / Date of issue / Sheet: 1/1

J DLS results

The following pages show the results of the dynamic dight scattering experiment, showing first the test performed on a small volume of (1:1 water:glycerol) 0.4 %(wt/vol), secondly the NanoAmando aqueous colloid solution and finally pure DI water.

Size Distribution Report by Intensity

v2.2

Sample Details

Sample Name: nanoparticles-13-2 3

SOP Name: diamond_nanoparticles.sop

General Notes:

File Name:	Example Results.dts	**Dispersant Name:**	Water
Record Number:	111	**Dispersant RI:**	1,330
Material RI:	2,42	**Viscosity (cP):**	0,8872
Material Absorbtion:	0,000	**Measurement Date and Time:**	maandag 6 juli 2020 15:35:...

System

Temperature (°C):	24,9	**Duration Used (s):**	60
Count Rate (kcps):	348,5	**Measurement Position (mm):**	3,00
Cell Description:	Disposable low volume cuv...	**Attenuator:**	6

Results

			Size (d.nm...	% Intensity:	St Dev (d.n...
Z-Average (d.nm):	85,22	**Peak 1:**	109,6	100,0	58,05
PdI:	0,230	**Peak 2:**	0,000	0,0	0,000
Intercept:	0,926	**Peak 3:**	0,000	0,0	0,000

Result quality Good

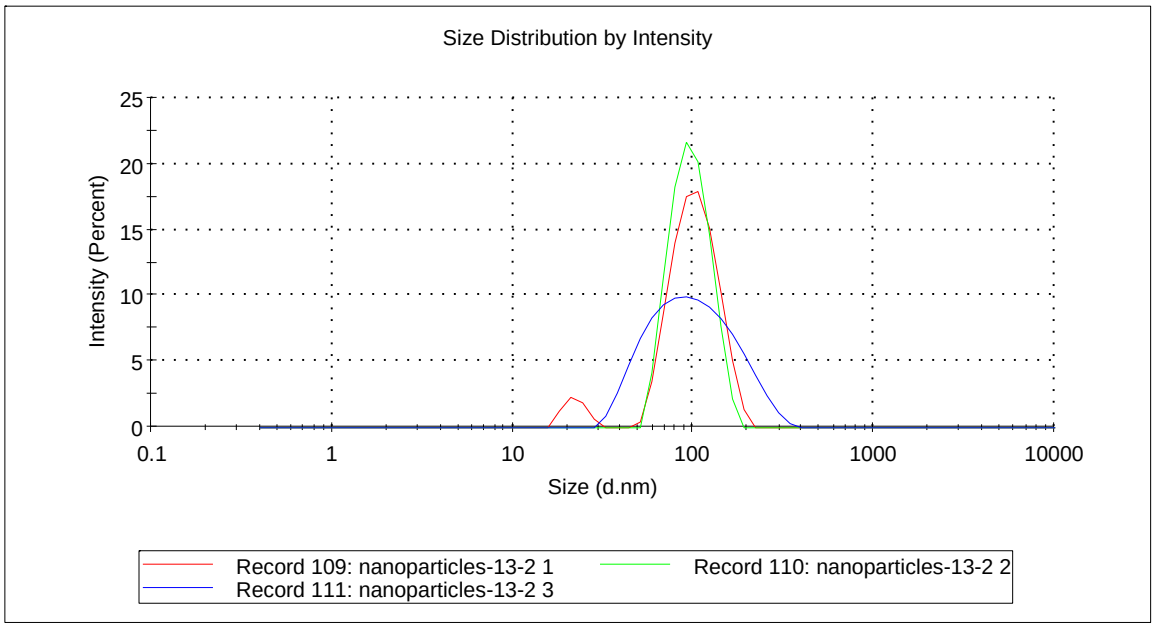

Size Distribution Report by Intensity

v2.2

Sample Details

Sample Name: nanoparticles-stock-solution 3

SOP Name: diamond_nanoparticles.sop

General Notes:

File Name:	Example Results.dts	**Dispersant Name:**	Water
Record Number:	102	**Dispersant RI:**	1,330
Material RI:	2,42	**Viscosity (cP):**	0,8872
Material Absorbtion:	0,000	**Measurement Date and Time:**	maandag 6 juli 2020 14:56:...

System

Temperature (°C):	25,0	**Duration Used (s):**	60
Count Rate (kcps):	203,6	**Measurement Position (mm):**	3,00
Cell Description:	Disposable low volume cuv...	**Attenuator:**	6

Results

			Size (d.nm...	% Intensity:	St Dev (d.n...
Z-Average (d.nm):	72,99	**Peak 1:**	119,0	89,7	34,58
PdI:	0,509	**Peak 2:**	16,40	10,3	3,826
Intercept:	0,946	**Peak 3:**	0,000	0,0	0,000

Result quality **Refer to quality report**

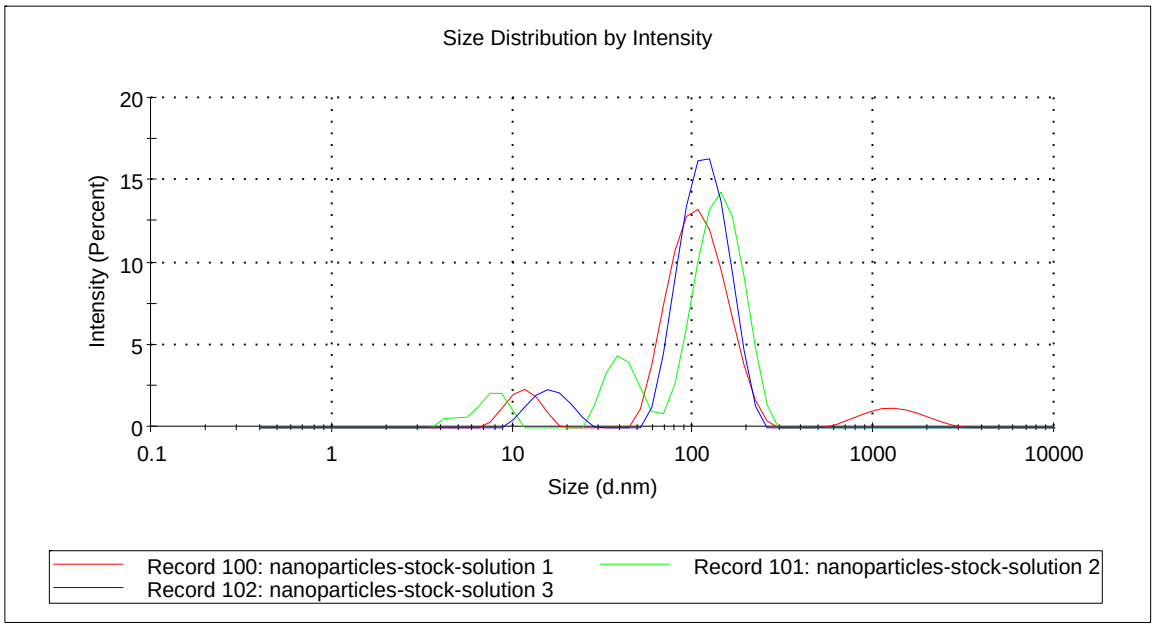

Size Distribution Report by Intensity

v2.2

Sample Details

Sample Name: water 3

SOP Name: diamond_nanoparticles.sop

General Notes:

File Name:	Example Results.dts	**Dispersant Name:**	Water
Record Number:	108	**Dispersant RI:**	1,330
Material RI:	2,42	**Viscosity (cP):**	0,8872
Material Absorbtion:	0,000	**Measurement Date and Time:**	maandag 6 juli 2020 15:21:...

System

Temperature (°C):	25,1	**Duration Used (s):**	80
Count Rate (kcps):	69,6	**Measurement Position (mm):**	3,00
Cell Description:	Disposable low volume cuv...	**Attenuator:**	11

Results

			Size (d.nm...	% Intensity:	St Dev (d.n...
Z-Average (d.nm):	2022	**Peak 1:**	239,4	100,0	17,31
PdI:	1,000	**Peak 2:**	0,000	0,0	0,000
Intercept:	0,235	**Peak 3:**	0,000	0,0	0,000

Result quality **Refer to quality report**